Gap Engineering and Simulation of Advanced Materials

A dissertation presented to

the faculty of

the College of Arts and Sciences of Ohio University

In partial fulfillment

of the requirements for the degree

Doctor of Philosophy

Kiran Prasai

December 2017

This dissertation titled

Gap Engineering and Simulation of Advanced Materials

by

KIRAN PRASAI

has been approved for

the Department of Physics and Astronomy

and the College of Arts and Sciences by

David A. Drabold

Distinguished Professor of Physics and Astronomy

Robert Frank

Dean, College of Arts and Sciences

Abstract

PRASAI, KIRAN, Ph.D., December 2017, Condensed Matter and Surface Science

Gap Engineering and Simulation of Advanced Materials (123 pp.)

Director of Dissertation: David A. Drabold

Generating computer models of materials that faithfully represent *all* of our current state of knowledge about those materials has remained an unsolved problem. In particular, models of amorphous solids following from a molecular dynamics (MD) simulation commonly show structural defects and related mid-gap electronic states that are not present in the real materials. In this dissertation, we present a novel way of using *a priori* knowledge of the electronic band gap of amorphous systems to guide MD simulations. This involves computing Hellmann-Feynman forces associated with certain electronic states and judiciously coupling them to the total force in MD simulations. We show that such a method can provide a means to purge structural defects. By producing a series of models of amorphous carbon with varying sp^2/sp^3 ratio, we'll show that this method offers useful new flexibility in modeling. And, we demonstrate, for the first time, how MD simulations can be biased to systematically model an insulator-metal transition in glassy systems. The nature of electron transport in $GeSe_3Ag$ glass is explored using advanced methods and important inferences are drawn about the role of Ag atoms in electronic conductivity. In particular, it is shown that a certain Se-Ag phase in this glass plays a dominant role in electron transport. We also investigate the response of *a*-$GeSe_3Ag$ to radiation damage using empirical interatomic interactions and show that the glass exhibits rapid recovery after a knock on event. Finally, we consider the the coupling between lattice vibrations and electronic states in disordered systems and show that disorder induced localization of states dictates the thermal modulation of electronic energy.

Matri Devir Shree Charane

Acknowledgments

I would like to express my deep gratitude to my advisor Prof. David Drabold for his continuous support, guidance and motivation throughout my PhD. His scientific insights and pedagogical excellence nurtured me throughout my PhD and brought me up as a young scientist. His teachings will be valuable resources for me throughout my life.

I am grateful to Prof. Gang Chan at Ohio University. Prof. Chen's insights from the experiments on glassy systems were always very valuable and immensely helpful. I am grateful to Prof. Parthapratim Biswas at the University of Southern Mississippi for his invaluable insights on modeling and simulations.

I am thankful to my senior group members Binay Prasai, Yuting Li and Mingliang Zhang for their advice. I have special thanks for my PhD colleagues Anup Pandey, Bishal Bhattarai, Dale Igram and Mayur Sundararajan for all the fond memories we share. I am grateful to Donald Roth and Edward Drabold for their assistance in setting up and managing computing resources.

I would like to extend my sincere gratitude to Ohio University and the department of Physics and Astronomy for providing me an opportunity to pursue doctoral degree. I am especially thankful to past graduate chair Prof. Daniel Phillips and current graduate chair Prof. Carl Brune for their support and guidance. I would like to thank all staffs in the department for their kindness, generosity and hard work. My sincere thanks to all the funding agencies, especially CMSS (for fellowship), NQPI (for travel supports), graduate college (for fellowship), and NSF (for grants DMR1507670 and DMR1506836).

I would like to express my gratitude to my parents, to my wife and my son, to my brother and his family, to my sister and her family and to the entire family of my wife. They have always been on my side whenever I needed them and I wouldn't have dared to pursue this project without knowing that I would have their support.

Finally, I would like to thank all my friends and relatives for their time and support.

Table of Contents

List of Tables

List of Figures

1 Introduction

1.1 Background

Amorphous materials and glasses are technologically important materials, and understanding their properties is an ongoing endeavor in condensed matter physics. Amorphous materials do not have long range order. This means that the structure of these materials cannot be expressed as a repetition of a finite sized building block analogous to the unit cells of crystalline materials. Crystalline materials are periodic, and experimental probes, like X-ray scattering experiments, point to a unique structural solution. The lack of such periodicity in amorphous systems renders the conventional tools of probing crystalline materials unusable and attracts a whole host of experimental as well as theoretical approaches that are able to deal with the statistical nature of the underlying system.

The structure of amorphous systems is far from random. These materials exhibit a strong local order, called the short range order (SRO) on the length-scale of up to about 5 Å. And, depending on material systems and method of preparation, there exists an intermediate range order (IRO) on the length scale of 5 to 20 Å [1]. The ordering can be better understood by reflecting on the process of preparation of amorphous solids by dynamical arrest where the smaller units forming the solids lose their dynamical degrees of freedom (get 'arrested') before they are able to 'click together' into a global network. Hence, the extent of order present in amorphous systems depends strongly on the details of their preparation. This is also manifested in energy landscape terms, where the crystal structure is represented as the global minimum in the landscape and the statistical nature of the amorphous configuration is the result of a multitude of thermally accessible local minima and the transition between those minima.

Emergent phenomena from such structure constitute an immensely interesting problem to a material scientist. On one hand, the structure is aesthetically beautiful: one where there is 'no dull repetition' (Erwin Schrödinger in "What is Life?", [2]) of a building block, but instead comes with a more subtle and elaborate pattern. The structure is dynamic and is constantly in transition among energy minima [3]. The disorder induces localization in the electron states and this gives rise to large thermal fluctuation of these states and a special electron-phonon coupling [4]. Localized states critically dictate the transport properties and various types metal-insulator transitions ensue [5]. That the disordered systems exhibit electronic band gap and display curious phenomena like Urbach tails have produced many theories in condensed matter physics [6, 7, 8].

On the other hand, modeling disorder and understanding its consequences is a daunting task. Experiments that probe the structure of amorphous materials usually capture the average distributions of atoms with respect to each other. It has been challenging to produce atomistic models of materials that match these average distributions and predict their properties correctly. A widely accepted theoretical model for certain amorphous materials is the *continuous random network* (CRN) by Zachariaisen [9]. In this model, all atoms are perfectly coordinated following Mott's '8-N rule' [10] but possess no long range order. In 1985, Wooten, Winer and Weaire [11] developed an algorithm based on Monte Carlo bond switching that was able to produce CRN for amorphous column IV materials. Later, the method was extended to binary glasses like SiO_2 [12]. This method is *ad hoc* in the sense that it assumes the complete *a priori* knowledge of bonding environment of all the atoms and is thus limited to few systems. Despite the limitation, WWW model of amorphous silicon is still considered the best model so far.

Molecular dynamics simulations are widely used to produce atomic models of liquids and amorphous materials [13]. Over the years, in parallel with the growth of

computational power, MD simulations have improved in accuracy and scope and can now describe complicated systems with impressive accuracy. In order to explore the stable low energy disordered minima, MD simulations mimic the experimental procedure of rapid quenching from liquid state. This consists of equilibrating the system at high enough temperature for long enough time so that the system "forgets" the initial configuration and then rapidly cooling the system and finally performing energy minimization to push the configuration to a local minima.

One major drawback of MD simulations aimed at generating models of amorphous materials is that they often end up producing models with too many defects, an unphysically wide distribution of bond lengths and bond angles, and consequently a strained network. Such structural defects may produce localized states in the band gap. This shortcoming of MD simulation arises mainly from two sources: i) inaccurate description of interactions within the system of electrons and ions ii) drastically short time scale of MD simulations compared to laboratory quench from the melt procedures which the MD simulations are designed to mimic.

The principal focus of this thesis is a newly developed method, called "Gap Sculpting", that attempts to address some of the shortcomings of MD simulation and allow the inclusion of *a priori* electronic information. At its core, the method proceeds by explicitly demanding that the final models of MD simulations have a realistic band gap, in addition to being at an energy minimum. This fits with the lore of "inverting experimental data" in the sense that *a priori* knowledge of band gap is used to guide the simulation towards the correct band gap. It is possible do so because of the multitude of energy minima available for amorphous systems and the process can be understood as exploring the energy minima with preferred band gap. This is the first demonstration of direct coupling of electronic structure information in MD. The method is developed in chapter 2. Through examples, it is shown that the new electronic constraints not only produce

realistic band gaps but also produce structures with fewer defects. It is a long-standing observation that localized states in the band gap are associated with defects in the network. There have been numerous works showing that better structures result in defect free band gap. This work is the first demonstration that the inverse is also true.

Once the method of guiding MD simulations to desired band gap is developed, it opens up a myriad of possibilities. We have exploited this to simulate a technologically important insulator-metal transition in silver doped amorphous chalcogenides. In this case, MD simulation is guided to produce a metal-like electronic structure. It is seen that the structures with metal like density of states match with the experimental observations of metallic state. The method is readily transferable to other systems and has potential to be the go-to method to explicitly simulate metal-insulator transition. This method is described chapter 3. This calculation emphasizes the utility of the method as a tool of materials engineering and design. The other focus of the thesis is understanding the structure of these silver doped chalcogenides and understand the atomistic mechanism of electronic conduction from the view point of use of these materials in memory devices.

1.2 Molecular Dynamics Simulations

Molecular dynamics or MD is a widely used method to study many particle systems. MD simulates the evolution of a system over a period of time by integrating equations of motion numerically [13]. In a collection of N classical particles, at positions R_i at time t and each with masses m_i the following equation of motion gives the evolution of system at time t+dt

$$m_i \frac{d^2 R_i(t)}{dt^2} = -\frac{\partial \Phi(R_1, R_2..., R_{3N})}{\partial R_i} \tag{1.1}$$

In MD simulation equation 1.1 is solved numerically over many time steps. Here, Φ represents total energy when the positions on ions are given by R_1, R_2.... R_{3N} and Φ is

calculated in different ways depending upon the nature of the interatomic interaction being considered. In this thesis, the following three types of interactions are used.

1.2.1 Empirical Potentials

Empirical potentials are widely used to model systems with thousands of atoms. These potentials are formulated by "guessing" a functional form to describe bonding and electrostatic interaction. Such a functional has free parameters which are then fitted in a way such that a chosen set of experimentally observed (or other) properties are reproduced. These potentials are computationally inexpensive so that large systems (from thousands to millions of atoms) can be simulated and evolution of the system for longer duration of time can be observed than is possible with more complex interactions. However, they suffer from transferability issues *i.e.* the energy functional may not capture the underlying physics when it is used to predict properties outside the domain of properties used to fit the parameters.

In this thesis, a classical potential formulated by Iyetomi *et.al.* [14] is used to model radiation damage in silver doped chalcogenide systems. Classical MD simulation code LAMMPS [15] is used to run the simulation.

1.2.2 Tight-Binding Method

Tight-binding is the simplest (and thus computationally inexpensive) method that explicitly involves an electronic structure calculation and is thus more predictive than empirical schemes. Here, electrons are treated as being tightly bound to the atoms and have limited overlap with rest of the electrons is the system. Then, if c_i denotes atomic orbitals (or the basis vectors), then the tight binding Hamiltonian is given by

$$H_{TB} = \sum_i V_i c_i^\dagger c_i - \sum_{i,j} (t_{ij} c_i^\dagger c_j + t_{ji} c_j^\dagger c_i) \tag{1.2}$$

where *t's* are the so called 'hopping' matrix elements and give the overlap between the atomic orbitals. The first term in Eq. 1.2 gives electron energy on isolated atoms and the second term gives correction in energy due to overlap. The total energy (ion + electron) governing the atomic motion is then given by the following relation [16]:

$$E_{tot} = \sum_i \frac{p_i^2}{2m_i} + \sum_n \langle \psi_n | H_{TB} | \psi_n \rangle + E_{rep} \tag{1.3}$$

where p_i is the momentum associated with i^{th} atom, m_i is the mass of the i_{th} atom, $|\psi_n>$ is the wave function of the state occupied by n^{th} electron and E_{rep} is a repulsive pair potential between the ions and also includes the correction to offset the errors due to other terms. For silicon [16] and carbon [17], as considered in this dissertation, minimal basis set comprises one s-orbital and three p-orbitals per atomic site. So the free parameters of the model are i) E_s and E_p: the on-site energies corresponding to the V_i in Eq. 1.2. ii) overlap amplitudes $t_{ss\sigma}$ $t_{sp\sigma}$ $t_{pp\sigma}$ $t_{pp\pi}$: corresponding to the t's in Eq. 1.2 iii) E_{rep}: the repulsion term corresponding to the one in Eq. 1.3 (in practice, it is there to offset everything else).

When the distances between the atoms is not fixed (as in the case of all amorphous materials), the parameters in ii) and iii) become distance dependent and hence need to be expressed in a functional form. In this dissertation, we follow the functional form prescribed by Goodwin, Skinner and Pettifor [18].

1.2.3 Density Functional Theory

The many body Schrodinger equation that involves full interaction between all the electrons and ions is an almost intractable problem [19]. Density functional theory (DFT) is an approximate but very successful solution to some aspects of this problem. After making the Born-Oppenheimer approximation (decoupling of ionic and electronic motion), the electron density ρ(r) is used to simplify the complicated many body equation into one-electron equations. This is possible due to a set of theorems by Kohn, Hohenberg

and Sham [20, 21] that electron density at ground state has one-to-one relation with the ground state energy. Kohn and Sham [21] postulated a form of Schrodinger equation that self-consistently (non-linearly) depends on electron density. These equations are called Kohn-Sham equations.

We employ the Vienna Ab-initio Simulation Package (VASP) [22, 23] to self-consistently solve Kohn-Sham equations. VASP uses plane waves as basis vectors, projector augmented wave (PAW) [24, 25] method for electron-ion interaction and local density approximation (LDA) [26] or generalized gradient approximation (GGA) [27] for exchange-correlation energy.

1.3 Chalcogenide Glasses

Glasses that contain one or more chalcogens (*i.e.* S, Se or Te) are called chalcogenide glasses [28]. Widely studied among these are the binary chalcogenide glasses Ge_tSe_{1-t} which are excellent glass formers for wide range of t [29]. In this dissertation, I will focus on a silver doped chalcogenide glass: $(GeSe_3)_{1-x}Ag_x$ where x denotes the Ag content. These materials can be prepared either by the melt-quench method or by photo-dissolution of Ag into the glassy host. This particular composition is a Se rich stoichiometry of a more broader class represented as $(Ge_ySe_{1-y})_{1-x}Ag_x$. The later class of glass shares many attributes used to characterize "network-former network modifier" class of glasses. In Se-rich limits, Ag is shown to act as network modifier and the glass is known to phase separate into Ag rich Ag_2Se phase and the remaining Ge-rich host network [30]. Ag atoms are known to be very mobile and this makes the whole glass structure very flexible and responsive to external perturbations. For example, these glasses have extremely interesting response to light [31, 32]. Among such interesting properties afforded by this glass is also the swift and dramatic change in electrical conductivity in response to small external bias. This property has been utilized to design memory elements out of these

materials, one where a thin film of this material is sandwiched between two electrodes and a small voltage is applied in between the electrodes. The bias voltage is seen to induce structural changes in the thin film and sharply change its conductivity. Reversing the bias is seen to reverse these changes back to the original state. This property has been utilized to craft credible non-volatile memory materials called Conducting Bridge Random Access Memory or CBRAM [33, 34]. Similarly, these materials are also shown to respond to radiations with change in conductivity and come back to the original state when the radiation stops. This makes this material a prospective material for radiation dosimeter. The microscopic phenomena behind these interesting properties is a burgeoning field of research.

1.4 Common Descriptors of Amorphous Solids

Structure of amorphous solids is described in statistical sense *i.e.* using distribution functions. The most common distribution function is the pair distribution function (PDF) written as [35]:

$$g(\vec{r}) = \frac{1}{\rho N} \sum_i \sum_{j \neq i} \delta(\vec{r} - \vec{r}_i)\delta(\vec{r} - \vec{r}_j) \tag{1.4}$$

where ρ is the number density, given by ρ=N/V where N is number of atoms and V is the volume. $\vec{r}_i$ is the position of atom i with respect to the central atom.

The radial distribution function (RDF) is obtained by integrating out the angular dependance as [35]:

$$g(r) = \int \frac{d\Omega}{4\pi} g(\vec{r}) \tag{1.5}$$

and is given by

$$g(r) = \frac{1}{4\pi\rho r^2 N} \sum_{i \neq i} \delta(r - r_{ij}) \tag{1.6}$$

where r_{ij} is the distance between atom i and atom j. The RDF is widely used to describe the structure of amorphous systems. The first peak and the first minimum in RDF show the degree of short range order in the solid whereas the position of first peak (also

called the radius of first coordination shell) gives the bond length (for a system with only one atom type). The degree of medium range order in the solid dictates the form of intermediate peaks beyond the first coordination sphere. Since amorphous solids don't have long range order, $g(r)$ flattens out to a constant (=1) at long distances (e.g. 20 Å). For system with more than one species, partial pair correlation function $g_{\alpha\beta}(r)$ between species α and β are computed as

$$dn_{\alpha\beta} = 4\pi r^2 \rho_\beta g_{\alpha\beta} dr \tag{1.7}$$

where $dn_{\alpha\beta}$ gives the average number of β atoms between distance r and $r + dr$ from the centre α atom. ρ_β is the number density of β species. Total pair distribution function (PDF) is then obtained by taking weighted sum over partial PDFs.

RDF can be inferred from experiments as the Fourier transform of static structure factor S(q) [36],

$$g(r) = 1 + \frac{1}{2\pi r \rho_o} \int_0^\infty q(S(q) - 1) sin(qr) dq \tag{1.8}$$

More discussion of structural analysis of amorphous solids can be found in [36, 37]. In many cases in this dissertation, I have used an open source program ISAACS [38] for structure analysis.

The electronic properties of amorphous systems is described through electronic density of states (EDOS). In this dissertation, we use density functional theory based calculations and the electronic states are single particle Kohn-Sham eigenvectors. The EDOS in that case represents the density of Kohn-Sham states plotted against the energy axis. For finite systems, the EDOS is discrete and can be expressed as [19]:

$$D(E) = \frac{1}{N} \sum_{i=1}^{N} \delta(E - E_i) \tag{1.9}$$

where N is size of the basis set and E_i is the eigenvalue of i^{th} eigenvector. The electronic band gap and the distribution of states around Fermi energy are important determinants of properties of these systems.

The electronic states in amorphous materials are not all extended as they are in crystals. This is a direct consequence of the disorder present in the structure. The localization of electronic states can be quantified in several ways. In this dissertation, we extensively use Inverse Participation Ratio (IPR) [7, 39] as the measure of localization of electronic states. We compute IPR of the n^{th} electronic state ψ_n as,

$$I_n = \frac{\sum_{i=1}^{N_{basis}}(\langle\psi_n|\phi_i\rangle)^4}{(\sum_{i=1}^{N_{basis}}(\langle\psi_n|\phi_i\rangle)^2)^2} \tag{1.10}$$

where ϕ_i is a basis vector. In this formulation, IPR assumes values between 0 to 1, where 1 corresponds to the most localized state.

1.5 Dissertation Outline

The rest of the dissertation is organized in the following way: In Chapter 2, the method of gap sculpting is developed and its applications within tight-binding framework to model amorphous silicon and amorphous carbon are presented. In Chapter 3, we extend the application of gap sculpting to *ab initio* calculation and present a scheme of modeling insulator-metal transition for silver doped chalcogenide glass. In Chapter 4, first principles studies of mechanism of electronic conduction in a-$GeSe_3Ag$ is presented and results from explicit simulation of Ag nanowires in glassy matrix are discussed. In Chapter 5, response of a-$GeSe_3Ag$ to radiation impact is discussed within the framework of empirical MD simulation. In the last chapter (Chapter 6), the coupling between electron states and thermal vibrations of lattice is discussed within the framework of first principles calculations. Much of the text of the chapters that follow are from my published works cited here: [40, 41, 42, 43, 44].

2 Gap Sculpting

The work presented in this chapter has been published in (i) **Prasai, K., Biswas, P., and Drabold, D. A. (2015). Sculpting the band gap: a computational approach.** Scientific reports 5, 15522. (ii) **Prasai, K., Biswas, P., and Drabold, D. A. (2016). Electronically designed amorphous carbon and silicon.** physica status solidi (a), 213(7), 1653-1660. (iii) **Prasai, K., Biswas, P., and Drabold, D. A. (2016). Electrons and phonons in amorphous semiconductors.** Semiconductor Science and Technology, 31(7), 73002-73015.

Here, we offer a method of including *a priori* electronic information in molecular dynamics (MD) simulations. This method provides a novel tool for structural modeling and materials design by gap engineering.

2.1 Motivation for Structural Modeling

Computer models of disordered semiconductors have usually fallen short of realistically representing the material in that these models often include too many defects (e.g. miscoordinated atoms, strained bonds or misaligned bond angles). These imperfections drastically impact electronic structure of these models making them inconsistent with experimental results, usually in the form of localized electronic states in the band gap region. The details of the nanometer-scale structure of an amorphous solid are not uniquely defined for these materials since it is not the global minimum of energy. In a celebrated work, Stillinger has shown that the number of structural energy minima scales exponentially with the system size [45]. Since experimental data reflect an ensemble average of physical observables from a huge set of low-lying energy minima, it is possible to successfully sample these configurations aided by external information in order to improve the realism of atomistic simulations and the quality of structural models. Atomistic simulations have taken the approach of using *a priori* knowledge about the

system (in the form of experimental information) to reduce the search space. These include various types of Reverse Monte Carlo (RMC) schemes that use diffraction data [46, 47, 48], diffraction data and constraints of spatial homogeneity [49], and diffraction data as well as information from electronic structure [50, 51] and nuclear magnetic resonance spectra [52]. Recently, an approach of including ionic forces "Force-Enhanced Atomic Refinement" (FEAR) has emerged [53].

Recent works have shown that imposing spatial homogeneity as a modeling constraint had a dramatic effect in improving models of a-Si, solid C_{60} and other systems [49, 54]. These workers invert the structural data (e.g. from scattering experiments) and use the reverse monte-carlo (RMC) approach to implement the constraint. The modeling of amorphous semi-conductors by enabling electronic constraints can also be viewed as imposing "electronic homogeneity" (in particular, by eliminating localized eigenstates in the gap region) for improving the structural models.

2.2 Motivation for Materials Design

In the theory of complex materials, one frequently confronts the following question: "Given particular optical properties (for example, extent of an optical gap or lack thereof), what atomic coordinates provide the desired properties?". This is an inverse problem, and requires a computational scheme that efficiently explores the configuration space and leaves us with an atomistic model satisfying our conditions. A way to approach this problem is to construct a large number of models using some random process, and keep promising candidates. While this can be effective for small systems (crystals with a small unit cell), it is impractical for more complex systems like amorphous materials. In some cases, the emphasis is not to construct a full structural model from scratch, but rather to improve an existing model by imposing additional atomistic information on the model. A

simple example is to generate a model of *a*-Si with a clean optical gap from an amorphous silicon network with defect states in the gap region.

There are diverse motivations for these calculations. The most obvious reason is to find materials optimized for photovoltaic (PV) applications, i.e. tuning a band gap to the solar spectrum, for example. It is also possible to induce metallization via gap tuning: compelling the density of states to be large at the Fermi level would significantly increase the conductivity of the model to induce transition to the metallic state. It also provides an effective means to discover the structural signatures of photodarkening or photobleaching, much studied effects in chalcogenide glasses [55]. For phase-change computer memory materials, the optical contrast between the amorphous and crystalline phases is fundamental, and these techniques should enable additional insight into the processes.

2.3 Theory

We adopt tight-binding Hamiltonians and employ Hellmann-Feynman forces [19, 56] in a novel way to determine structures with desired optical gap. Recall that the spatially non-local part of the interatomic force, the band-structure force, has the form:

$$\vec{F}_{\alpha}^{BS} = -\sum_{i}^{occ} \langle \Psi_i(r) | \frac{\partial H}{\partial R_\alpha} | \Psi_i(r) \rangle = -\sum_{i}^{occ} \frac{\partial \lambda_i}{\partial R_\alpha} \equiv \sum_{i}^{occ} \vec{F}_{i,\alpha}^{BS}. \tag{2.1}$$

Here i indexes eigenvalues (or bands) and runs through all occupied states, R_α are the $3N$ positional degrees of freedom, H is the Hamiltonian, and Ψ_i is an eigenvector. If one considers individual terms in the sum in Eq.(2.1), the term $\vec{F}_i^{BS}$ represents the contribution from the i^{th} eigenvalue (or band) to the total band-structure force. In effect, $\vec{F}_i^{BS}$ is a gradient for the i^{th} energy eigenvalue λ_i. As such, $\vec{F}_i^{BS}$ provides the direction in the 3N-dimensional configuration space of most rapid change of λ_i. Thus, to shift λ_i to higher (lower) energies, we should move atoms incrementally along the direction $-\vec{F}_i^{BS}$ ($+\vec{F}_i^{BS}$). For incremental displacements δR_α along this gradient, the shift $\delta\lambda_i$ of an eigenvalue λ_i

can be written as $\delta\lambda_i = \sum_\alpha -\vec{F}^{BS}_{i,\alpha}\ \delta R_\alpha$. To this end, we introduce the term *gap force* for state i to indicate the force (negative nuclear gradient) associated with eigenvalue λ_i. We exploit such forces to push eigenvalues out of a spectral range that we wish to be free of states. Our modified or biased dynamics follow from a Lagrangian $\mathcal{L} = T - \Phi$, in which $T = \frac{1}{2}\sum_{\alpha=1}^{3N} m_\alpha \dot{R_\alpha}^2$, and

$$\begin{aligned}\Phi(R_1, R_2 \ldots, R_{3N}) &= \sum_i f_i \langle\Psi_i|H|\Psi_i\rangle + U_r \\ &+ \sum_i{}' \gamma g\left(\langle\Psi_n|H|\Psi_n\rangle - \varepsilon_f\right) \end{aligned} \tag{2.2}$$

The sum in the last term in Eq. (2.2) is restricted to the energy range we wish to clear of states i.e. in the spectral range $\lambda_n \in [E_{min}, E_{max}]$. f_i is the occupation number of i^{th} energy level. The parameter γ controls the strength of the gap force, g is either +1 or -1 and it determines whether the state is pushed to the conduction edge or to the valence edge. In the equation above, ε_f is the Fermi energy, and U_r is the repulsive ion-ion interaction. The force associated with the α^{th} degree of freedom is given by,

$$\vec{F}^{bias}_\alpha = \vec{F}^{BS}_\alpha + \vec{F}^{ion}_\alpha + \vec{F}^{gap}_\alpha, \tag{2.3}$$

which can be used to obtain stable local minima by minimizing the total energy and forces via MD simulations and/or relaxations. In the tight-binding formulation, the forces on the right-hand side of (Eq. 2.3) are:

$$\begin{aligned}\vec{F}^{BS}_\alpha &= -\sum_i^{occ} f_i \langle\Psi_i(r)|\frac{\partial H}{\partial R_\alpha}|\Psi_i(r)\rangle \\ \vec{F}^{ion}_\alpha &= -\frac{\partial U_r}{\partial R_\alpha} \\ \vec{F}^{gap}_\alpha &= -\sum_{i=E_{min}}^{E_{max}} \gamma g(\lambda_i)\langle\Psi_i|\frac{\partial H}{\partial R_\alpha}|\Psi_i\rangle\end{aligned}$$

Here, choosing $g = +1$ will push the corresponding state to valence edge and choosing $g = -1$ will push it to conduction edge. We show empirically that the method works well even for mid-gap states near ε_F. We have observed that the method is also applicable in the opposite mode: to *maximize* the density of states at the Fermi level by shepherding eigenvalues toward the Fermi level [43]. This might, for example, introduce new structural features and produce models with interesting electrical conductivity.

Naturally, there is no *a priori* guarantee that a model with preferred electronic properties should be a minimum of the total energy functional. To ensure that the model is at equilibrium, we have adopted a quench and relax procedure in which biased dynamics is employed to push the system toward a configuration with preferred electronic optical gap (by using "gap forces" described above to drive states away from the desired spectral gap into the valence or conduction bands), and slowly quenching the diffusive dynamics so that the system may explore many configurations as its dynamics is gradually arrested. The system is then relaxed with physical forces to obtain a strong energy minimum and coordinates that yield the prescribed electronic gap.

2.4 Examples in Tight Binding Approximation

We demonstrate our method by modeling amorphous silicon (*a*-Si) and tetrahedral amorphous carbon (*ta*-C). These are well known to be difficult to model and to obtain a well-defined gap. We demonstrate the biased dynamics using the tight-binding parametrization for carbon by Xu *et al.* [17] and that of Goodwin, Skinner and Pettifor [18] for Si. In a conventional melt-quench method, a well equilibrated liquid model is quenched below the glass-forming temperature by performing dissipative dynamics. We take the same point of view here, except that we bias the dissipative dynamics toward a configuration with fewer states in the gap region. The biasing is done by adding the gap forces to the band-structure and ionic forces as given by Eq. (2.3).

All models are then compared to the corresponding Wooten, Weire, Weiner (WWW) models [11, 57], which are widely recognized as best models of *a*-Si and *ta*-C. This is a proxy for comparing to experiments, since the agreement of WWW model with experiments is well established [58, 59, 60]. Furthermore, our results are substantiated by density functional theory (DFT) calculations [22, 23, 24, 25, 26] in both examples.

2.4.1 Amorphous Carbon

Amorphous carbon is technologically important and has intriguing microscopic structure. Carbon forms strong bonds in both sp^2 and sp^3 environments and can be prepared in various forms. Sputtering and evaporation usually produce disordered phases that are rich in sp^2 bonds, whereas mass-selected ion beam deposition produce a disordered phase with more than 90% sp^3 character [61]. Structural, electronic and optical properties of these materials are of great technological and scientific importance, which have led to considerable works in this field [17, 61, 62, 63, 64, 65, 66, 67, 68, 69, 70, 71]

There have been many attempts of modeling amorphous carbon [68, 17, 66, 67, 71]. Particularly, sp^2 -bonded carbon is modeled and characterized by using empirical potential [68], tight-binding approximation [17] and *ab initio* methods [66, 67, 71] with a varying degree of success. Tight-binding MD simulations were employed in Ref. [69, 72] to model diamond-like carbon but the authors used, as a critical requirement, much higher density than the experimental density of 2.9 gm/cm^3 [66]. Drabold *et al.* used first-principles methods to model *ta*-C at the experimental density and produced 64-atom models of *ta*-C with 91% 4-fold coordination [66]. Djordjevic, Wooten and Thrope used the bond-switching algorithm of Wooten, Weaire and Winer [11] to prepare perfectly tetrahedral models of *a*-C [57]. However, modeling alloy systems with a significant fraction of both sp^2 - and sp^3 -bonded carbon has not been accomplished to our knowledge.

It has been observed that systems with a higher fraction of sp^3 -bonded C atoms have a wider electronic gap than its sp^3 counterpart. For example, evaporated *a*-C has a gap of 0.4-0.7 eV, whereas diamond-like *a*-C has gap of 0.5-1.5 eV (see ref. [61] and table 1 therein for details). This correlation between the gap size and concentration of sp^3 -bonded atoms is valuable and can be used as *a priori* information to bias the dynamics in order to tune the concentration of sp^3 -bonded atoms in a model. Here, we have implemented such a biased dynamics using the tight-binding approximation and reported models of disordered carbon, which consist of both sp^2 - and sp^3 -bonded carbon atoms at various concentrations.

It is notable that imposing electronic information not only opens up the electronic gap, but also influences the structural properties by changing the character of carbon-carbon bonding from sp^2 to sp^3 . The fraction of sp^3 -bonded atoms increases with increasing γ, and thereby provides a previously unavailable knob to tune the sp^3 concentration in the network – *in this mode using an electronic constraint to obtain a desired structural result*. For this calculation, we relaxed Djordjevic's model [57] with TB Hamiltonian and used the size and location of the gap of the relaxed model as required electronic information for biased MD simulations.

We have chosen three densities to conduct biased dynamics: 2.9, 3.2 and 3.5 gm/cm^3. The conventional melt-quench MD simulations at these densities produce amorphous carbon with more than 90% sp^2 concentration as observed in our present work and in previous work by others [73, 70]. Melt-quench procedure at higher pressure has been shown to produce a strong sp^3 character of C-C bonding in the liquid state [73, 74]. On the other hand, quenching at higher densities have been employed to force the models into a diamond-like structure [69, 72].

The models reported here are constructed by quenching from equilibrated liquid C. For each density, a cubic supercell of 216 atoms in diamond lattice with periodic boundary

condition was heated beyond its melting temperature. (We note that, with increasing density, the cell needs to be heated to higher temperature and for longer duration in order to impart sufficient disorder to fully melt the cell. Accordingly, we heated the cell at density 2.9 gm/cm^3 to 7000 K and then equilibrated it at that temperature for 7.5 ps. The cell at density 3.2 gm/cm^3 was heated to 9000 K and equilibrated for long time following to successive equilibrations at 7000 K and 8000 K respectively. The cell at density 3.5 gm/cm^3 was heated to 10000 K and the equilibrated after two successive equilibrations at 8000 K and 9000 K respectively.) We verified that the these well-equilibrated liquid models bear the standard signatures of liquid carbon (radial distribution, bond-angle distribution, coordination numbers and electronic structure) reported in [73, 74]. We have observed that conventional TBMD has led to results, which are consistent with the earlier results obtained by others using this Hamiltonian.

To produce gap-engineered models, we bias the quenching from the liquid by modifying the TB forces according to Eq. (2.3). To impart diamond like character in the network, we biased the dynamics towards the electronic structure of a perfectly tetrahedral amorphous carbon model (We rescaled Djordjevic's perfectly tetrahedral model [57] to densities 2.9 gm/cm^3 , 3.2 gm/cm^3 and 3.5 gm/cm^3, then relaxed the rescaled models using Xu's tight-binding Hamiltonian [17] until the forces on each atom vanishes. These relaxed models have gap of size 3.14 eV, 3.80 eV and 4.10 eV respectively. We used the size and location of these gaps at the respective densities to bias the dynamics (i.e. the values of E_{min} and E_{max} in Eq. (2.4) were set equal to the gap limits of these relaxed models). The strength of the biasing forces were tuned by appropriately choosing γ.) Finally the quenched models at 600K were relaxed to their local minimum using true (unbiased) TB forces. Hence, the final structures are true inherent structures of the carbon system, and the models are stable.

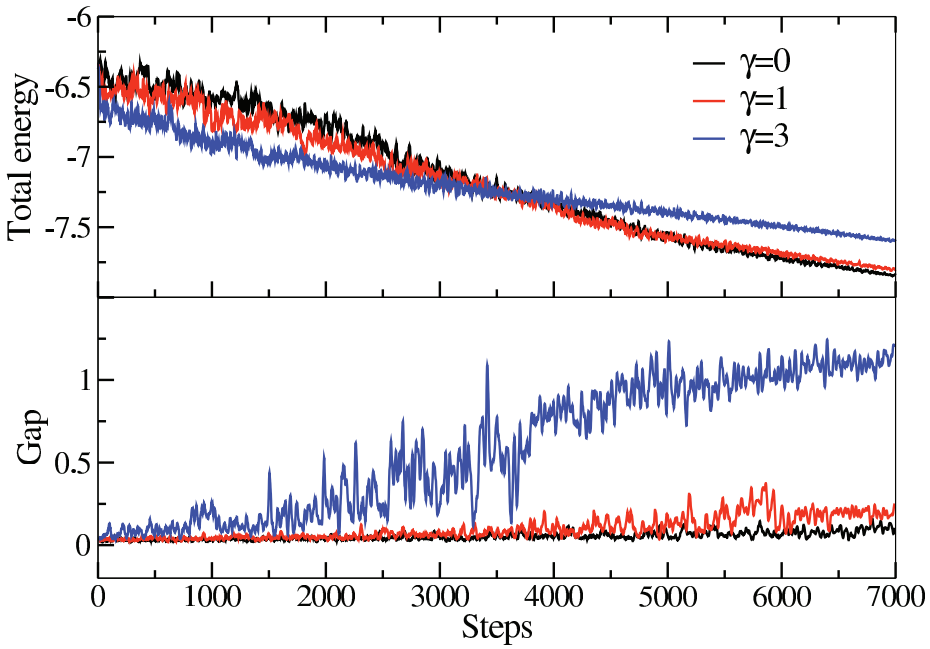

Figure 2.1: Evolution of total energy and band gap in gap sculpting. (Top) The total energy per atom of the system upon quenching for 7000 K to 600 K at density 2.9 gm/cm^3. For small γ, the energy penalty is very small. Note that these models are relaxed using unbiased TB forces (i.e. $\gamma = 0$) following the quench to ensure that we obtain a "true" minimum. The total energy of these systems after relaxation is -7.92 eV/atom, -7.88 eV/atom and -7.70 eV/atom for γ= 0, 1 and 3, respectively. (Bottom) The evolution of the gap during the quench. For clarity and reduction of noises in the data, a running-window average of the gap values are presented here.

We note that for small γ, the energy penalty of biasing the dynamics is small. Figure 2.1 (top) shows the total energy per atom during quenching. The energy penalty is reconciled to some extent by the relaxation with respect to true forces and the final models are less than 0.15 eV/atom apart for $\gamma = 1$. The dynamics steers the network to wider gap configurations as seen in figure 2.1 (bottom) and that has a strong effect on the nature of bonding in the network that results. We see that for increasing value of γ at a particular density, the concentration of sp^3 bonds increases. For density 2.9 gm/cm^3, which is the experimental density of ta-C, we get 22.7%, 48.1% and 55.5% sp^3 character in the models for γ= 1, 2 and 3 respectively, compared to 6.5% sp^3 -bonded atoms for γ=0 (see figure

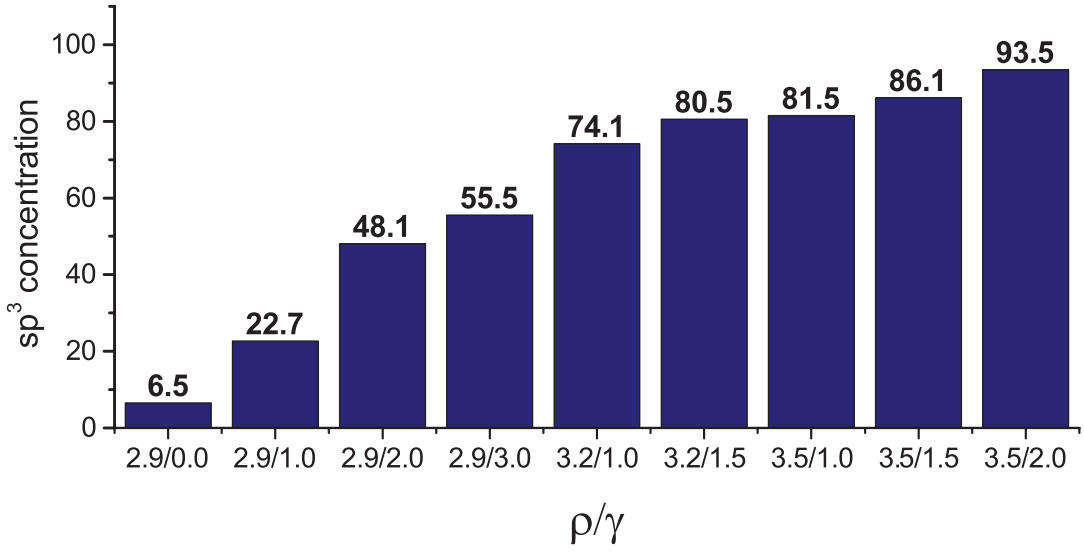

Figure 2.2: The concentration of tetrahedrally-bonded carbon atoms in the relaxed models. The labels along the horizontal axis designate the density (ρ) and the strength of gap forces (γ) used to bias the forces. For clarity, (ρ,γ) is written as ρ/γ.

2.2). We find that the leverage on γ declines after γ=3 because further increase in γ significantly alters the dynamics and does not increase the sp^3 concentration.

Similar behavior is observed at higher densities. At density 3.2 gm/cm^3, the final models have sp^3 concentration of 74.1% and 80.5% for γ=1 and 1.5, respectively. Similarly, biased dynamics at density 3.5 gm/cm^3 produced models with sp^3 concentration of 81.5%, 86.1% and 93.5% for γ= 1, 1.5 and 2 respectively. It is important to note here that, while increased pressure at 3.2 gm/cm^3 and 3.5 gm/cm^3 has certainly helped to align the dynamics to tetrahedral geometry, an application of biasing forces is absolutely necessary to obtain to these models. Our calculations have shown that unbiased dynamics at all three densities presented here produce a predominantly sp^2 network. The alloy systems with comparable concentrations of sp^2 and sp^3 have the character of both types of network. Figure 2.3 shows the RDF of the relaxed models with

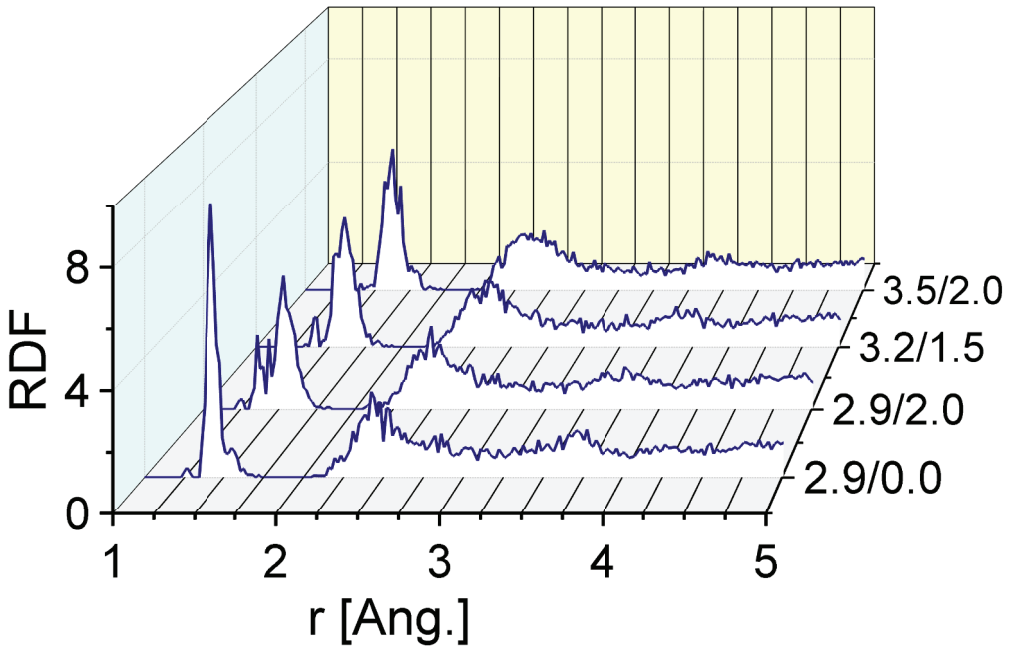

Figure 2.3: The radial distribution function of various relaxed models of amorphous carbon. The labels along the horizontal axis designate the density (ρ) and gamma (γ) used to bias the TB forces. These models correspond to increasing concentration of tetrahedral character in the network. This change in character is reflected in the gradual widening and shift of the first RDF peak from 1.41 Å (for lowest sp^3 density) to 1.53 Å (for highest sp^3 density).

48.1% and 80.5% sp^3 bonding respect to predominantly sp^2 and sp^3 networks. This demonstrates the magnitude of structural consequences of electronic constraints in atomistic simulations.

In figure 2.4, we compare some key features of the models obtained using biased and unbiased dynamics at density 3.5 gm/cm^3. To be able to appreciate the sp^3 character in the network, we compare these two models with Djordjevic's model. We see that the biased model very closely resembles the radial distribution function of Djordjevic's model and has the bond length of 1.51 Å (original Djordjevic model has bond length of 1.54 Å [57].) Similarly, the unbiased model registers a peak in the bond-angle distribution (BAD) around $\approx 120^\circ$, characteristic of sp^2 networks. The bond-angle distribution of the biased

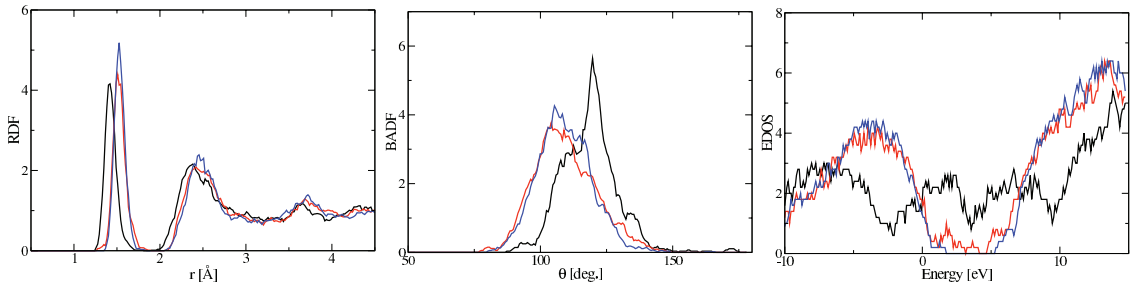

Figure 2.4: Radial distribution function (RDF), bond angle distribution function (BADF) and electronic density of states (EDOS) for unbiased model (γ=0, black), biased model (γ=2, red) and relaxed Djordjevic's model (blue) [57] at density 3.5 gm/cm^3. The biased model plotted here has 93.5% four-coordinated C atoms and resembles closely with Djordjevic's model.

model closely resembles that of relaxed Djordjevic's model. Finally, we show that the biased model has the diamond-like electronic structure.

2.4.2 Amorphous Silicon

A realistic model of disordered silicon is needed in order to understand the material for technological as well as scientific purposes. Amorphous silicon has electronic and optoelectronic applications and this material has long been used by the community as archetypal material to understand various structural, electronic as well as vibrational properties of disordered materials. It has been difficult to make reliable models of *a*-Si using MD simulations even with the most advanced *ab-initio* methods. Models of *a*-Si due to Wooten, Winer and Weire [11, 57] are widely recognized as among the best models so far. Their agreement with structural and electronic properties of bulk *a*-Si is well established [58, 59, 60]. But, these models are created using a guided metropolis algorithm (the "bond-switching method") which is obviously less general and intuitive than the conventional melt-quench method. The later mimics the glass formation process by performing dissipative dynamics on well-equilibrated liquid models. But, the models

of *a*-Si created using the melt-quench method usually show many remnants of the liquid silicon (*l*-Si): too many floating, strained and dangling bonds leading to far too many defect states in the electronic gap region. Silicon, despite its ubiquity in nature and the literature is particularly difficult to model because of its over-constrained bonding topology.

In this example, we show again that *a priori* knowledge of the electronic gap can be coupled with the conventional TB forces to produce models of *a*-Si that are structurally and electronically superior to the models using conventional TB forces. Much of the method of conducting biased dynamics is similar to that used for *a*-C in previous section.

Here, we carry out the melt-quench method using the tight-binding Hamiltonian of Goodwin, Skinner and Pettifor [18]. The melt-quench process is similar to those used in earlier works [73, 75, 76, 16]. We started with a random collection of 216 atoms at a density of 2.33 gm/cm^3 and we equilibrated the system at 2500 K for 4 ps, followed by three successive equilibrations: at 2300 K for 2 ps, at 2100 K for 2 ps, at 1900 K for 2 ps. The system was then equilibrated at 1780 K (close to the melting point of Si) for 50 ps to arrive at *l*-Si model. We checked the *l*-Si model by computing its radial distribution function (RDF), bond-angle distribution function (BADF) and electronic density of states (EDOS). These calculations conform to earlier calculations on *l*-Si by Kim and Lee [75]. We then obtained 25 distinct configurations of *l*-Si by equilibrating the model at 1780 K for 25 ps and capturing the instantaneous configurations at the interval of 1 ps. These 25 configurations are then quenched to 300 K at a rate of $\approx$ 100 K/ps using biased dissipative dynamics. We used the electronic gap of WWW model as the target gap and used $\gamma = 1$. The models are then relaxed by damping the velocity of atoms by 1% at each step until the forces on the atoms become smaller than 0.05 eV/Å. We point out here that the biased dynamics is used only while quenching the system and, for the particular choice of $\gamma = 1$, the average magnitude of the biasing force remains smaller than 18% of the average TB

force throughout the quench. For the sake of comparison, we also quenched all 25 models using only the conventional TB forces. The quenched models were then relaxed using the method described above.

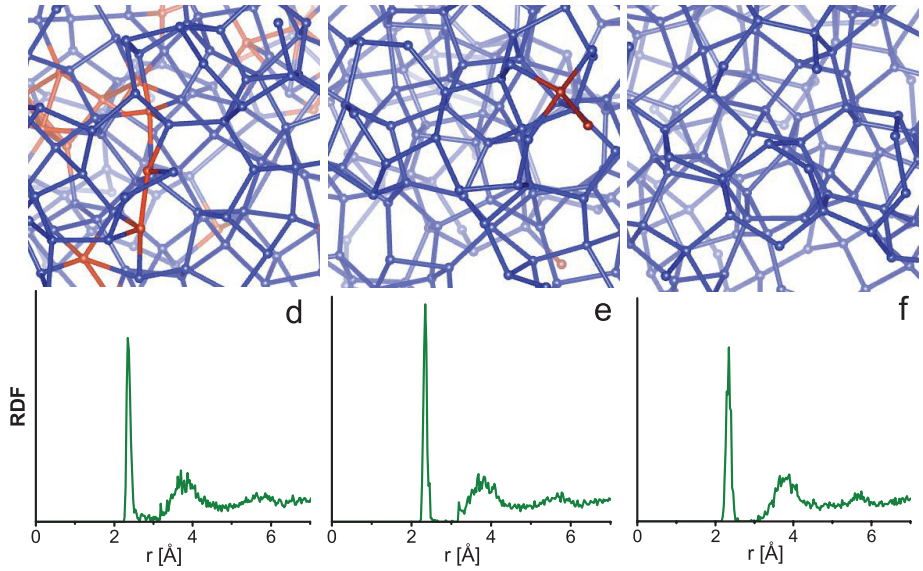

Figure 2.5: The structural features of the TBMD, biased TBMD and WWW models of *a*-Si (a, b and c respectively). Mis-coordinated atoms and their bonds are visualized in red and normally coordinated atoms are in blue. Cutoff radius of 2.8 Å was used to define a bond for all three models. d, e and f: Radial distribution function (RDF) of these models are plotted in the same order.

We have examined structural and electronic features of an array of relaxed models following biased quenching runs (referred to as 'biased TBMD models'), as well as the corresponding conventional TBMD models (referred to as 'TBMD models'). The merits of these two ensembles of models can be determined by validating them against the WWW model.

Biasing forces skew the dynamics towards a structure with a clean gap. In direct consequence of this, the network organizes with higher structural order while still in a topologically disordered state of tetrahedral character. (This leads us to suspect that

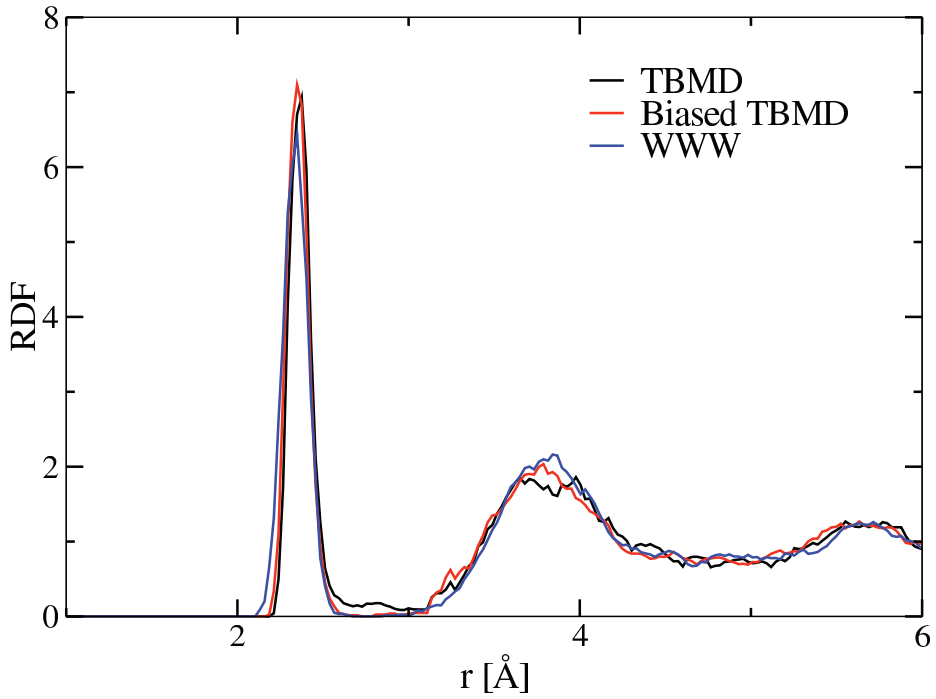

Figure 2.6: Radial distribution functions of a TBMD model (γ=0), biased TBMD model (γ=1) and WWW model [11]. The biased model has a clean first minimum and closely resembles with the WWW model.

simulations of crystallization might be significantly accelerated in this framework.) Durandurdu *et al.* [77] have pointed out that models with a cleaner gap (narrower band tails) are also the ones with narrower bond-length and bond-angle distributions [77]. The radial distribution function of the biased model presents significant structural order, indicated by a clear first minimum (see Fig. 2.6) compared to that of the unbiased model. The biased model clearly agrees more closely with the RDF of the WWW model. The structural order is also indicated by the bond-length and bond-angle distributions. The biased model presents a narrower bond-angle distribution as evident in figure 2.7. We note that the biased model is free of the presence of small (60 degrees) bond angles that arise in conventional MD. We have computed the variance of bond length for both TBMD models, as well as for the biased TBMD models. We observe that out of 25 models sampled, 20 of

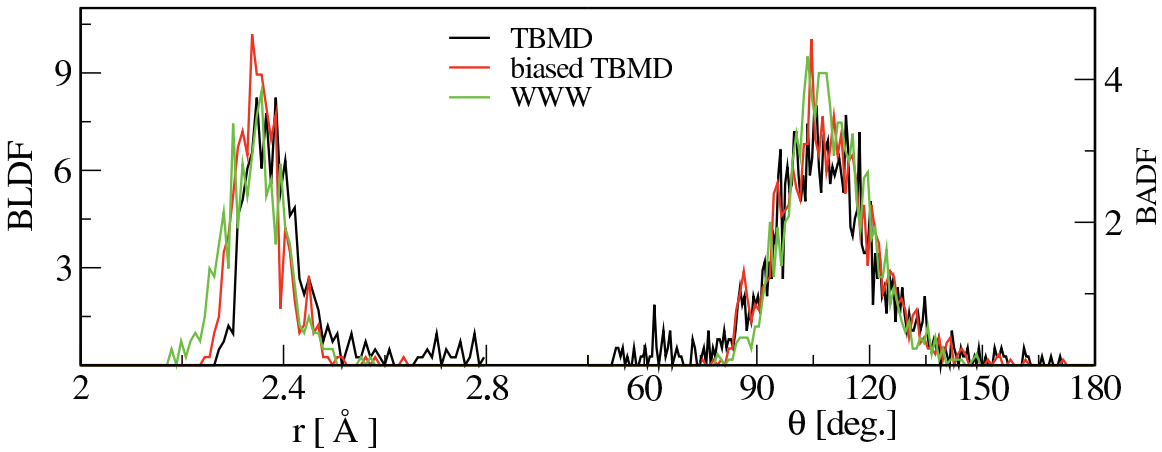

Figure 2.7: The bond-length (left) and bond-angle (right) distribution functions of TBMD model (γ=0), biased TBMD model (γ=1) and the WWW model [11]. The biased model is nearly free of over-coordinated atoms that give rise to small bond angles and long bond lengths in TBMD model. Biased model closely resembles with WWW model.

the biased models show a smaller variance in bond length. Also, the number of 4-coordinated atoms is higher for models following the biased dynamics in 19 out of 25 instances (see Fig. 2.8).

The electronic density of states of the relaxed models is plotted in figure 2.9. It is observed that the biased TBMD models have cleaner gap than the TBMD models. Note that for the particular instance plotted in figure 2.9, the gap of biased model is wider than that of WWW model.

We characterized models described in this section in local density approximation (LDA) using density functional code VASP [22, 23]. Interestingly, the biased TBMD model has lower energy than the TBMD model. Similarly, biased model exerts cleaner gap in LDA. To study the dependence of the method on system size, we carried out the biased dynamics in 512 atom cell with the same quenching rate and biasing parameter. For five out of five samples that we tested, biased dynamics produced models with higher concentration of 4-folds and cleaner gap.

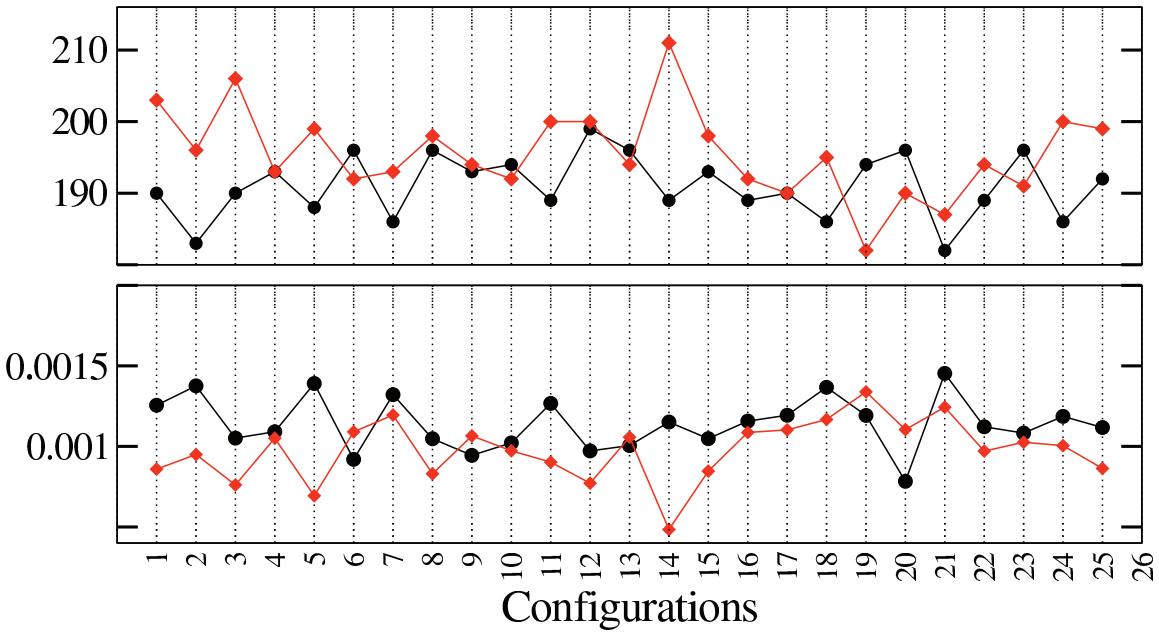

Figure 2.8: (Top) The number of four-coordinated Si-atoms in models that are quenched and relaxed from 25 different liquid models at 1780 K. For models plotted in red, biased TB forces with $\gamma = 1$ were used during quenching whereas for those in black, conventional (unbiased). TB forces were used. Both batches of quenched models were relaxed using unbiased TB forces. (Bottom) The variance of bond lengths for the corresponding models.

2.5 Density Functional Approach

This approach of gap sculpting is preferably performed using first principles calculations since tight-binding methods suffer from well-known problems of limited transferability. We have used VASP to carry out biased dynamics. As an example, we report here a wide band gap amorphous form of silicon that is structurally different from the tetrahedral continuous random network picture of *a*-Si. This structure is stable and has lower energy that its conventional counterpart.

We started with a random collection of 64 atoms and prepared a liquid model of silicon (*l*-Si). The system was heated to 1800 K for 2 ps and was then melted at various temperatures higher than 1800K for 10 ps. The system was then equilibrated at 1800K for

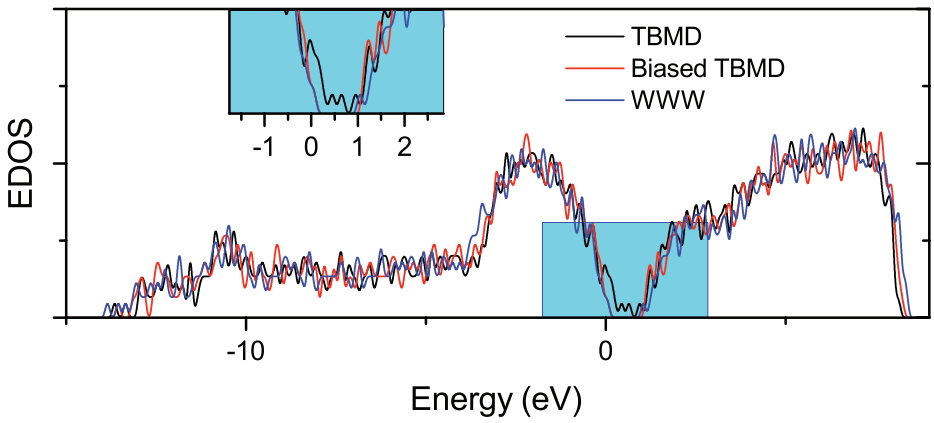

Figure 2.9: The electronic density of states of the unbiased model (γ=0), biased model (γ=1) and relaxed WWW model [11]. The unbiased model (labeled 'TBMD') registers few states in the gap while the biased model is free of defect states. The gap of the biased model is wider than that of the WWW model by $\approx$ 0.1 eV.

another 12ps. The liquid model so obtained was then quenched to 300K using biased forces. The band gap of the 64-atom WWW model was taken as reference to electronic gap. We tested 4 different biasing factors (γ = 0.0, 0.3, 0.5 and 1.0). We see that the biased dynamics gradually steers the model to configurations with larger electronic gap and the size of the gap roughly correlates with value of γ within reasonable limit (Fig. 2.10).

The quenched models are then relaxed to their nearest minimum using true LDA forces (γ = 0). We find that relaxed models so obtained have a band gap larger than conventional model by 0.24 eV (for γ = 0.3), 0.35 eV (for γ = 0.5) and 0.15 eV (for γ = 1.0). The band gap of our best model (that with γ = 0.5) is still smaller than that of WWW model of the same volume by 0.25 eV. We report the comparison of electronic EDOS and RDF of the model using γ = 0.5 with the conventional model (i.e. using γ = 0.0). The former has more structural defects in the form of floating bonds than the later and it is remarkable that these defects somehow do not register states in the gap. The

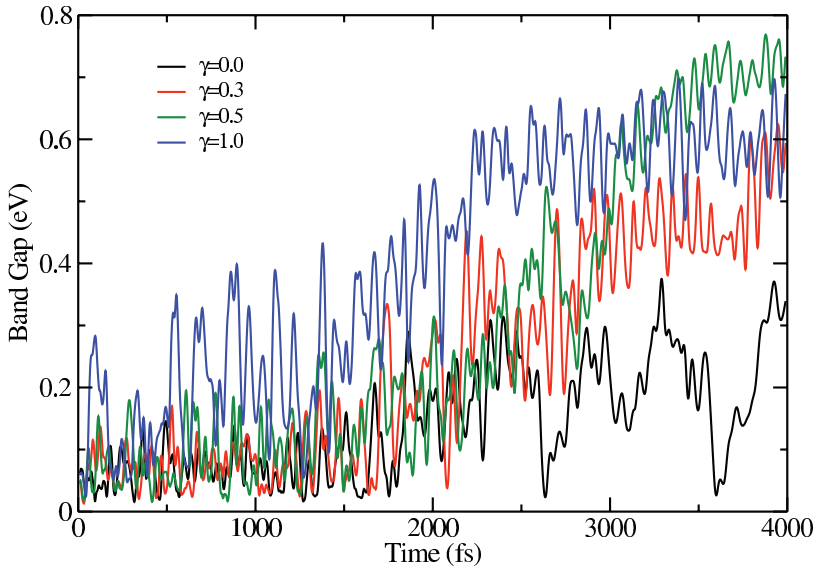

Figure 2.10: The band gap of the model during biased quenching from 1800 K to 300 K. γ represents the biasing factor, which remains constant throughout the quenching dynamics. For all data sets, a running window average is taken to reduce the noise.

structure with $\gamma = 0.5$ has lower energy than its conventional counterpart ($\gamma = 0$) by 0.02 eV/atom but has higher energy than WWW model of same volume by 0.07 eV/atom.

2.6 Discussion

Listed below are few comments on statistics and technical details. 1) As we have shown, our method is best employed in a "statistical mode"–unsurprisingly the final structures depend on the initial state. In some fraction ($\approx$ 20%), the method does not improve the gap in case of *a*-Si. We suppose that this may be due to the very simple rule of shifting atoms along gradients toward the nearest band edge, even for eigenvalues very near ε_f. 2) We have experimented with various γ, and have found no particular advantage to selecting $\gamma \neq 1$ to date. 3) Preliminary studies suggest that the results presented here also accrue for larger (512-atom) models. 4) For *a*-Si, we use *a priori* knowledge of the gap from the best available models. In the general case, one can define a gap by trial and

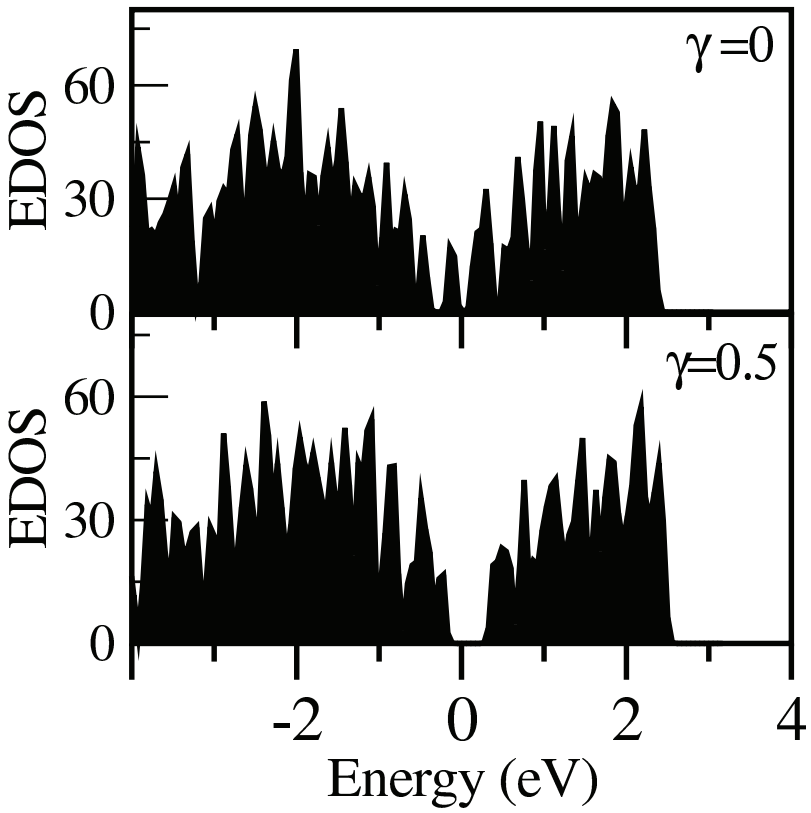

Figure 2.11: Electronic density of states (EDOS) of the relaxed models. The model indicated $\gamma = 0.0$ is constructed using unbiased first principles MD where as the one indicated $\gamma = 0.5$ is constructed using biased dynamics with $\gamma = 0.5$. The Γ-point gap is 0.64 eV for model with $\gamma = 0.5$, compared to 0.89 eV in WWW a-Si of the same volume.

error, with the choice being determined in part by a requirement that the physical forces vanish at the end.

As is the case with all methods, our approach has limitations: (1) We used standard orthogonal tight-binding Hamiltonians for the simulations. This is hugely limiting, since such Hamiltonians have only been devised and tested for a handful of systems, mostly elemental, and suffer from significant limitations with respect to transferability [78]. 2) Even in a density-functional framework, gap estimates from Kohn-Sham eigenvalues are spurious, though usually these account reasonably well for trends. With significant

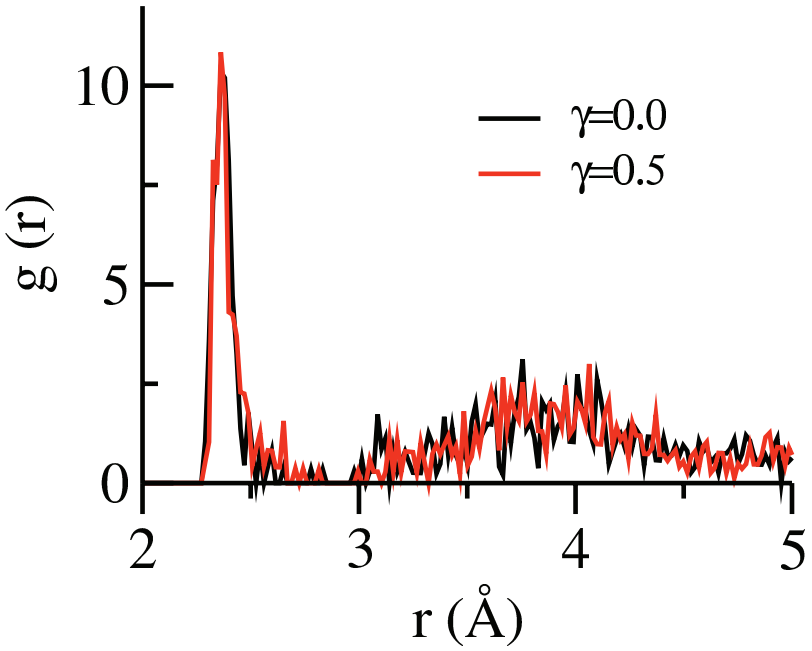

Figure 2.12: Radial distribution function (RDF) of the relaxed models. The model indicated $\gamma = 0.0$ is constructed using conventional molecular dynamics where as the one indicated $\gamma = 0.5$ is constructed using biased dynamics with $\gamma = 0.5$. The calculation was carried out with the plane-wave LDA code VASP

computational expense, these estimates may be improved *e.g.* with GW or Hybrid Functional schemes [19].

2.7 Conclusions

We demonstrate the utility of the method with two examples and suggest that the approach may be developed in promising ways. We show in a practical way how to include electronic information in structural modeling, and we prove that imposing electronic constraints leads to relaxed models in better agreement with structural experiments, particularly for the case of *a*-Si. The method can be used to make a nearly state-free gap, or to maximize metallicity. For *ta*-C, considerable flexibility is afforded by our approach in tuning sp^2/sp^3 ratios. Our method is highly efficient since it employs

Hellmann-Feynman (HF) forces [19, 56], which are the byproduct of any electronic structure simulations. We expect that the scheme will be useful for many other complex materials not only for discovering structures with desired gaps but also for imposing electronic constraints in modeling. This scheme opens the way for new avenues of materials engineering, especially for optical properties, and we expect it to have a broad impact when implemented fully with *ab initio* methods.

3 Insulator-Metal Transition in $GeSe_3Ag$ Glass

The work presented in this chapter has been published in **Prasai, K., Chen, G., and Drabold, D. A. (2017). Amorphous to amorphous insulator-metal transition in $GeSe_3$Ag glasses.** Physical Review Materials, 1(1), 015603.

3.1 Introduction

Metal-Insulator transitions (MIT) and their associated science are among the cornerstones of condensed matter physics [79]. In this chapter, we describe the atomistics of a technically important but poorly understood MIT in GeSe:Ag glasses, a prime workhorse of conducting bridge memory (CBRAM) devices [33, 34]. By *design*, we construct a stable conducting model from a slightly energetically favored insulating phase. Predictions are made for structural, electronic and transport properties. We demonstrate the utility of our gap sculpting method [40] as a tool of materials design.

We report here the metallic phases of amorphous $(GeSe_3)_{1-x}Ag_x$ at $x = 0.15$ and 0.25. These are canonical examples of Ag-doped chalcogenide glasses, which are studied in relation to their photo-response and diverse opto-electronic applications [31, 32]. Ag is remarkably mobile making the material a solid electrolyte and is known to act as "network-modifier" in these glasses as it alters the connectivity of network. Experiments have shown Se rich ternaries ($(Ge_ySe_{1-y})_{1-x}Ag_x$ with $y < 1/3$) to be phase-separated into Ag-rich Ag_2Se phase and residual Ge_tSe_{1-t} phase [30].

Using first-principles calculations, we show that stable amorphous phases with at least $\sim 10^8$ times higher electronic conductivity exist with only small (≈ 0.04 eV/atom) difference in total energy. These conducting states present the same basic structural order in the glass, but have a higher relative fraction of an a-Ag_2Se phase compared to the insulating states. It is known that amorphous materials are characterized by large numbers of degenerate conformations that are mutually accessible to each other at small energy

cost, but those usually have similar macroscopic properties. The remarkable utility of these materials accrues from states with distinct properties, nevertheless readily accessible to each other.

We discover the conducting phase of $GeSe_3Ag$ glass by *designing* atomistic models with a large density of states (DOS) near the Fermi energy [80]. This is achieved by utilizing Hellmann-Feynman forces from the band edge states, the theory of which has been developed in chapter 2. These forces are used to bias the true forces in *ab initio* molecular dynamics (AIMD) simulations to form structures with a large DOS at the Fermi level. The biased force on atom α, F_α^{bias}, is obtained by suitably summing Hellmann Feynman forces for the band edge states (second term in Eq. 3.1) with the total force from AIMD calculations, F_α^{AIMD}.

$$F_\alpha^{bias} = F_\alpha^{AIMD} + \sum_i \gamma_i \langle \psi_i | \frac{\partial H}{\partial R_\alpha} | \psi_i \rangle \tag{3.1}$$

Here, γ's set the sign and magnitude of the HF forces from individual states i. To maximize the density of states near ϵ_F, gap states closer to the valence edge will have $\gamma > 0$, whereas the states in the conduction edge will have $\gamma < 0$. The magnitude of γ determines the size of biasing force (with $\gamma = 0$ representing true AIMD forces). We have employed biased forces as an electronic constraint to model semiconductors and insulators in chapter 2 where the biasing is done in just the opposite sense: to force to states out of the band gap region.

3.2 Computational Approach

We start with conventional 240 atom models of $(GeSe_3)_{1-x}Ag_x$, x=0.15 and 0.25, at their experimental densities 5.03 and 5.31 gm/cm^3 [81] respectively. These were prepared using melt-quench MD simulations, followed by conjugate-gradient relaxation to a local energy minimum. The MD simulations are performed using the Vienna *Ab initio*

Simulation Package (VASP) [22, 23]. Plane waves of up to 350 eV are used as basis and DFT exchange correlation functionals of Perdew-Burke-Ernzerhof [27] were used. Brillouin zone (BZ) is represented by Γ-point for bulk of the calculations. For static calculations, BZ is sampled over 4 k-points. These models fit the experimental structure factor reasonably well (Figure 3.1).

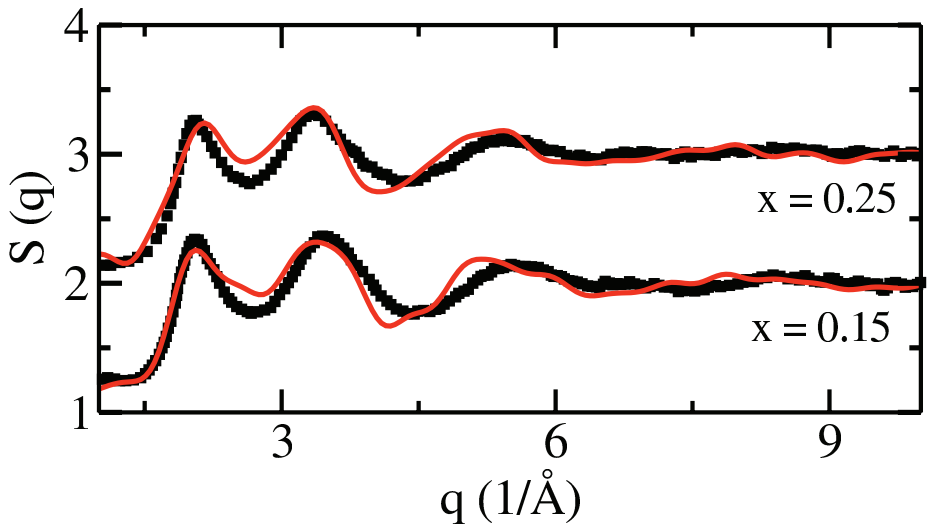

Figure 3.1: The structure factor of $(GeSe_3)_{1-x}Ag_x$ models (solid red line) compared with experiment (black squares)[81]

We obtain conducting conformations by annealing the starting configurations using biased forces at 700 K for 18 ps. The electronic states in the energy range [ϵ_F–0.4 eV, ϵ_F+0.4 eV] are included in the computation of bias force and $\gamma = 3.0$ is used. The bias potential ($\Phi_b(R_1, .., R_{3N}) = \sum -\gamma_i \langle\psi_i|H(R_1, .., R_{3N})|\psi_i\rangle$) shepherds the electronic states at the band edges into the band-gap region. Since we want any proposed metallic conformation to be a minimum of the unbiased DFT energy functional, we relax instantaneous snapshots of biased dynamics (taken at the interval of 0.2 ps, leaving out the first 4 ps) to their nearest minima using conjugate gradient algorithm with true DFT-GGA forces. We study all relaxed snapshots by i) gauging the density and localization of states

around Fermi energy and, ii) testing the stability of the configurations by annealing them at 300 K (*n.b.* glass transition temperatures (T_g) are 488 K and 496 K for compositions x=0.15 and 0.25 respectively [82]). At each composition, we selected five models that display a large density of extended states around Fermi energy and are stable against extended annealing at 300 K as the 'metallized' models. These metallized systems are, on average, 0.040±0.009 eV/atom above their insulating counterparts.

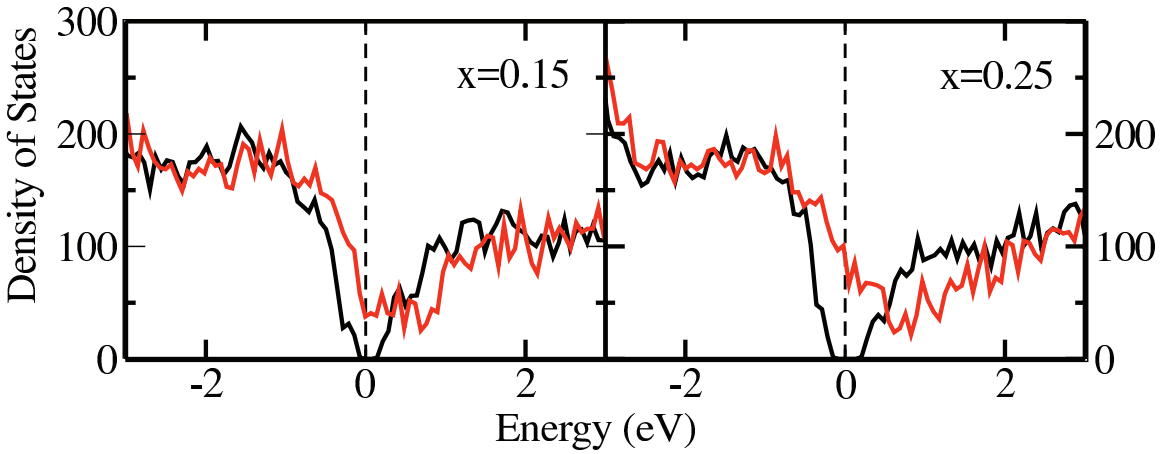

Figure 3.2: The electronic density of states (DOS) of the insulating model (black curve) and the metallized model (red curve). Energy axis is shifted to have Fermi level at 0 eV (the broken vertical line)

3.3 Results

3.3.1 Electronic Structure and Transport

The metallized models, by construction, exhibit a large density of states around the Fermi energy (Figure 3.2) whereas the insulating models display small but well defined PBE [27] gap of 0.41 eV and 0.54 eV for x=0.15 and 0.25 respectively. For disordered materials, a high DOS at ϵ_F *alone* may not produce conducting behaviour since these states can be localized (example: amorphous graphene, [83]). We gauge the localization of

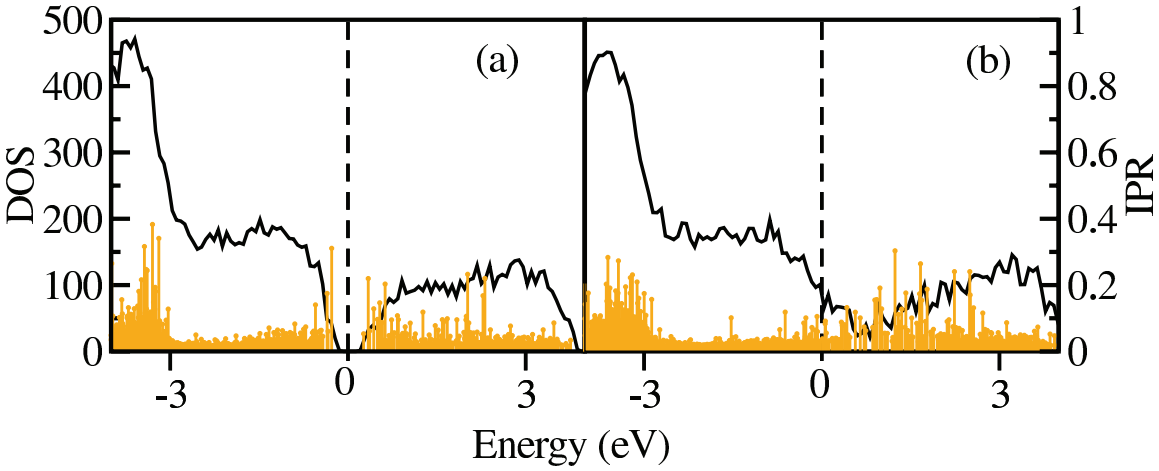

Figure 3.3: The (black curve) electronic density of states (DOS) and (orange drop lines) Inverse Participation Ratio (IPR) of the insulating model (a) and the metallized model (b). Energy axis for all datasets is shifted to have Fermi level at 0 eV (highlighted by the broken vertical line)

these states by computing inverse participation ratio (IPR, [7]) (plotted for x=0.25 system in Figure 3.3) and show that these states *are* indeed extended. We compute the electronic conductivity [$\sigma(\omega)$] using the Kubo-Greenwood formula (KGF) in the following form:

$$\sigma_k(\omega) = \frac{2\pi e^2\hbar^2}{3m^2\omega\Omega}\sum_{j=1}^{N}\sum_{i=1}^{N}\sum_{\alpha=1}^{3}[F(\epsilon_i,k) - F(\epsilon_j,k)] \\ |\langle\psi_{j,k}|\nabla_\alpha|\psi_{i,k}\rangle|^2\delta(\epsilon_{j,k} - \epsilon_{i,k} - \hbar\omega) \tag{3.2}$$

It has been used with reasonable success to predict conductivity [84, 85, 86]. Our calculations used 4 k-points to sample the Brillouin zone. To compensate for the sparseness in the DOS due to the size of the supercell, a Gaussian broadening (δE) for the δ-function is used. We note that the choice of δE between 0.01 eV and 0.1 eV does not significantly alter the computed values of DC conductivity [$\sigma(\omega = 0)$] (Figure 3.4). For the choice of δE=0.05 eV (which is small compared to the thermal fluctuation of Kohn-Sham states for disordered systems at room temperature. For a heuristic theory, see

[44]), the DC conductivity of metallic models are of the order of $10^2\ \Omega^{-1}cm^{-1}$ at both concentrations. For the insulating model at x=0.15, this value is of order $10^{-6}\ \Omega^{-1}cm^{-1}$ whereas for insulating model at x=0.25, this value is lower but can not be ascertained from our calculations. We find that the metallized models show, at least, $\sim 10^8$ times higher conductivity than the insulating models. The computed conductivity for metallic models are comparable to the DC conductivity values of liquid silicon ($\approx 10^4\ \Omega^{-1}cm^{-1}$, [87]).

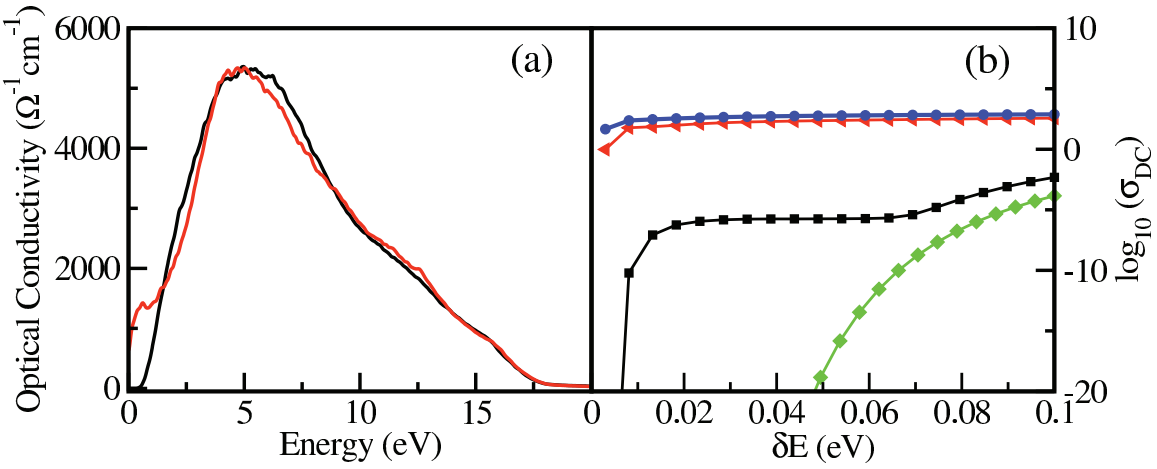

Figure 3.4: (a) Optical conductivity of insulating (black curve) and metallized (red curve) models for $(GeSe_3)_{0.75}Ag_{0.25}$ model computed using Kubo-Greenwood formula. Brillouin zone sampling is done over 4 k-points and averaged over 3 directions to eliminate artificial anisotropy. (b) DC conductivity as a function of Gaussian approximant δE (see text). black squares: insulating model at x=015, red triangles: metallic model at x=0.15, green diamonds: insulating model at x=0.25, blue circles: metallic model at x=0.25

3.3.2 Structure of Conducting Phase

We track the atomic rearrangements associated with the metallization of the network to identify the microscopic origin of metallicity. Recalling that these are inhomogenous glasses with phase separation into Ag-rich a-Ag_2Se phase and residual Ge-Se backbone, we note that the insulator-metal transition in these glasses can be viewed in terms of relative ratio of these two competing phases. In particular, we make the following three

observations associated with the insulator-metal transition: i) Growth of Ag-Se phase, ii) Depletion of tetrahedral $GeSe_2$ phase, and iii) Growth of Ge-rich phase in the host network. Below we briefly comment on these three observations, a more detailed account of structural rearrangements will be published later.

Growth of Ag-Se phase. We observe that the Ag-Se phase grows upon metallization. Se-Ag correlation (r_{Ag-Se} = 2.67 Å) is found to increase from the insulating to metallic model (see Figure 3.5, also the increase in peak P2 in Figure 3.6). For both Ag concentrations, Se-coordination around Ag is found to increase from insulating to metallic models. For x=0.15, Se-coordination around Ag increases from 3.47 to 3.72 (the later value is an average over 5 metallic models, see Figure 3.5). For x=0.25, it increases from 3.23 to (on average) 3.53.

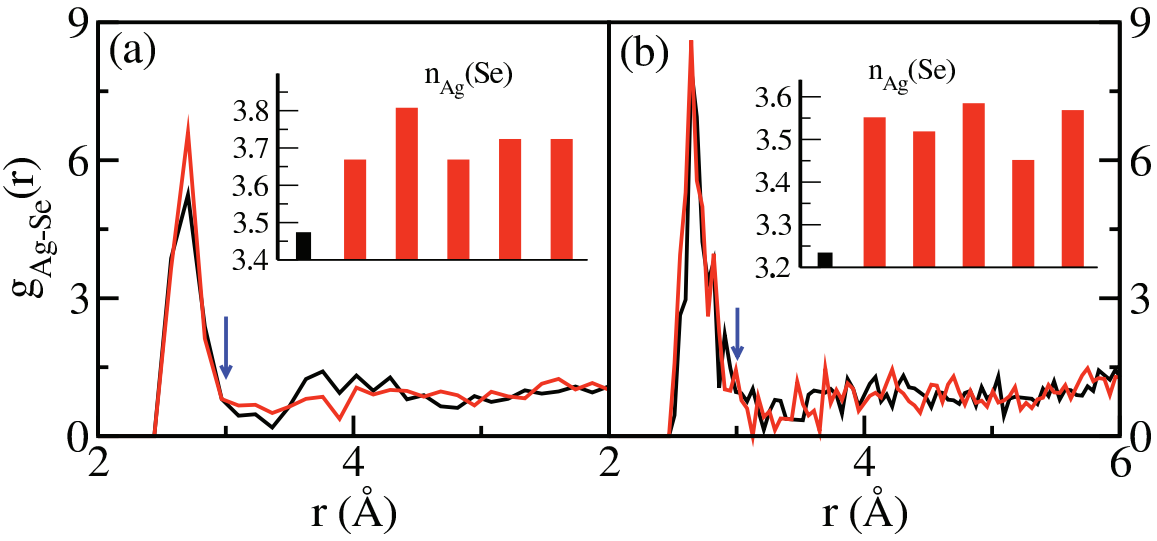

Figure 3.5: The Ag-Se correlation in insulating (black) and metallized (red) models at two concentrations of silver (a) x=0.15 and (b) x=0.25. The histogram in inset shows the Se-coordination around Ag atoms (n_{Ag}(Se)) for insulating (black) and 5 metallic (red) confirmations at both values of x. The cutoff for computing coordination is 3.00 Å, highlighted by an arrow.

Depletion of tetrahedral $GeSe_2$. The network in the insulating phase is dominated by Se-rich tetrahedral $Ge(Se_{1/2})_4$, accompanied by a competing Ag-Se phase. The fraction of later phase is directly determined by Ag-concentration in the network. These two phases appear as two distinct peaks in total radial distribution function (RDF) (Figure 3.6 and 3.7). Upon metallization, the growth of Ag-Se shifts the balance of stoichiometries in network and the host network becomes Se deficient. At composition x=0.25 (plotted in Fig. 3.6), the network in metallic phase is dominated by the Ag-Se subnetwork (peak P2). The corresponding Ge-Se coordination number in metallic model is 3.22, slightly lower than 3.40 in insulating model. These values are 3.28 and 3.43 respectively for x=0.15. The correlation cutoff of 2.70 Å is taken to determine the coordinations.

Growth of Ge-rich phase in the host network. The host network of Ge-Se consists of Se-rich tetrahedral $GeSe_2$ and non-tetrahedral Ge-rich phases including the ethane-like Ge_2Se_3 units. These subnetworks were reported in $GeSe_2$ by Boolchand and coworkers [88] and in ternary chalcogenide glasses by Mitkova and coworkers [89]. We find that these Ge-Se stoichiometries have different bondlength distributions: Se rich phases ($n_{Ge-Se} \geq 4$) have bondlengths smaller than 2.55 Å whereas Ge-rich phases ($n_{Ge-Se} < 4$) have bondlengths longer than 2.55 Å. In an insulating conformation, the former phase dominates and registers an RDF peak at $\approx$ 2.40 Å (Fig. 6.6). For metallic conformations, fewer Se atoms are available to Ge. This increases the fraction of Ge-rich phases and the Ge-Se bondlength distribution shifts to longer distances. This is represented by a shift in Ge-Se pair correlation function in Figure 3.6 (inset) and appearance of peak P3 in total RDF. Due to increase in fraction of $Ge_2(Se_{1/2})_6$, Ge-Ge correlation peak appears around 3.5 Å in metallic models. We note that it is such a Ge-Ge signal in Raman scattering and ^{119}Sn M*ö*ssbauer spectroscopy that led to experimental discovery of Ge-rich $Ge_2(Se_{1/2})_6$ phase in stoichiometric bulk Ge_xSe_{100-x} glasses [88].

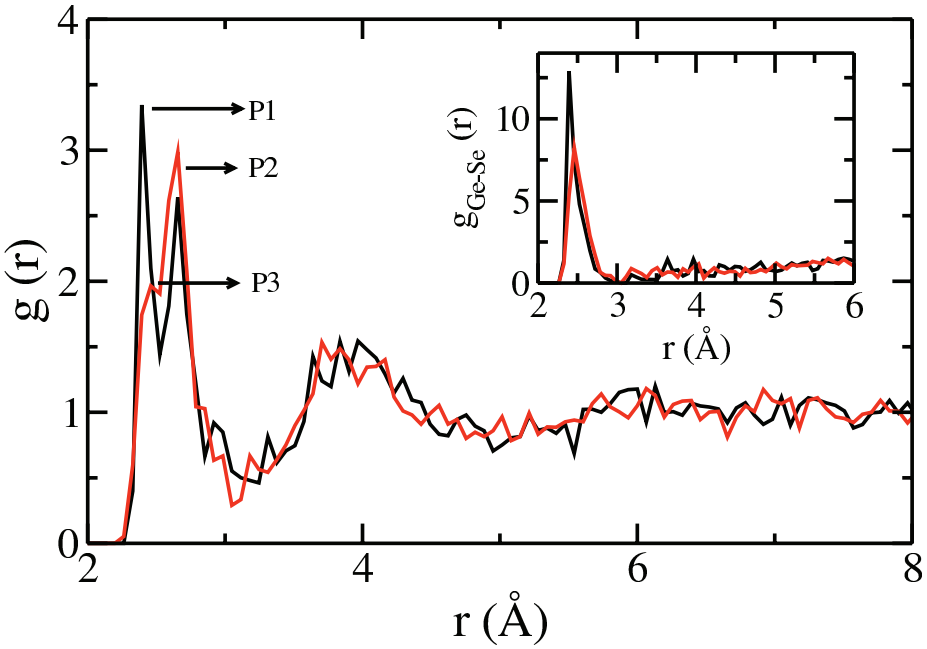

Figure 3.6: The total radial distribution function [g(r)] of the insulating and metallized models (black and red curves respectively) at x=0.25. Note the bifurcated first peak originates from Ge-Se correlation (P1 at 2.40 Å) and Ag-Se correlation (P2 at 2.67 Å). For metallized model, peak P3 arises due to depletion of tetrahedral $Ge(Se_{1/2})_4$ and formation of Ge-rich Ge-Se phases.

3.3.3 Electronic Activity of Ag-Se Phase

Now we comment further on the role of the Ag-Se phase in conduction. It is well known that the states around the Fermi energy are mainly Se p-orbitals ([90, 91], In GeSAg: [92]). The electronic structure of metallic model projected onto its constituent subnetworks (Ag-Se and Ge-Se) shows different electronic activity of Se-atoms in the two subnetworks. We find that Se atoms in Ag_2Se network have twice as much projection around the Fermi energy than the Se atoms in Ge-Se network (Figure 3.8). This suggests that a more concentrated Ag-Se network will enhance the conduction. Experimentally, growth of Ag-rich nanocrystals in GeS_2 matrix has been shown to enhance the *electronic* conductivity [93, 94]. The Se-atoms in Ag-Se phase are found in atomic state ($q_{Se} \sim 0$)

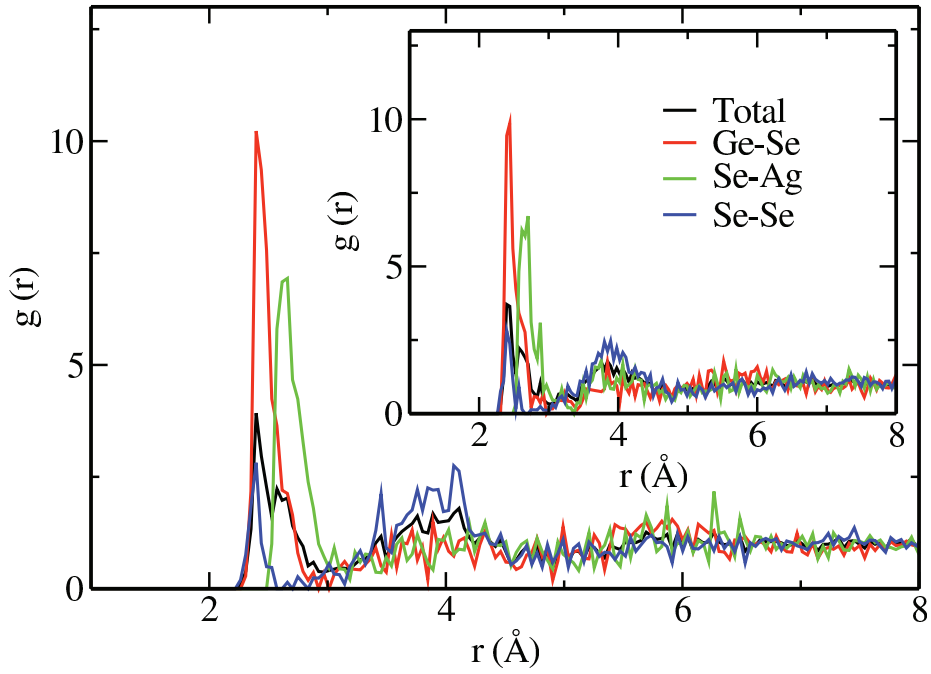

Figure 3.7: The partial pair correlation functions of the metallized models at x=0.15. Inset presents these correlation functions for insulating models. The remaining Ge-Ge, Ag-Ag and Ge-Ag correlations are noisy and are not presented here.

where as those in Ge-Se network are ionic with negative charge ($q_{Se} \sim -1$ or -2) (See inset in Figure 3.8).

3.4 Discussion

In the more general context of oxides and chalcogenides, the states in the energy gap are associated with oxygen or chalcogen p-states. An insulator-metal transition thus involves phase separation of material into an oxygen or chalcogen rich phase embedded in oxygen or chalcogen deficit matrix. Such a process has been experimentally and theoretically demonstrated in amorphous gallium oxide [95] wherein a transition to a metallic phase is shown to involve formation of O-rich Ga_2O_3 nano-crystals accompanied by O-depleted Ga-O matrix. In the case of GeS_2:Ag_2S, it has been reported that the size of

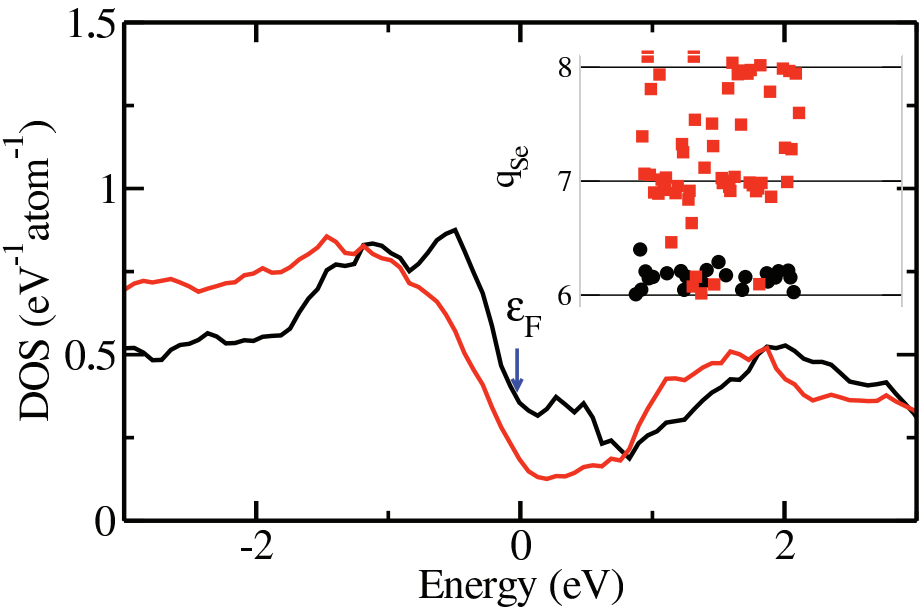

Figure 3.8: The density of states of metallic model projected onto Se-atoms in the two subnetworks: Ag-Se subnetwork (black curve) and Ge-Se subnetwork (red curve). Since these two subnetworks contain different number of Se atoms (23 and 59 for this plot), an average was taken to enable comparison. Bridging Se-atoms are not included in the calculation. The energy axis was shifted to have Fermi energy (ϵ_F) at 0 eV. The inset shows Bader charges (q_{Se}) for the same two groups of Se atoms. Black filled circles represent Se in Ag-Se network, Red filled squares represent Se in Ge-Se network.

Ag_2S nano-crystallites in a GeS_2 matrix correlates directly with electronic conductivity of the composite sample, and for sufficiently large nano-crystallites, approaches the conductivity of Ag_2S film [93]. The formation of Ag_2S and a Ge-rich host network upon the addition Ag atoms has been observed using Raman Spectroscopy [96] and this supports our observation of formation of Ge-rich backbone upon metallization.

The observed conducting phase of $GeSe_3$:Ag does not require Ag wires as often supposed. The conductivity of our phase is still rather low, of order of 200 $\Omega^{-1}cm^{-1}$, and due to an impurity band formed at the Fermi level, associated with Se p-orbitals on certain Se-atoms bonded to Ag-atoms. The impurity bands depend on the concentration of Ag and phase separation. More discussion on the conduction through impurity bands and

resonant clusters [97] is presented in chapter 4. We note here that the observed weakly conducting phases might correspond to recent observations by Chen and coworkers [98] of intermediate-phase switching in $GeSe_2$:Ag. Such intermediate conducting phase is induced by applying a weak electrochemical bias and is observed before the onset of Ag-nanowire formation.

The metallic and insulating phases reported here are an unusual example of poly-amorphism. It is interesting to observe that amorphous phases that are energetically similar can exhibit markedly different transport behavior.

3.5 Conclusions

Altogether, we have presented a direct simulation of conducting phase of CBRAM material $GeSe_3Ag$ and it provides evidence of the conduction through interconnected regions of Ag_2Se phase in the glassy matrix [93, 94]. This chapter does not attempt to describe the conduction through Ag-nanowires which may be the mechanism of conduction in two terminal metal-electrolyte-metal devices [99]. It demonstrates the existence of metastable amorphous forms ("poly-amorphism") of the glass with drastically different optical response. The observation that the DFT energies of these states are only 0.04 eV/atom higher than insulating state suggests that these states might to accessible. We also showed by direct computation that our gap sculpting method can be an effective tool to explore/discover phases of matter with desired optical properties.

4 Indirect Role of Silver Atoms in Electronic Transport in $GeSe_3Ag$ Glass

The work presented in this chapter being prepared for publication: **Prasai, K., Chen, G., Biswas, P., and Drabold, D. A. Indirect role of silver atoms in electronic transport in $GeSe_3Ag$ glass.** *In preparation.*

4.1 Introduction

Electron transport in disordered semi-conductors is intricately connected with the degree of spatial localization of electron states and various regimes of transport come into play at various manifestations of disorder [100, 101, 5]. For solids of technological use, this critically dictates the choice of stoichiometry, doping level, dimensionality and the fabrication method as a whole. Despite the elaborate theoretical frameworks laid out for such transport, computational tools are yet to be developed to help guide experiments on real materials.

This discussion is highly relevant for chalcogenide glasses being used to develop memory applications. An example of such memory application is called the "programmable metallization cell" which is based on bias induced swift change in conductivity in these materials [94, 34, 102]. These devices are shown to operate at low voltage, provide high speed and excellent scalability and retention and yet are simple to make. Various compositions of chalcogenides doped with silver or copper are shown to be effective materials and have been built into functional devices. These glasses in their as-formed state are well known semiconductors. The observed increase in conductivity by many orders of magnitude upon the application of external bias cannot be explained by ionic conduction alone. There are indications that there exists a transient electronically

conducting phase and some studies have suggested that such phase involves conducting pathways possibly made of metal atoms.

In chapter 3, we reported on direct simulations of insulator-metal transition in $GeSe_3Ag$ glasses and showed that the transition to metallic phase is characterized by an apparent "redistribution" of Se atoms from $Ge(Se_{1/2})_4$ phase to Ag_2Se phase [43]. Unmistakably, this points to the question: what role does Ag play in conduction? Or, put differently, does the conduction proceed through Ag channels that are continuous from electrode to electrode or does Ag have more indirect role in bolstering conduction of the whole cell? From our point of view, it is important to examine these questions in order to understand the formation and function of conducting channels in memory cells. There have been many attempts in this direction and some experiments have been able to identify Ag-filaments in conducting phase [103]. In this chapter, we provide important insights into the microscopic processes behind conduction through density functional simulations. We show that Ag atoms play an indirect role in transport, i.e. through the formation of non-bridging and terminating Se atoms. By explicit calculations, we demonstrate the existence of electronically resonant clusters and discuss the idea of hopping transport as a possible mode of conduction. While the existence of Ag-nanowires in conducting phase appears to be the consensus view, we show that Ag-nanowires of 2 to 3 atomic thickness *don't conduct*. We'll follow the results by a discussion of different conduction regimes where these modes of conduction may play out.

We'll center our discussion on non-stoichiometric glass: $(GeSe_3)_{1-x}Ag_x$, for varying values of x. It is a preferred class of materials for CBRAM applications. Beyond a threshold concentration, Ag atoms are shown to be highly diffusive and take part in ionic conductivity. The system has been extensively studied, using experiments [104, 105, 106] and simulations [14, 107, 90, 92, 108]. This family of silver doped chalcogenides can be prepared either by melt-quench method or by photo-dissolution of silver into glassy host.

Selenium rich stoichiometries have been shown to be phase separated into Se-rich Se_2Ag phase and Se-deficient Ge-Se backbone [30, 88, 109, 89, 93]. This glass shares many attributes of the family of glasses called "network-former network-modifier", with Ag atoms (the cations) in Se-rich stoichiometries disrupting homogeneity of network and triggering a phase separation into $GeSe_2$ and Ag_2Se. This leads to another interesting angle to view this class of material i.e. as mixture of two extremes: $GeSe_2$ (strongly glass forming network glass) and Ag_2Se (a fast ion conductor, Ag being the fast ion). The distribution of Ag atoms within or relative to the network is a highly important and widely researched topic [109, 107].

4.2 Methods

Here, we study $(GeSe_3)_{100-x}Ag_x$ at 4 different concentrations of Ag, viz., x=10%, 15%, 25% and 35%. For each of these concentrations, we take a supercell containing 240 atoms. The volumes of the supercells are chosen such that their densities matches with the experimentally measured values. We find that these glasses have been experimentally studied for x= 10, 15, and 25. The experimental densities (shown in Table 4.2) are taken from [81, 110]. For higher concentrations of Ag (*i.e* x= 35), we use extrapolated density. We get a more accurate density by performing relaxation at zero pressure during the simulation. Table 4.2 presents the details of the systems used in the simulation.

Table 4.1: System Stoichiometries and Densities

x	**Mol. Formula**	$\mathbf{N_{Ge}}$,$\mathbf{N_{Se}}$,$\mathbf{N_{Ag}}$	ρ**(gm/cm^3)**
10	$(GeSe_3)_{0.90}Ag_{0.10}$	54, 162, 24	4.98
15	$(GeSe_3)_{0.85}Ag_{0.15}$	51, 153, 36	5.03
25	$(GeSe_3)_{0.75}Ag_{0.25}$	45, 135, 60	5.31
35	$(GeSe_3)_{0.65}Ag_{0.35}$	39, 117, 84	5.52

Total energies and forces we calculated using density functional theory (DFT) [19]. Plane waves of up to 350 eV were used as basis functions and PAW potentials [24, 25] with gradient corrections due to Perdew-Burke-Ernzerhof [27] was used. The simulation was carried out using Vienna Ab-Initio Simulation Package (VASP) [22, 23]. For systems as big as 240 atoms, the energy landscape can be very complex and AIMD simulation starting from a random structure may take very long time to reach a stable energy minima. So, before starting AIMD, we performed complete melt-quench-relax cycle for each of these configurations using the two-body classical potential of Vashishta et al [14]. The resulting structures from these calculations were used as starting configuration for AIMD.

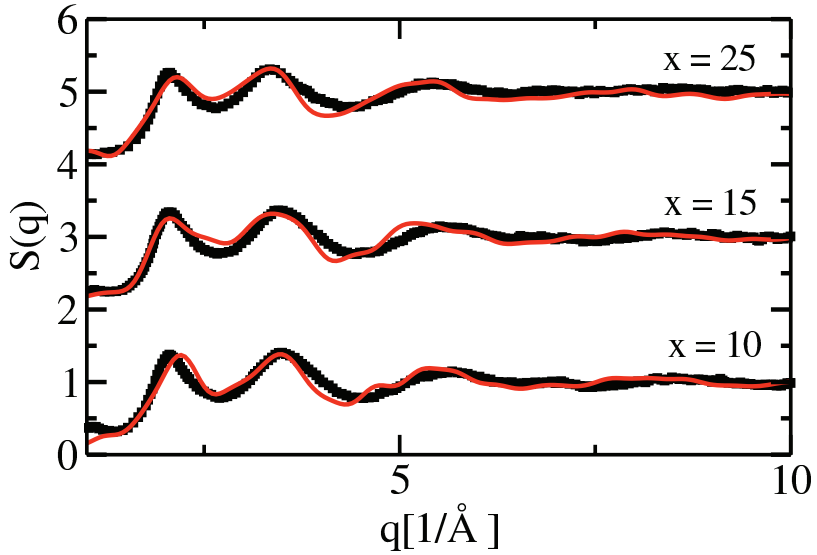

Figure 4.1: The structure factor of $(GeSe_3)_{100-x}Ag_x$ models (solid red line) compared with experiment (black squares) [81]. For the sake of clarity, vertical axis is shifted by 2 for x=15 and by 4 for x=25.

The starting configurations were equilibrated at 2000 K for 4 ps and then were cooled to 1200 K over 12 ps. Then, the models were equilibrated at 1200 K for 6 ps. These models were quenched to 300 K over 18 ps. Then, all systems were equilibrated at 300 K for 10 ps. Finally, the models are relaxed to their nearest energy minima using conjugate

gradient algorithm. The resulting models closely reproduce the structural features (e.g. structure factor, Figure 4.1) that are reported in the literature for these widely studied materials.

4.3 Results

4.3.1 Spatially Resolved Conductivity

In one of its form, the Kubo Greenwood formula (KGF) [111, 79] for electronic conductivity is written as:

$$\sigma_k(\omega) = \frac{2\pi e^2\hbar^2}{3m^2\omega\Omega}\sum_{j=1}^{N}\sum_{i=1}^{N}\sum_{\alpha=1}^{3}[F(\epsilon_i,k) - F(\epsilon_j,k)] \\ |\langle\psi_{j,k}|\bigtriangledown_\alpha|\psi_{i,k}\rangle|^2\delta(\epsilon_{j,k} - \epsilon_{i,k} - \hbar\omega) \tag{4.1}$$

We'll show elsewhere how to produce a real space decomposition of the conductivity [112]. Here, we take an empirical approach and approximate the spatial dependance by substituting the matrix elements by the product $q_i(\vec{r}) \times q_j(\vec{r})$ where $q_i(\vec{r})$ $(= |\psi_i(\vec{r})|^2)$ represents the charge density corresponding to i^{th} electronic state at position $\vec{r}$. Such an expression clearly would *not* be the *quantitative* measure of the conductivity but would rather estimate the likelihood of a point in space to take part in electron transport. This is because the charge densities (complex squares of electron wave functions) directly represent the spatial spread of the wave functions and the product of charge densities from two electron states evaluate to higher values at points in space where the overlap of those states is higher. The product is then modulated by electron distribution function and the delta function to eliminate the overlaps that do not contribute to the conduction at a given frequency. Taking only Γ point (k=0), we compute,

$$\xi_\omega(\vec{r}) = \frac{2\pi e^2\hbar^2}{m^2\omega\Omega}\sum_{j=1}^{N}\sum_{i=1}^{N}[F(\epsilon_i) - F(\epsilon_j)] \\ q_i(\vec{r})q_j(\vec{r})\delta(\epsilon_j - \epsilon_i - \hbar\omega) \tag{4.2}$$

For each ω, the above equation crudely highlights the "path" of electron transport. If $\xi_\omega(\vec{r})$ is projected onto the atomic sites, those parts of the network would get maximum projection (would "light up") that contribute most significantly to the conduction at that frequency. Figure 4.2 shows the transport active parts of the network for DC limit at Ag-concentrations 10%, 15%, 25% and 35%.

The results indicate that the Se-atoms play the most active role in electron transport. It is also interesting to observe that the transport active parts of the network form a cluster and, at higher Ag concentrations, there seems to exist a transport channel that extends through the entire length of the supercell.

4.3.2 Broken Chemical Order in Host Network

The network structure in the (network former)-(network modifier) family of glasses is often described in terms of phase separated metal chalcogenide (or metal oxide) embedded in host-network with higher glass forming tendency. In the case of Ge/Se/Ag glasses, this manifests as phase separated Ag_2Se in the glassy matrix of Ge_tSe_{1-t} where the value of t depends on composition and is discussed here.

For homogenous continuous random network glass $GeSe_2$, Ge is tetrahedrally coordinated and $t = 1/3$. In a constrained glass network, there are local fluctuations in Ge-environment. Boolchand and co-workers, through Raman and Massabauer spectroscopy, showed that glassy $GeSe_2$ shows intrinsic inhomogeneity by phase separating into $GeSe_2$ and Ge_2Se_3 networks [88]. Such inhomogeneity is also found in the host network of ternary GeSeAg glasses [96, 89] and is highly dependent on

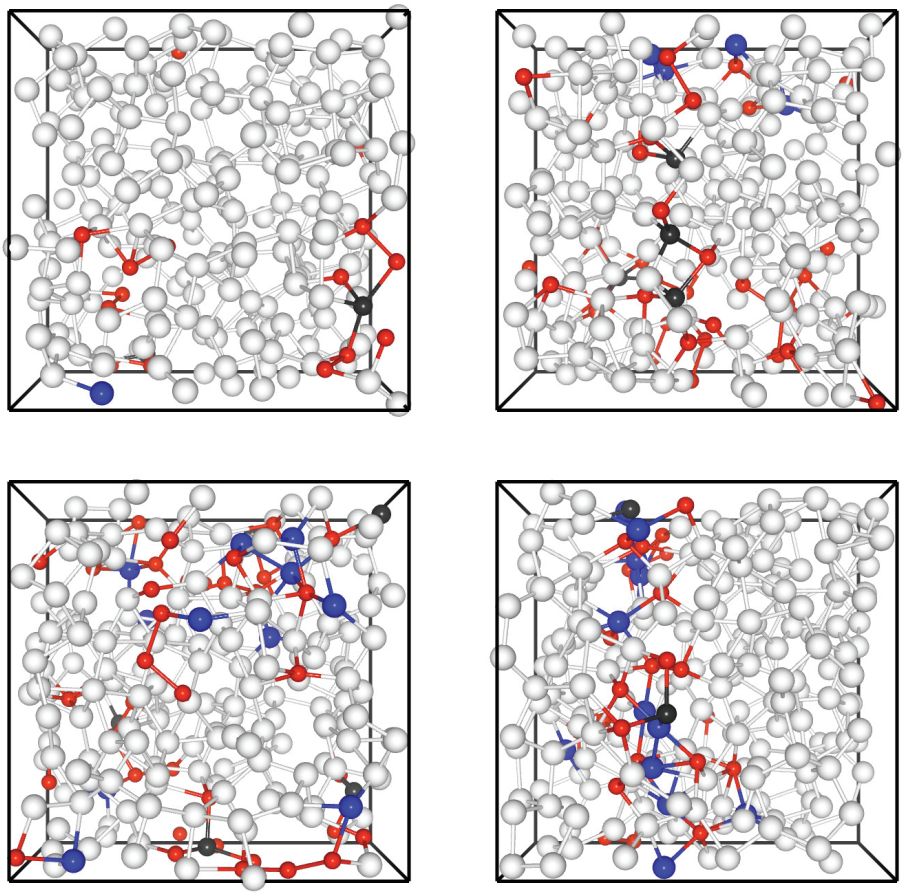

Figure 4.2: The transport active parts of $GeSe_3$:Ag models for Ag-concentrations of 10%, 15%, 25% and 35% at the DC limit at 700 K. Equation 4.2 is used to compute space projected conductivity which is then projected on the atomic sites. Color nomenclature: Red Se atoms, Blue Ag atoms and Black Ge atoms.

Ag-concentration. We recently reported that metallized $GeSe_3$:Ag models show higher fraction of Ge-rich phases [43].

We report here that such broken order in the host network has correlated bond-length and Bader-charge distribution. It is observed that the Ge-Se bonds associated with tetrahedral Ge sites tend to be short and those associated with Se-deficit Ge sites tend to be longer. Figure 4.3 shows the correlation between Ge-Se bond lengths and the

Bader-charge on the associated Ge-atoms. The Bader charge on Ge-atoms roughly correlates with Se-deficiency around them. This is true both from valence-charge arguments as well as from our nearest neighbor analysis.

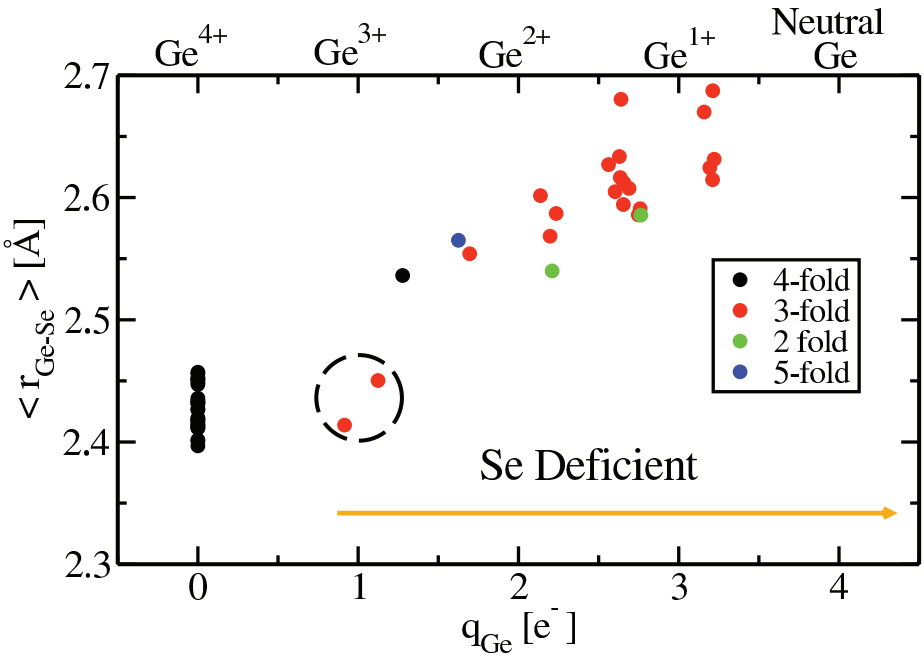

Figure 4.3: The correlation between Ge-Se bond lengths and Bader charge on associated Ge-atoms. Average Ge-Se bond length around each Ge atom is taken. A bond cutoff of 2.8 Å is taken to define the Ge-Se bonds. The broken circle encloses Ge atoms forming ethane-line Ge_2Se_3.

We note here the following considerations. Although average bond lengths are reported in figure 4.3, there is remarkable uniformity in bond lengths around each Ge-atoms. The plot suggests that Se-coordination around a Ge-atom alone may not fully characterize the Se-environment around those Ge-atoms and that the associated bond-lengths may be more relevant.

4.3.3 Electrical Activity of Se Atoms

We observe that Se-atoms play significant role in transport behavior of these glasses. First, we observe that the states in the band edges are derived mainly from Selenium p-orbitals as shown from the projected density of states (Figure 4.4).

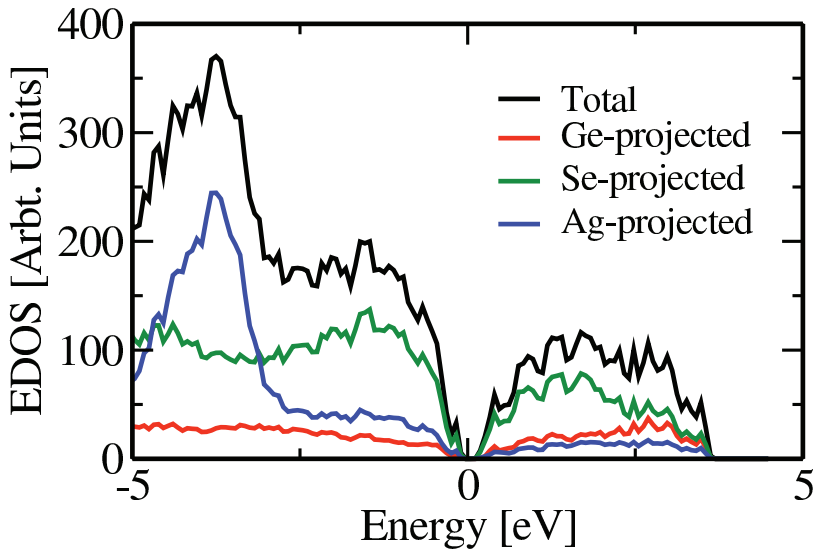

Figure 4.4: The projected electronic density of states for $(GeSe_3)_{1-x}$:Ag_x with x=0.15. The energy axis has its zero at the Fermi energy.

Se atoms exhibit wide range of bonding abilities, bonding with Ge to form host network, bonding with Ag atoms to form Ag_2Se phase and bonding with other excess Se atoms to form Se-filaments. These bonding environments project different electronic activity around the Fermi energy. To discuss this in familiar terms, we use the terminology commonly used to describe oxygen atoms in common network-former/network-modifier glasses (e.g. $NaSiO_3$). We categorize Se-atoms bonded to 2 Ge atoms as 'bridging' Se atoms. Similarly, Se-atoms bonded to one or no Ge-atom are referred here as

'non-bridging' Se-atoms. The later group of Se-atoms either 'terminates' the GeSe network (one-fold Se) or is more or less mobile and form Ag_2Se phase/short Se-chains. With this classification in mind, it is interesting to observe that the non-bridging Se atoms are highly electronically active around Fermi-energy and are transport significant. We make this point in figure 4.5 where we show the top projections of eight band-edge states on to the atoms. It is clear that the non-bridging Se-atoms play a key role band edges.

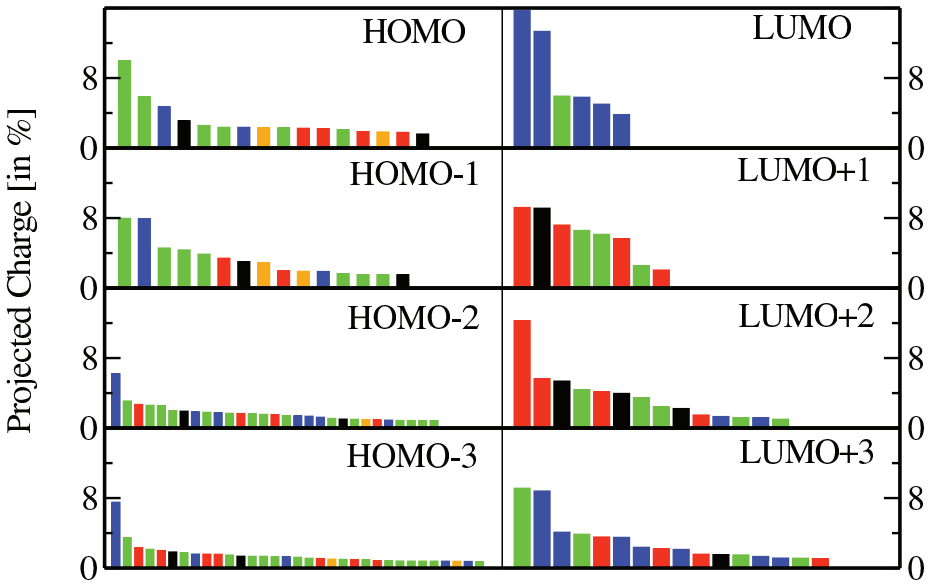

Figure 4.5: The projected charges of band edge states onto the atoms. Eight bands in the band-gap region are presented here. HOMO and LUMO represent the valence edge and conduction edge respectively. Each rectangle in the histogram represents an atomic site where the color is used to denote atom environments: Bridging Se-atoms (Red), Non-bridging Se-atoms (Green and Blue, Green for Se atoms bonded with one Ge-atom and Blue for Se-atoms not bonded to any Ge atom). Black and Orange colors represent Ge and Ag atoms respectively. Only the atoms with highest contribution to the band up to 50% of total charge of the band (i.e. $2e^-$) are shown.

This also aligns with the well-known observation that states deeper into the band are more extended as can be noted from the higher number of atom projections used to amass top 50% of the band charge for those states. We also note the asymmetrical localization on

the two sides of Fermi level. Conduction edge states appear to be more localized than the valence edge states. The states LUMO+1 and LUMO+2 have anomalous origins and are derived from two strained tetrahedral Ge sites.

4.3.4 Modeling of Ag-Nanowires in Glassy Host

We now comment on the role of Ag-nanowires on electronic transport by taking the approach of explicitly simulating the Ag-filaments in $GeSe_3Ag$ glass matrix using first principles simulation. We take the model with 10% Ag and employ a constrained dynamics to install a Ag-nanowire in the following way: The atoms in rectangular block of 5.06 Å× 5.06 Å× 18.60 Å were identified as Ag. The cross-section of this block is chosen in order to preserve the overall n_{Ge} to n_{Se} ratio. The final stoichiometry of the wire-matrix system is $(GeSe_3)_{0.84}Ag_{0.16}$. This model is then annealed at 700 K for 5 ps, then at 1000 K for 5 ps and finally quenched to 300 K in 4.5 ps. During the annealing and quenching cycle, the initial Ag atoms in the rectangular block are constrained to move only along the axis of block. The quenched structure is then relaxed to its nearest energy minima using unconstrained conjugate gradient moves. The final model has a continuous Ag filament across the center of the cell (figure 4.6) and the glassy backbone bonds well with the filament so that no internal surfaces are formed in the boundary between the filament and the matrix. The forces on the atoms are on the order of 10^{-2} eV/Å. The volume is kept fixed since the density difference between the systems with x=10 and x=15 is small. The internal pressure in the model is found to be 0.02 GPa which is quite acceptable value. For the sake of convenience, we label this model as 'Model A'.

For the sake of comparison, we repeat the same process starting with the model with 15% Ag and model a nanowire in rectangular block of dimension 7.00 Å× 7.00 Å× 18.65 Å. The final stoichiometry of the wire-matrix system for this system is $(GeSe_3)_{0.74}Ag_{0.26}$. In the discussion that follows, we call this model 'Model B' (see figure 4.6).

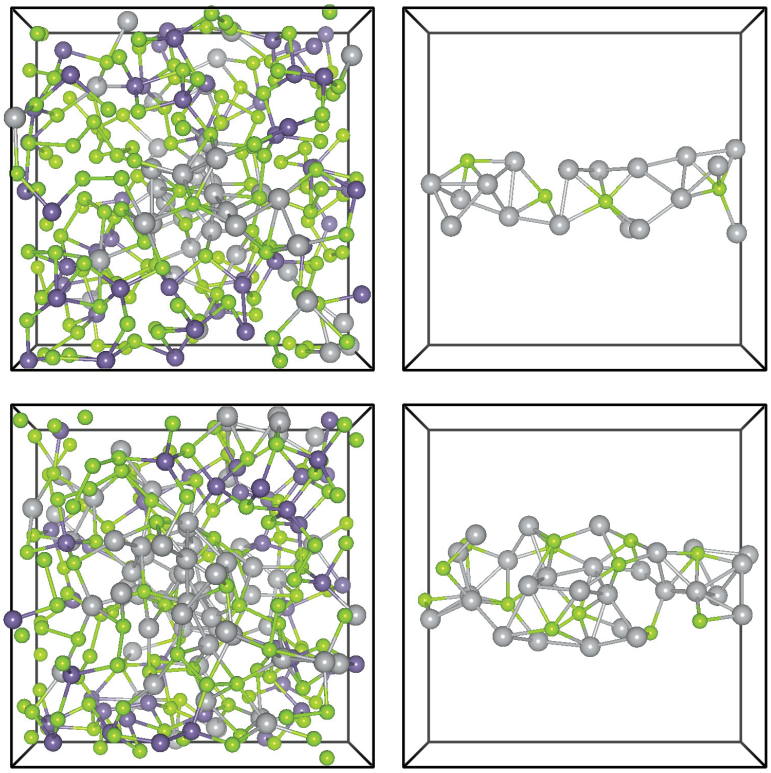

Figure 4.6: (Top left) Model A with Ag-filament viewed parallel to the axis of the filament. (Top right) The central Ag filament in the model A. (Bottom left) Model B with Ag-filament viewed parallel to the axis of the filament. (Bottom right) The central Ag filament in the model B. Color nomenclature: Ge:Purple, Se: Green, Ag: Silver

We compute the electronic structure of the systems by sampling over 4 points on the Brillouin zone. As expected, there is negligible K-dispersion since the size of the unit cell is fairly large. Figure 4.7 and 4.8 show band structures of model A and model B alongside homogenous models of comparable composition. Interestingly, we observe that Ag-nanowire does *not* produce a metal-like DOS but rather all models show a well defined band gap. We find that model A is slightly p-doped. The HOMO-LUMO gap in the model with Ag-filament is 0.04 eV. The optical gap is 0.29 eV which is still smaller compared to 0.38 eV of model without the Ag-filament. For model B, the HOMO-LUMO gap is 0.43 eV which is smaller compared to 0.53 eV of the model without the Ag-filament. These

gaps are calculated using GGA functional of Perdew-Burke-Ernzerhof [27] which are commonly known for underestimating the gap.

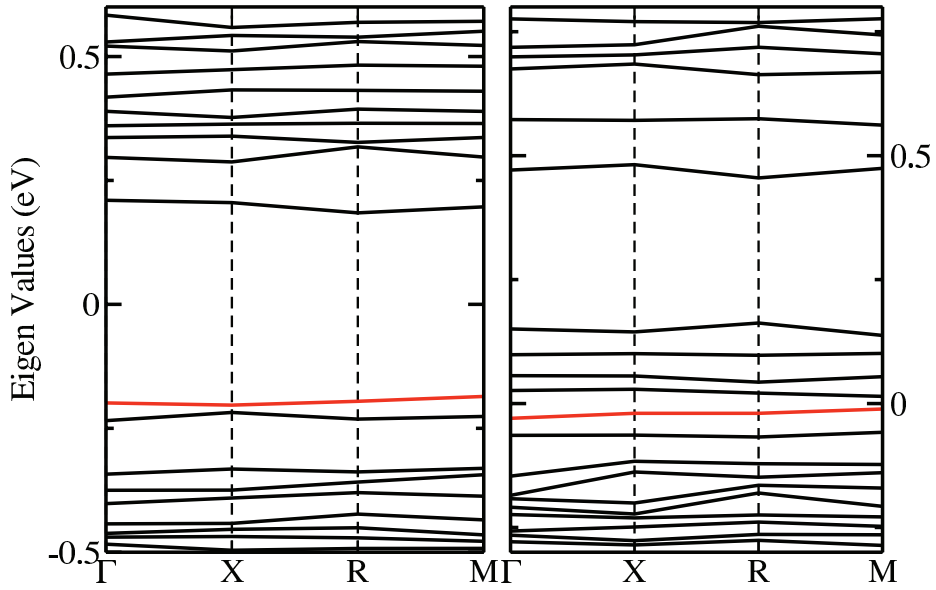

Figure 4.7: The band structure of model A (right) compared with homogenous model with close stoichiometry (left). The band structure on the left is of a homogenous model with composition $(GeSe_3)_{0.85}Ag_{0.15}$ and that on the right is of the model A (i.e the model with Ag nanowire and with composition $(GeSe_3)_{0.84}Ag_{0.16}$). The Fermi energy is at zero and HOMO level is highlighted by red line.

We computed the conductivity of model A using Kubo Greenwood formula (Eq. 4.1). In order to account for the discreteness of the density of states, we used Gaussian broadening ($\triangle$ E=0.05 eV) to replace the $\delta-$function. The DC conductivity is calculated to be $\approx 10^2$ Siemens/cm for model A which is large compared to that of the model without Ag-filament $\approx 10^{-6}$. We do not find anisotropy along different directions (α's in Eq. 4.1).

Bader charge analysis for the Ag-filament model A finds the Ag atoms in the filament in slightly positively charged state, similar to the Ag-atoms in the glass backbone (see figure 4.9). Se atoms have various negatively charged to neutral states where as Ge atoms are found in various positively charged state from Ge^{+1} to Ge^{+4}.

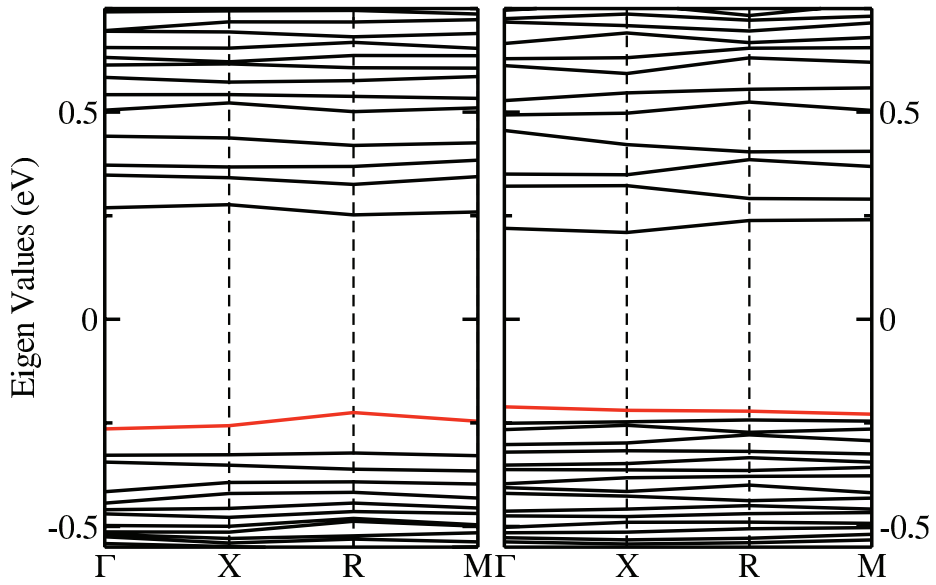

Figure 4.8: The band structure of model B (right) compared with homogenous model with close stoichiometry (left). The band structure on the left is of a homogenous model with composition $(GeSe_3)_{0.75}Ag_{0.25}$ and that on the right is of the model B (i.e the model with Ag nanowire and with composition $(GeSe_3)_{0.74}Ag_{0.26}$). The Fermi energy is at zero and HOMO level is highlighted by red line.

We probe the localization of the Kohn-Sham states in model A by computing inverse participation ratio (IPR). IPR is defined as $\sum_i a_i^4/(\sum_i a_i^2)^2$ where a_i are projections of eigenvectors onto atomic orbitals, as measure of localization of states. We find band edge states to be localized (see figure 4.10).

4.3.5 Impurity Bands and Resonant Clusters

In order to understand the role the impurity states in model A might play in the transport, we investigate the structural origins of these states. We observe that the energetically close (nearly degenerate) doping levels in model A come from the same parts in the network (See figure 4.11). This suggests that there is mixing between the doping levels and these levels form an extended band. In such a system should enable electronic conduction since an electron is more likely to find an overlapping state with

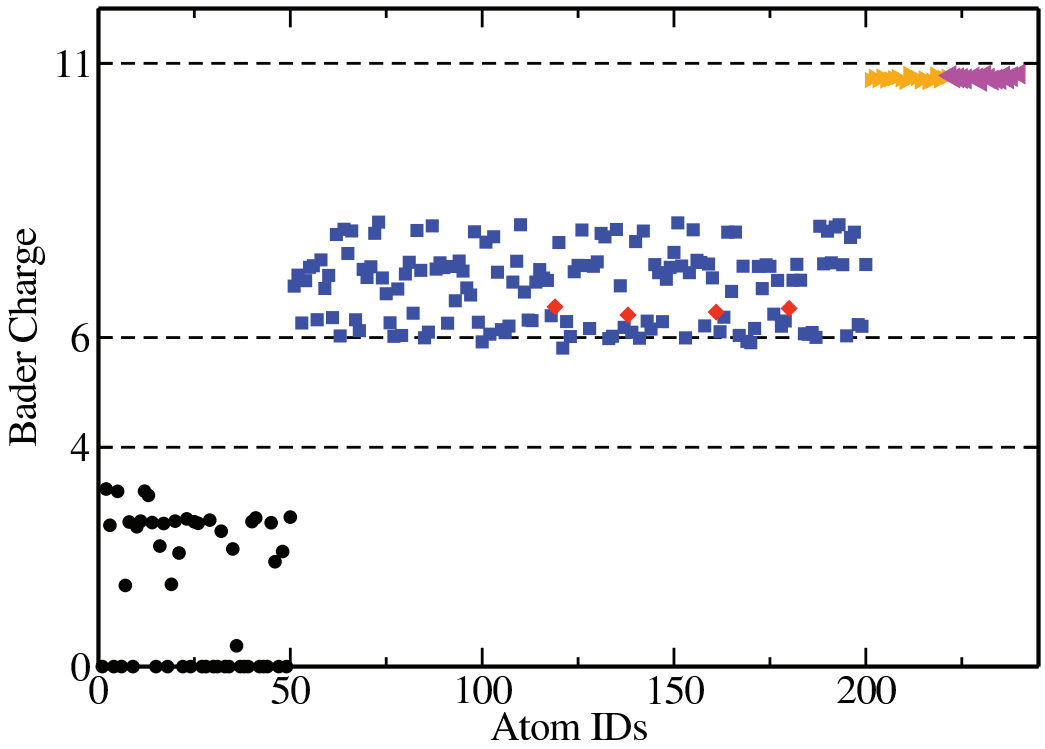

Figure 4.9: Bader charge distribution for the model A. Black circles: Ge, Blue squares: Se atoms in glass matrix, Red diamonds: Se atoms in the filament block, Orange triangles: Ag atoms in glass matrix, Pink triangles: Ag atoms in filament

similar energy. The likely mechanism of conduction from this line of reasoning is the hopping transport through the resonant clusters, discussed in more detail elsewhere [97].

4.4 Conclusions

We discussed that electronic conduction in $GeSe_3Ag$ glass proceeds through Se-Ag network and not directly through Ag atoms as is usually assumed. By explicitly modeling Ag nanowires in glassy matrix, we showed that Ag filaments of 2 to 3 atom thickness do not conduct.

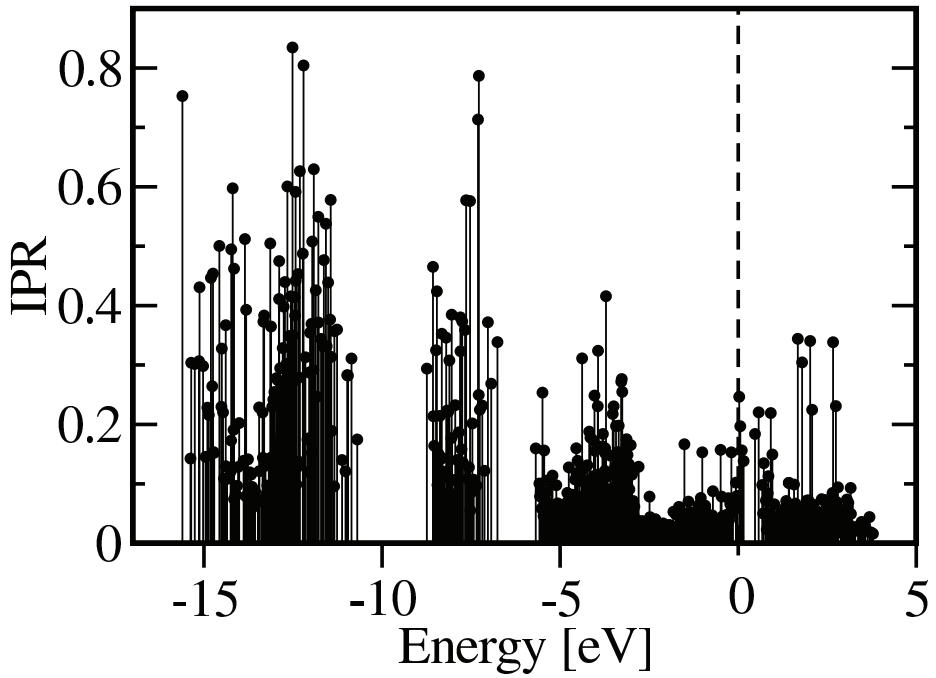

Figure 4.10: Localization of states in model A. The inverse participation ratio (IPR) of electronic states in model A is plotted against the energies of those states. The Fermi energy is at 0 eV and is indicated by broken line. Point to be noted is the degree of localization of doping levels right above the Fermi level in energy axis. These are seen to be slightly localized with IPR equal to ≈ 0.2. Note, in this formulation of IPR, 0 corresponds to homogeneously spread state and 1 corresponds to maximally localized state.

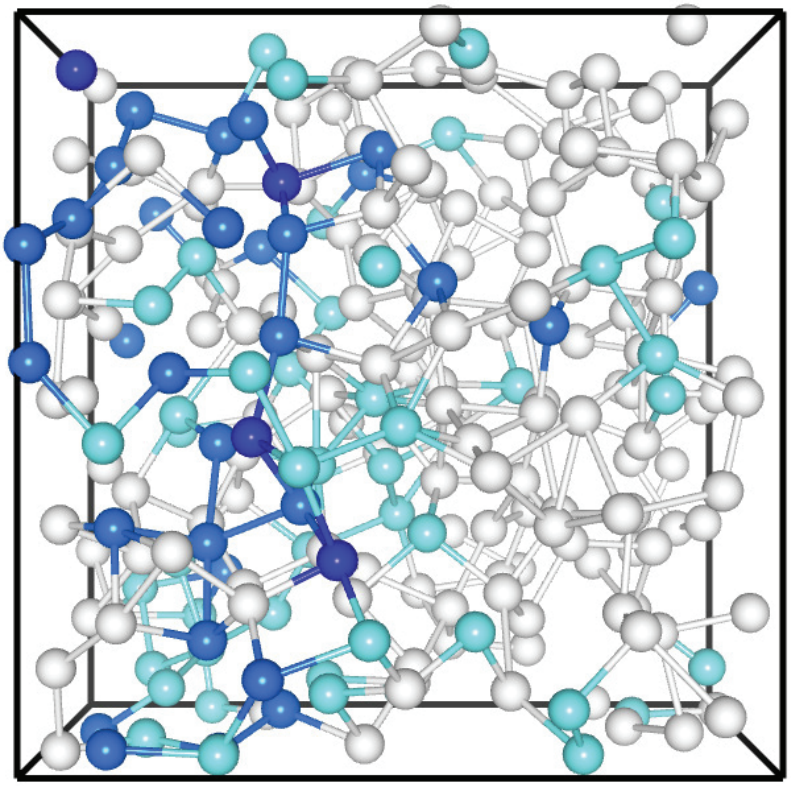

Figure 4.11: The resonant clusters in model A. The top 40 atoms (out of 240) contributing to three doping levels with energy ϵ_F+0.055 eV, ϵ_F+0.096 eV and ϵ_F+0.150 eV are presented in color. Those atoms that fall in top 40 of *all* three states (two of three states/one of three states) are painted in dark blue (light blue/ice blue).

5 Simulations of Silver-Doped Germanium-Selenide Glasses and Their Response to Radiation

The work presented in this chapter has been published in **Prasai, K. and Drabold, D. A. (2014). Simulations of silver-doped germanium-selenide glasses and their response to radiation.** Nanoscale research letters, 9(1), 594.

5.1 Introduction

Chalcogenide materials are among the most flexible and useful in current technology. Certain GeSbTe alloys are the basis of phase change memory technology [113] (now a credible alternative to conventional FLASH memory) and DVDs [114]. Amorphous Se is the active element for digital x-ray radiography [115], and metal-doped chalcogenide glasses are among the best known solid electrolytes or 'fast ion conductors'[116] and form the basis for another quite promising class of FLASH memory devices, 'conducting bridge' memory. The basic science of the material is just as interesting as the other phenomena such as the optomechanical effect [117] and photomelting [118]. Recently, a new application has emerged: the use of chalcogenide glasses for the detection or sensing of radiation (a dosimeter) [119, 120]. The electrical conductivity is found to be well-correlated to radiation dose [121]. With annealing, the damage is readily reversed so that the device may be reused. This important discovery is presently empirically understood, suggesting the need for theoretical research both to understand the basic process and to aid in optimizing the materials for future device application.

In this chapter, we undertake the first simulation to understand the atomistics of the response of chalcogenide glasses to highly energetic events. Like many other challenging material problems, we find it helpful to use multiple methods, in this case both empirical potentials, and *ab initio* techniques. We also have taken advantage of the contributions of

others, such as the use of an appropriate ‘heat bath’ to handle the excess thermal energy after the thermal spike [122]. We detail the disordering process from a knock-on event to the subsequent recovery process. We show that the spike is indeed reversible upon annealing and discuss the electron states near the Fermi level - those responsible for the changes in (electronic) conduction after radiation exposure. The picture that emerges is that the electronic transport is significantly determined by the connectivity of the Ag subnetwork. Thus, if clusters percolate through the entire system, we have a network of nanowires that provide a low resistivity. As these nanowires break, form, or otherwise change, the carrier transport changes accordingly.

5.2 Methods

5.2.1 Model Formation

Simulations have been widely used to characterize amorphous materials and satisfactory *ab initio* models of GeSeAg glasses for various compositions that have already been reported [123, 124]. Molecular dynamics (MD) simulation is a natural approach to simulate high-energy processes because MD offers detailed trajectories of the atoms as the system evolves after the radiation induced event. The pitfall of MD is that it is only as good as the force field used and it is as computationally costly as it is detailed. Furthermore, large models are needed to realistically simulate radiation events in any material and this greatly increases the computational cost.

Many simulations of radiation damage have been presented, with varying details and system sizes ranging from 446 to 2.3 million atoms; the following is a highly incomplete list [125, 126, 122, 127]. Early simulations applied many approximations like the binary collision approximation (BCA) [128], linear interactions [129, 128], and others to reduce the computational demand. Clever algorithms and parallel machines have enabled full simulations on large models [127]. We used the potential of Iyetomi et al.[14] to model

the interatomic attractions. This potential is simple in its form containing a Coulomb interaction term, charge-dipole interaction term, and a short range repulsion term, and yet commendable in its ability to predict wide range of properties of this material.

The primary model of a silver rich glass (with stoichiometry close to that used for a detector) was fabricated as follows. We used a cubic supercell containing 5,184 atoms with periodic boundary condition to represent bulk $Ge_3Se_9Ag_4$ (the cell had 984, 2,888, and 1,312 atoms of Ge, Se, and Ag, respectively). The model described in this work is obtained by using the melt-quenching method [130]. Starting from a randomly placed collection of atoms, we performed 10^5 steps of MD with constant NVE. Then the atoms were given random velocities corresponding to a macroscopic temperature of 5,000 K and were allowed to equilibrate for another 10^5 steps. The system was then cooled to 1,200 K over 3.8×10^5 steps and equilibrated at 1,200 K for another 10^5 steps. The system was then cooled to 300 K over 0.75×10^5 steps and equilibrated at 300 K for 10^5 steps. Finally, the system was relaxed using a conjugate gradient algorithm. The MD simulations described in this work were performed using the classical molecular dynamics simulation package LAMMPS [15]. A time step of 1 fs was used throughout, except when variable time steps were required.

This model faithfully reproduces many features of the material (see also reference [14]). The total radial distribution function (RDF) given by this model is in reasonable agreement with the experimental RDF [131] including a two-peak first neighbor feature in $g(r)$ (see Figure 5.1). Our model also reproduces the experimental nearest neighbor distances of Ge-Se, Se-Se, and Se-Ag correlations [131]. It overestimates the Ag-Ag correlation distance, but this can be understood considering the broad peak of Ag-Ag pair correlation function (see Figure 5.2).

The first peak of the partial RDF of Se-Ag displays a companion alongside the first peak in total RDF. The Se-Ag interatomic potential has a shallow minimum near the

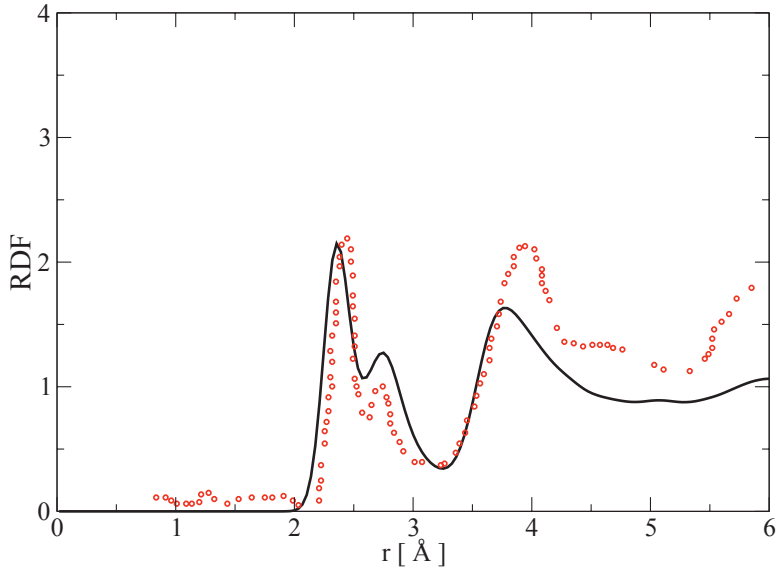

Figure 5.1: Radial distribution function (RDF): models and experiment. The total RDF of our model compared with experimental values for same composition (the red circles) from reference [131].

Se-Ag correlation distance, whereas all other interactions of Ag-atoms are repulsive. As a result, Ag atoms are very mobile in the network and Se atoms see high coordination with respect to Ag. The exceptional mobility of Ag atoms with respect to the host atoms is a widely reported phenomenon [90, 14, 132], and the basis of many applications, and even the accelerated crystallization of phase-change memory materials [133]. The mean-squared displacement (MSD) of atoms calculated for our model also predicts the high mobility of silver at all temperatures below the melting point of the material. Figure 5.3 shows the MSD for Ag atoms at different temperatures. The diffusion coefficients and conductivity calculated using the total MSD of the system compare

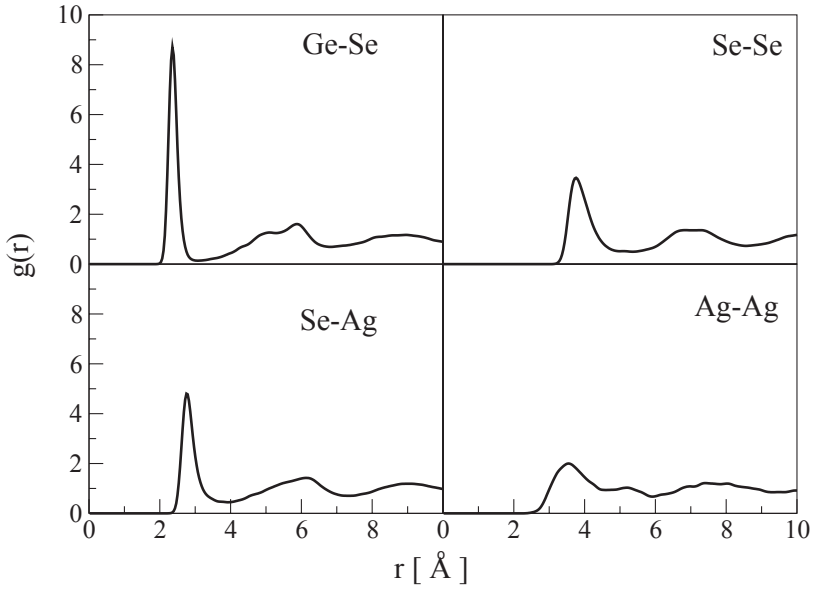

Figure 5.2: Partial correlations. The partial pair distribution function, *g(r)*, of our model. Note the weakly defined correlation of Ag-Ag interaction.

favorably with the corresponding experimental and *ab initio* values reported for most similar system as ours (see Table 5.1).

Table 5.1: Diffusion Coefficients and Ionic Conductivity

	D(cm^2/s)		**Conductivity (Siemens/cm)**		
	This work	**Ref [123]**	**This work**	**Ref [123]**	**Expt [134]**
300 K	4.05e-7	1.16e-8	0.0989	5.3e-4	7.5e-5
700 K	2.33e-6	1.20e-5	0.2436	0.235	0.0657
1,000 K	6.84e-6	2.53e-5	0.501	0.347	0.2584

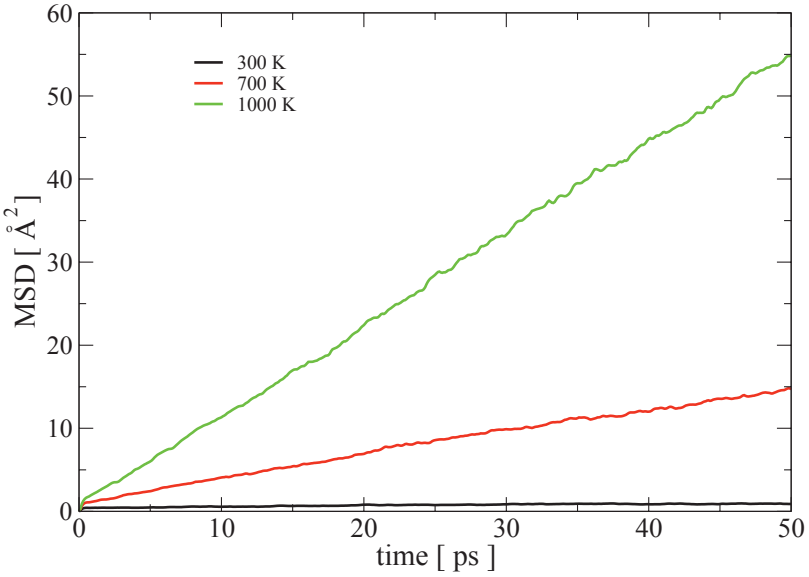

Figure 5.3: Silver dynamics and diffusion. Mean squared displacement of silver at different temperatures. The size of the simulation box is 50.86 Å.

5.2.2 Damage Simulation Using Thermal Spike

We carry out a thermal spike simulation using the model above. The damage inflicted on a material by high-energy radiation starts with a sudden transfer of kinetic energy from the incoming particle to an atom or a group of atoms that happen to suffer a collision with the incoming particle. For incident particles of energy in the range of MeV, the first interaction with the atoms on the target is entirely ballistic and the detailed role of interatomic potential between the impinging projectile and the target can be neglected. So, following Rubia et al.[126], we modeled the onset of radiation damage by igniting a thermal spike at the center of the supercell. We defined a sphere of radius 2.5 Å located at the center of the supercell, i.e., at d/2, d/2, and d/2, where *d* is the size of the cubic supercell to receive the thermal spike. For the particular configuration we modeled, this

sphere contained two atoms. These two atoms were given an initial velocity consistent with 1 MeV of energy, and the rest of the atoms were assigned a velocity distribution associated with a temperature of 300 K. These conditions are thus intended to mimic a damage event at 300 K with the center two atoms representing the primary knock-on atoms (PKAs). The system was then allowed to evolve. For an isotropic material like GeSeAg and energy of PKA being as high as MeV, the direction of the initial velocity of the PKA should have no observable effect on the damage production.

In view of the large velocity imparted to the atoms and the unknown behavior of the empirical potential under extreme conditions, we used a variable time step as in [135]. To avoid the diverging cascade of damage from bouncing back from the boundary, we used a damped outer layer of 0.5 Å thickness. The velocities of the atoms falling in this boundary region were rescaled at every dynamical step [136]. The schematic diagram of the simulation setup is shown in Figure 5.4.

5.3 Results

Immediately after the detonation of a thermal spike at the center, the hot atoms' trajectories resemble a projectile, and they pass through the network transferring huge amount of momentum to the atoms along their trajectory. These recipients of momentum get knocked from the network and, in turn, start moving like a projectile, thus creating a cascade. At this stage, the velocity of the PKA is highly non-canonical as indicated by the observation that temperature of the system excluding the PKA lags behind the temperature of the whole system for a brief period of time (see Figure 5.5). An animation tracking the positions of atoms and the average temperature of the system reveals rapid local melting. The average temperature of the system remains above the melting point of $GeSe_3Ag$ (approximately 1150 K, [131]) for 11.9 ps. To visualize radiation damage inflicted on the network, we present snapshots of a slice of the supercell containing central 6 Å of the

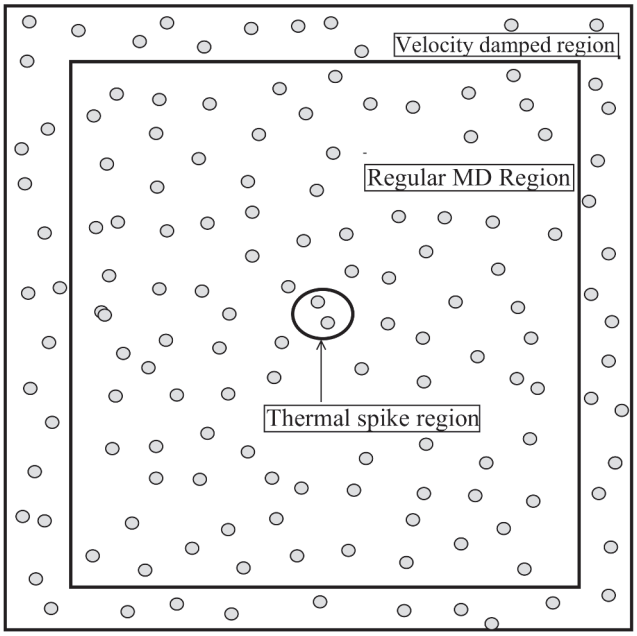

Figure 5.4: Schematics of simulation box. Diagram showing the regions of a simulation box where the thermal spike was modeled (the central circle), where the velocity rescaling was applied (the outer boundary), and where the normal molecular dynamics was performed.

simulation box at different times after the detonation (Figure 5.6). The damage is most conspicuous at 2.25 ps, and the image clearly shows the formation of voids and internal surfaces. At 10 ps, the system can be seen returning to its initial structure as also indicated by first peak of total RDF gaining height around that time.

With the onset of local melting, the system loses its short-range order. The temporal evolution of the RDF in Figure 5.7 shows an interesting recovery. The short-range order can be seen evolving continuously with the first peak gaining height and the first minimum continuously deepening. The evolution of second peak follows. The hump in the first peak originating from Se-Ag coordination, however, does not reappear as late as 50 ps.

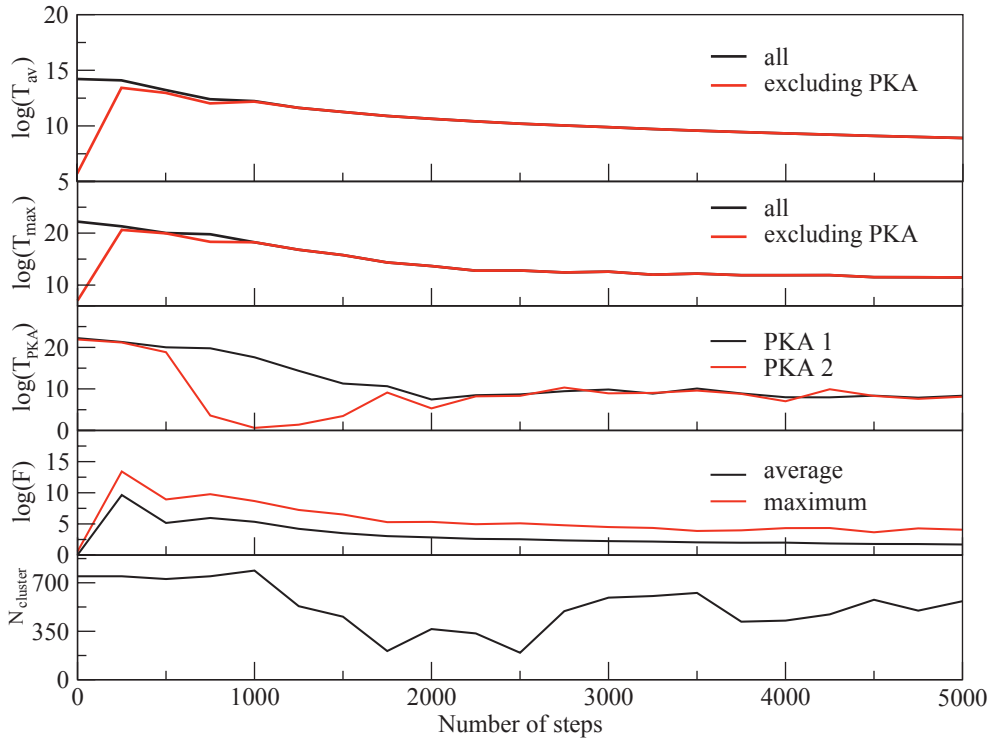

Figure 5.5: Evolution of the thermal spike. The logarithm of the average temperature (top box), logarithm of temperature of the hottest atom in the system (second box from top), logarithm of temperature of PKAs (third box from top), logarithm of force on the atoms (fourth box from top), and the size of largest cluster in the system (bottom).

To investigate the effect of radiation events on the phase separation of Ag atoms, we performed a cluster analysis of Ag atoms over the entire evolution of damage. We defined a cluster as a group of all atoms lying within a cutoff distance from at least one other atom belonging to the same cluster. We chose a cutoff distance of 3.7 Å (the Ag-Ag correlation distance is 3.55 Å) to define the cluster. Defined in this way, the initial configuration has one large cluster of about 750 atoms and other numerous smaller clusters. At just 2 ps into the damage evolution, the clustering of Ag is lost and the cluster distribution at this point

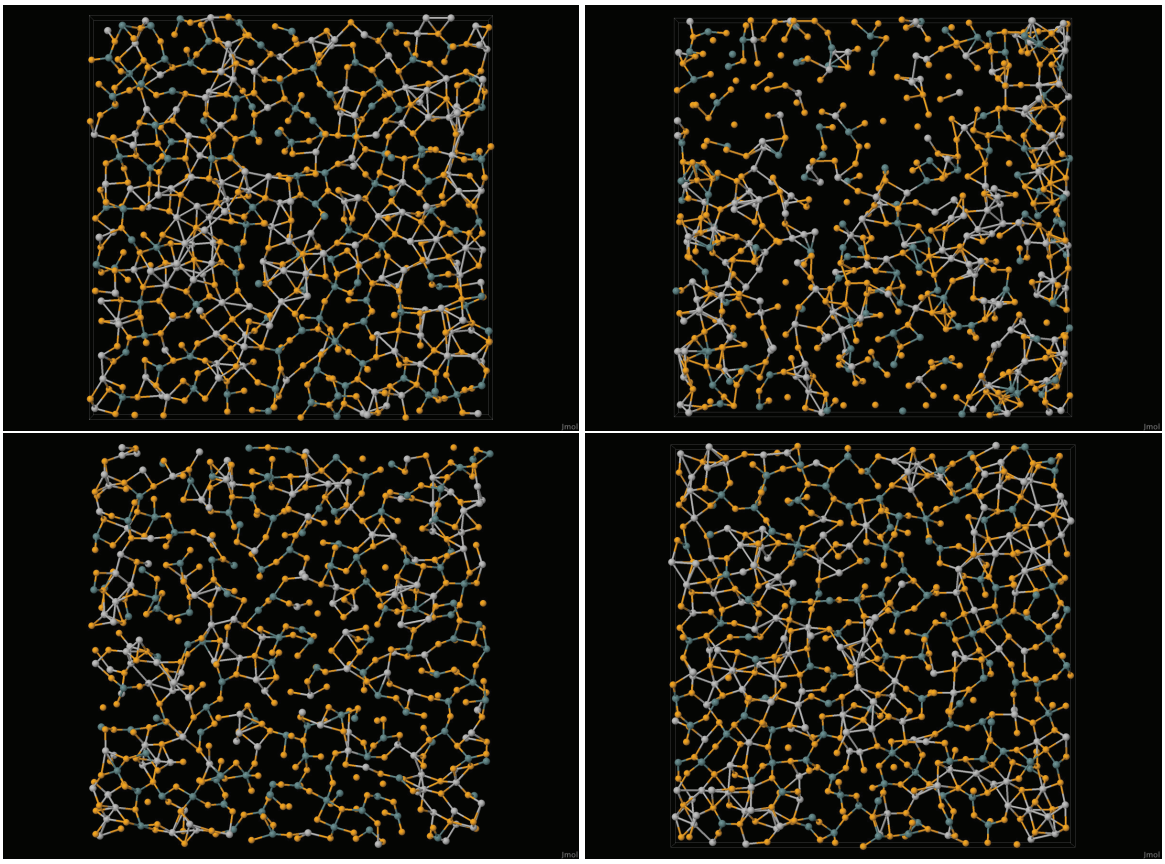

Figure 5.6: Damaged snapshots: Snapshots of central 6 of the simulation box (a) before the event, (b) at 2.25 ps after the event (c) at 10 ps after the even (d) at 50 ps after the event (fully equilibrated). The temperature drops below the melting point at around 12 ps.

essentially resembles a random configuration. The clusters, however, begin to grow as the network rearranges and recovers its initial connectivity (see Figure 5.8). The size of the biggest cluster in the network hits its minimum between 1.6 and 2.6 ps (see Figure 5.5). This is an interesting observation in that it lags behind the time the system has the highest temperature. We observe that the electrical conductivity presumably depends sensitively on the connectivity of the Ag subnetwork, the number, and the structure of the Ag filaments.

We performed *ab initio* calculation of the electronic densities of states (EDOS) of a 648-atom model prepared using the same empirical potential and the damaged snapshots

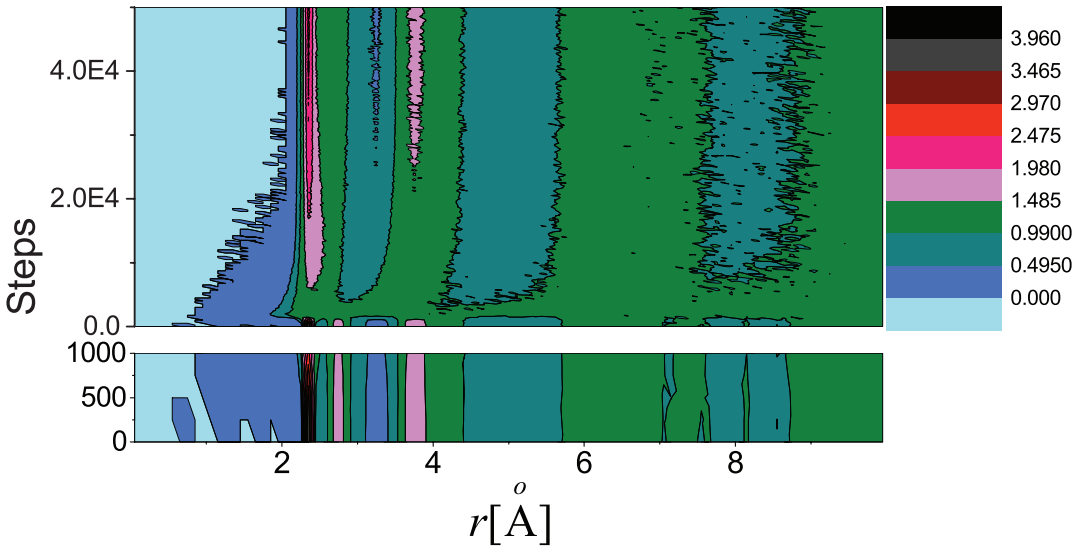

Figure 5.7: Evolution of RDF. The temporal change in total RDF of the system after the damage event. The features at the beginning are largely recovered after approximately 20,000 steps in the detonation-healing process. The RDF values for the first 1,000 steps after the detonation are highlighted in a separate band at the bottom. Note the peak values in the beginning and loss of the second peak of the first coordination.

of this model. The size of this model is a compromise between being large enough for damage production and being small enough for an *ab initio* calculation. Our calculations and reference [14] have confirmed that the 648-atom model is statistically similar to the 5184-atom model we discussed above. EDOS calculation is done using plane-wave basis code VASP [22, 23]. Plane waves of up to 350 eV and PAW potentials were used [24, 25].

EDOS and inverse participation ratio (IPR) (a measure of the spatial localization of the Kohn-Sham electronic states) of our 648-atom model is plotted in Figure 5.9. A comparison with EDOS from an *ab initio* model [123] reveals that our model lacks an energy gap though there are fewer slightly localized states in the expected gap region. Tracing the structural origin of these states, we note these are p-orbitals localized around Se atoms that are under coordinated with respect to Ge atoms (either one-fold or no Ge coordination). Our calculation on a smaller 100-atom model of [123], prepared using first

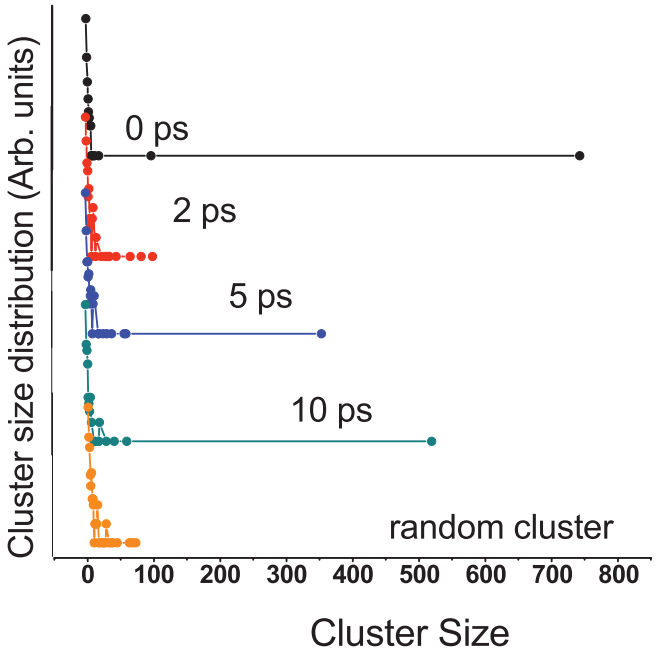

Figure 5.8: Cluster size distribution. The distribution of different sizes of Ag-clusters in system at the beginning, at 2 ps, at 5 ps, at 10 ps and in a random collection of Ag atoms. Vertical axis is in shifted logarithmic scale.

principles method, also shows that gap states are contributed by Se atoms that are under-coordinated with respect to Ge atoms.

We also analyzed the evolution of the electronic structure as the system passes through damage and restoration (see Figure 5.10). The damaged structures lead to gap states arising from under-coordinated Se atoms. It is interesting to note that the electronic structure recovers very quickly compared to the network itself. The RDF evolution of Figure 5.7 suggests that although the first peak and first minimum begin to take qualitative shape very early, the network attains similar structural order as the starting configuration as late as 25 ps. The electronic states however show a remarkable healing and reversibility even at 10 ps after the incidence of radiation. This naturally points to an interesting physics underlying the damage recovery that some features of network recover early

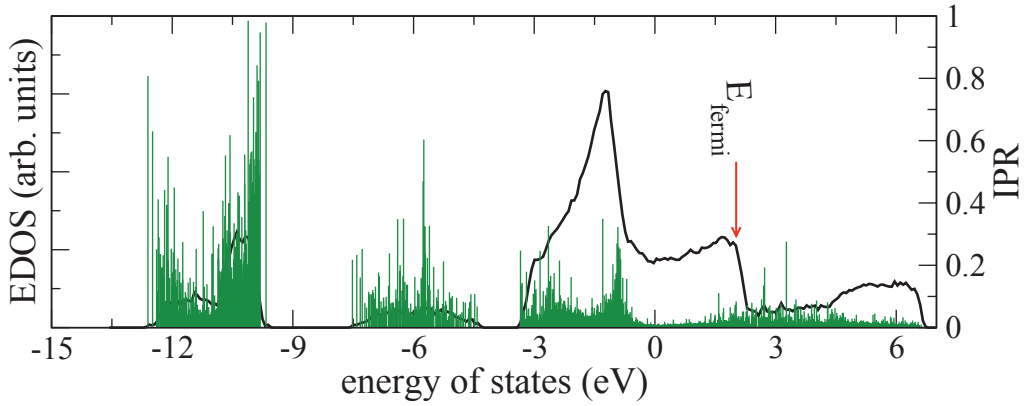

Figure 5.9: Electronic density of states (EDOS) and inverse participation ratio (IPR): The black curve shows EDOS and the green drop lines represent IPR (a measure of spatial localization of states) of 648-atom models obtained using empirical potential of reference [14]. Fermi level is at 2.01 eV.

whereas some others (eg., the Se-Ag correlation) are not recovered even after some equilibration of the system.

5.4 Conclusions

This paper is the first word on the atomistic processes underlying the fascinating experiments and device of Mitkova and coworkers [119, 121]. To fully realize the potential of our approach, many issues such as cell size, composition, details of the modeling of thermal spikes (and subsequent relaxation), and material composition must be explored. Observables like the transport and optical properties should be extracted at representative moments in the simulation. Nevertheless, this work reveals key aspects seen in the experiments including a remarkable reversibility upon annealing. We show that judicious use of the empirical potential of Iyetomi et al [14] leads to a credible model of the dynamical processes and correctly reproduces many aspects of the material. *Ab initio* methods are an important tool to augment this work and to understand its limitations

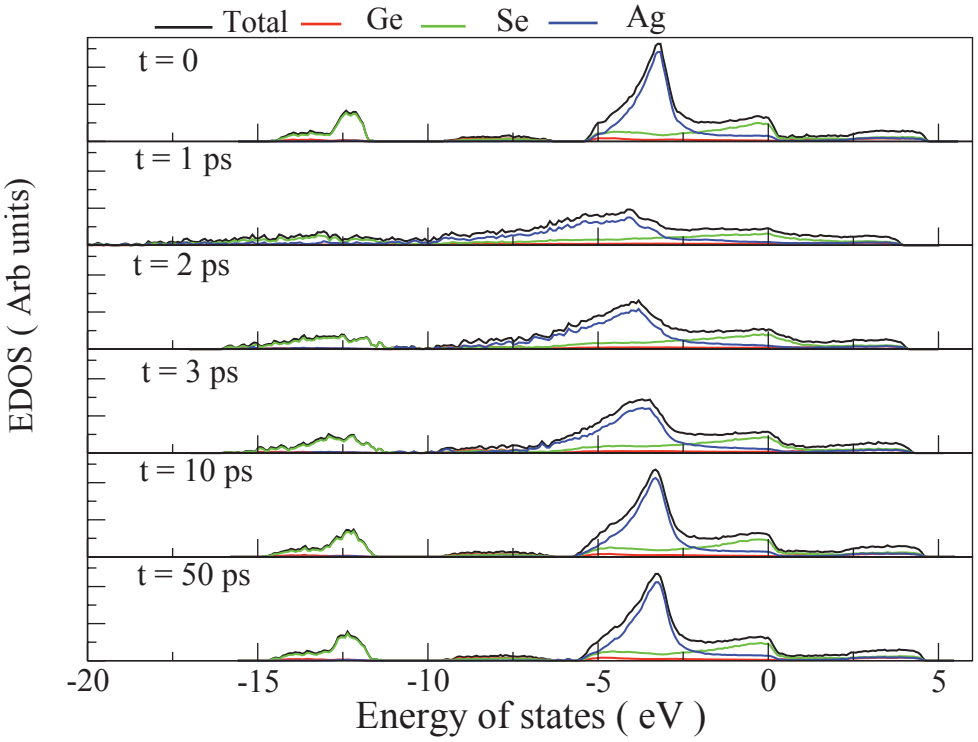

Figure 5.10: The evolution and reversibility of electronic structure. Electronic density of states of six instantaneous configurations of the model at different times with respect to damage event. The model structure and damaged structures were produced using empirical potential, and the electronic structure was calculated for these structures using first principle methods. Note the high degree of reversibility (comparing t=0 and t=50 ps).

and the electronic and optical properties. We have not yet modeled the conductivity of the system. This is complicated by the existence of both ionic and electronic conductivities for some parts of the simulation. Realistic calculations are currently being formulated (chapter 4 and reference [112]).

6 Electrons and Phonons in Amorphous Semiconductors

The work presented in this chapter has been published in **Prasai, K., Biswas, P., and Drabold, D. A. (2016). Electrons and phonons in amorphous semiconductors.** Semiconductor Science and Technology, 31(7), 73002-73015.

6.1 Introduction

Amorphous materials lack long-range structural order. For electrons and phonons in amorphous materials, the wave functions and classical normal modes may be localized, i.e. confined only to a finite volume of space. This is in contrast with any crystals, for which Bloch's Theorem applies and it is clear that *all* electron or vibrational states are extended (though of course not necessarily uniformly so). The localized states occur in spectral gaps in the electron or vibrational density of states. Any physical process that involves these localized states will be markedly different than for the extended states of translationally invariant systems.

In this chapter, we focus on one substantial issue – the interplay between the electronic properties (electronic states and energies) and the atomic coordinates (and associated motion of the atoms when in or out of thermal equilibrium). This linkage between the electronic and ionic degrees of freedom is described by the electron-phonon coupling (EPC) and plays a crucial role in determining thermal and optical responses of a solid to light and charge-carrier transport. We explore the electron-lattice coupling using current tools of first-principles computer simulation. We choose three materials to illustrate the phenomena: amorphous silicon (*a*-Si), amorphous selenium (*a*-Se) and amorphous gallium nitride (*a*-GaN). In each case, we show that there is a strong correlation between the localization of electron states and the magnitude of thermally-induced fluctuations in energy eigenvalues obtained from the density-functional theory (i.e. Kohn-Sham eigenvalues). We provide a heuristic theory to explain these

observations. Next, we explore the consequences of changing the charge state of a system as a proxy for tracking photo-induced structural changes in the materials.

6.2 Theory

The framework underlying these calculations is the many-body (electron and nucleon) Schrödinger equation. The first essential approximation is the Born-Oppenheimer or adiabatic approximation, which enables the decoupling of the electrons and phonons into separate quantum many-body problems. Still prohibitively difficult, we then make the assumption that the lattice dynamics may be treated classically. In practice, this means that the nuclei move in a potential determined by the electronic structure of the system (computed for that set of instantaneous atomic coordinates). Like others, we approach the many-electron problem using density functional theory in the local density approximation [137, 19]. Then, with specified initial conditions, we evolve the positions of the nuclei for a short time (of order 1 fs), obtaining updated coordinates and thus a new electronic Hamiltonian, with a new force field, and so the dynamics continues. Yet another approximation is to treat the Kohn-Sham orbitals as quasiparticle states, and we take the density of electron states to just be the density of Kohn-Sham eigenvalues. While these are substantial approximations, the resulting dynamics are reliable, as seen by direct comparisons to inelastic neutron scattering measurements. These are standard assumptions used in current *ab initio* molecular dynamics simulations. The simulations in this work were carried using the plane-wave code, Vienna Ab initio Simulation Package (VASP) [22, 23], in the local density approximation (LDA) [26].

Although we carry out first principles calculation for rest of the chapter, here let us consider an orthogonal tight-binding prescription for the electronic structure and the forces for the simplicity of equations. In this picture the ionic dynamics are determined by

Newton's Second Law (in the form of $3N$ coupled nonlinear ordinary differential equations):

$$m_\alpha \frac{d^2 R_\alpha}{dt^2} = -\frac{\partial \Phi(R_1, R_2, ..., R_{3N})}{\partial R_\alpha} \tag{6.1}$$

where,

$$\begin{aligned} \Phi(R_1, R_2, ..., R_{3N}) &= 2 \sum_{iocc} \lambda_i(R_1, R_2....R_{3N}) \\ &+ U(R_1, R_2....R_{3N}) \end{aligned} \tag{6.2}$$

Here, Φ is the total energy, a function of the atomic coordinates R_α, λ_i are the energy eigenvalues for the tight-binding Hamiltonian H ($H\psi_i = \lambda_i \psi$), the sum over occupied eigenvalues is the electronic contribution to the total energy (the so-called band-structure energy), and U is a short-range repulsive potential between ions. The greatest complexity emerges in Eq. 6.2, for which the computation of the energy eigenvalues λ requires a matrix diagonalization, so that the dependence of Φ on R_α may take a highly complex, and nonlocal and non-analytic functional form. Equation 6.1 represents the influence of the electrons on the particle coordinates in the form of a second-order differential equation, the second equation identifies the functional dependence of the total energy in terms of the electronic structure.

Equations 6.1 and 6.2 highlight the role of the Hellmann-Feynman derivatives,

$$\nabla_\alpha \lambda_i = \frac{\partial \lambda_i(R_1, R_2, ..., R_{3N})}{\partial R_\alpha} = \langle \psi_i | \frac{\partial H(R_1, R_2, ..., R_{3N})}{\partial R_\alpha} | \psi_i \rangle, \tag{6.3}$$

which are gradients of the electronic eigenvalues. The result is particularly useful because the RHS is easily computed and necessary for any molecular dynamics simulation based on an interatomic potential derived from electronic structure. Since they are gradients, they represent the direction of the most rapid increase of the eigenvalues in the

configuration space. These gradients have special utility for modeling of photoresponse [138] and computational gap engineering [40].

6.2.1 Lattice Dynamics and Electronic Fluctuations

To appreciate the difference in electronic (and optical) properties between crystals and semiconductors, we begin by addressing the time evolution of the Kohn-Sham (KS) eigenvalues from molecular-dynamics simulations as shown in Fig. 6.1.

Here we show the fluctuations of the KS eigenvalues at room temperature (300 K) in crystalline Si and amorphous Si. The thermal fluctuations of the KS eigenvalues are considerably larger for the amorphous system (*a-Si*) than for the crystal (*c*-Si), and the degree of fluctuation is obviously energy-dependent. It's also apparent that the tail states have a large fluctuation that 'fills in' much of the gap region. The energy scale of the problem is the thermal energy $k_B T$, of the order of 0.025 eV at T=300 K. While this value roughly characterizes the magnitude of fluctuations observed for the crystal, the thermal excursions of the Kohn-Sham states may be significantly larger (more than a factor of 10) near the Fermi level. Further, the fluctuations decay in amplitude as we move away from the conduction or valence band edges (far from the Fermi level) to a region where the states are normally delocalized. This leads to the conclusion that localization of a given eigenstate *amplifies* the fluctuations for the eigenvalue associated with that state.

6.2.2 Electron-Phonon Coupling, Eigenvalue Fluctuations and Localization

A crude derivation of electron phonon coupling (EPC) has been presented in [4] and is summarized below. EPC, denoted by $\Xi_n(\omega)$, has been shown to be given by

$$\Xi_n(\omega) = \sum_{\alpha=1}^{3N} \langle \psi_n | \frac{\partial \mathbf{H}}{\partial \mathbf{R}_\alpha} | \psi_n \rangle \chi_\alpha(\omega) \tag{6.4}$$

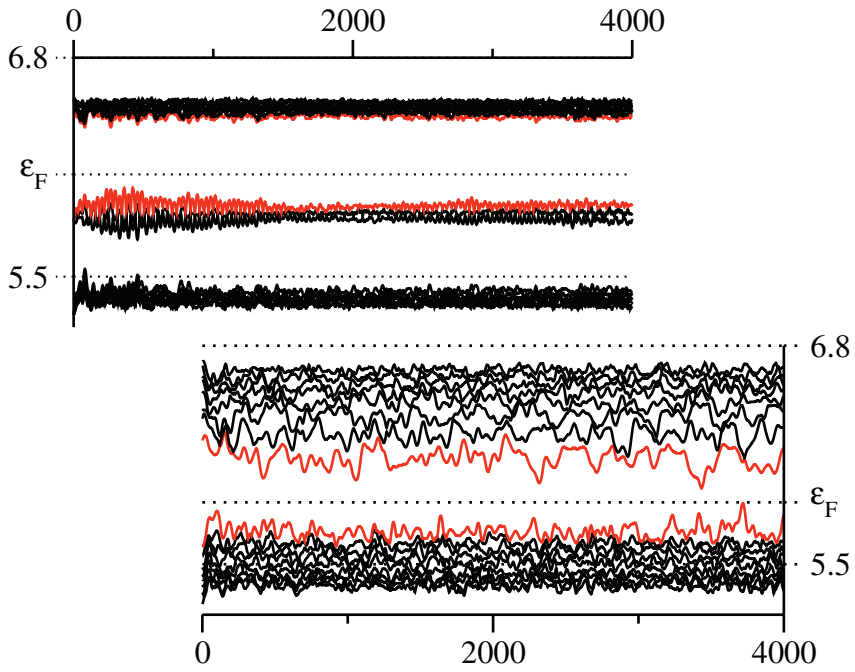

Figure 6.1: Thermal fluctuations of Kohn-Sham eigenvalues in the vicinity of the Fermi level for a 216-atom model of c-Si (top) and a-Si (bottom), both at 300K. The natural energy scale for the lattice in equilibrium is $kT \approx 0.025eV$, not far from what is seen for c-Si. The fluctuations in a-Si near the Fermi level can be ten times this. Here (and it the rest of the chapter, we employ the Γ approximation. A nearly universal approximation for semiconductor models with more than 100 atoms is the Γ-point approximation. Electron states are computed only at $\mathbf{k} = \mathbf{0}$, from which total energies and forces are computed based upon the assumption that the bands are nearly flat (with respect to $\mathbf{k}$ dispersion) for such a large cell. In a similar way, the density of states is usually taken at Γ only. It is noteworthy that for the 216-atom crystal cell there is a "gap" between ≈ 5.4 and 6.0 eV, appearing only because we did not integrate over the Brillouin zone of the cell (that is, we sampled only the Γ point), a sobering reminder of how slowly we approach the thermodynamic limit from an electronic perspective [139]!

where ψ_n is the wave function of n^{th} electron state, H is the Hamiltonian (*i.e.* $H\psi_n = \lambda_n\psi_n$), $\chi_\alpha(\omega)$ is the normal mode with angular frequency ω and the α's are the indices for the 3N degrees of freedom.

Inverse Participation Ratio (IPR) provides an estimate for the degree of localization of a wave function. A large value of IPR reflects a spatially compact or localized state, whereas a small value indicates an extended state. Here, the IPR, $\mathcal{I}_n$ is computed as

$$\mathcal{I}_n = \frac{\sum_i a_{in}^4}{(\sum_i a_{in}^2)^2} \tag{6.5}$$

where the a_{in} is the projection of eigenfunction ψ_n onto i^{th} basis vector. In this work, projections of states onto atomic s, p and d orbitals (provided by VASP) are used.

In reference [4], using a simplified framework to describe electron-phonon coupling, the following empirical relations have been derived:

$$\Xi_n^2(\omega) \sim \mathcal{I}_n, \tag{6.6}$$

$$\langle \delta\lambda_n^2 \rangle \propto \mathcal{I}_n. \tag{6.7}$$

where $\delta\lambda_{rms}$ is the root mean squared fluctuations in eigenvalues as given by

$$\delta\lambda_{rms} = \sqrt{\bar{\lambda}^2 - (\bar{\lambda})^2}. \tag{6.8}$$

In equation 6.8, the raised bar means average over the simulation at constant temperature T. In the course of analyzing new simulations for this chapter, we noted that a more general (closer) linkage between localization $\mathcal{I}$ and thermal variation of eigenvalues of the form

$$\delta\lambda_{rms} = \alpha\bar{\mathcal{I}} + \beta, \tag{6.9}$$

where α and β are constants that depend on the type of material. The value of α gives the 'amplification factor', a measure of how strongly the lattice vibrations affect electronic

energies of localized states. One may suppose that parameter α is a partial indicator of the TCR of a material doped into the fluctuating states.

6.2.3 Structural Change from Electronic/Optical Modification

Topological or chemical irregularities in amorphous networks lead to localized electron states in the gap or in the band tails. If such a system is exposed to light of appropriate wave length, then it becomes possible for the light to induce transitions of electrons from the top of the occupied states to low-lying unoccupied (conduction) states. Such a process is explicitly non-equilibrium and the response suffered by the system is of key interest. Here, we will simply assume that a photo-induced promotion of an electron occurs, by depleting the occupied states of one electron forming a hole and moving the electron to the bottom of the unoccupied conduction states. We will not dwell on the system specific details here but instead describe the short time response of the such systems suffering an occupation change and in particular the case of structure changes from placing an electron at the bottom of the conduction edge. We discuss this for *a*-Si and *a*-Se. Such a change in occupation results in a change of the Hellmann-Feynman forces leading to structural rearrangements, either negligible or significant, depending on the flexibility or stability of the network, and the localization of the states (and EPC). The timescale associated with this relaxation from occupation-induced changes are short (e.g. a few phonon periods), which can be exploited to develop novel applications in solids involving ultrafast processes [140].

6.3 Results

In the following, we present results from molecular dynamics simulations of *a*-Si, *a*-Se, and *a*-GaN to link the thermal variation of Kohn-Sham eigenvalues to temperatures and static properties of the eigenfunctions like inverse participation ratio (IPR). The first two materials are covalent, and the third is significantly ionic. Amorphous selenium has

the feature that the states near the Fermi level are built from *p*-orbitals with associated phenomena like valence alternation [141, 142, 138]. Amorphous silicon has band tails built from linear combinations of valence *s* and *p* states of bonding and anti-bonding form. On the other hand, *a*-GaN is partly ionic semiconductor in which the valence and conduction states involve quite different hybridizations, with the conduction edge consisting primarily of mixtures of *both* Ga and N *s*-states. The conduction states of *a*-GaN are less localized than the valence states, presumably because these states exhibit little dependence on local bond-angle disorder – because of the isotropy of the s-orbitals from which the eigenstates are built. Surprisingly, a-GaN also displays an essentially extended *midgap* state.

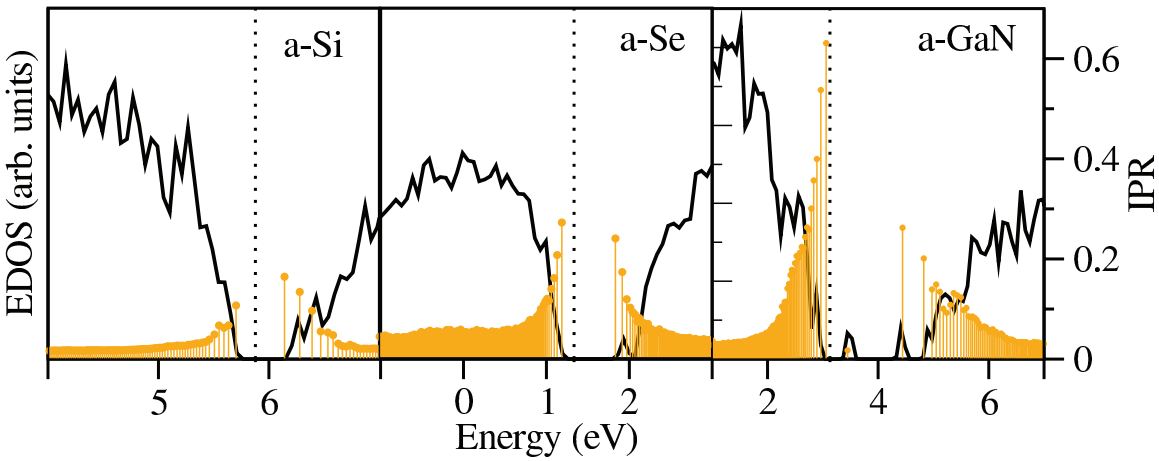

Figure 6.2: Electronic density of states (EDOS) and inverse participation ratio (IPR) for a-Si, a-Se and a-GaN. The black curves represent the EDOS and the orange drop lines represent IPR. The dotted lines represent the position of Fermi level for each model.The models being represented in the figure are described in the sections to follow.

6.3.1 Amorphous Silicon

Here, we employ a 216-atom continuous random network (CRN, [9]) model of *a*-Si due to Djordjevic et al [11, 57]. We'll refer to it as 'WWW model' throughout the chapter.

The model is discussed extensively elsewhere, and correctly produces the properties of *a*-Si for a small model.

In figure 6.2, the density of states and inverse participation ratio of electron states in *a*-Si are plotted. The IPR is slightly larger on the conduction tail than the valence tail. We begin by presenting results for thermally induced fluctuations of the Kohn-Sham states. In figure 6.3, we show the thermally induced fluctuation in the eigenvalues with color indicating extent of localization. As discussed elsewhere, the fluctuation for the eigenvalues in the gap are quite dramatic, varying over tenths of an eV for the lowest conduction states.

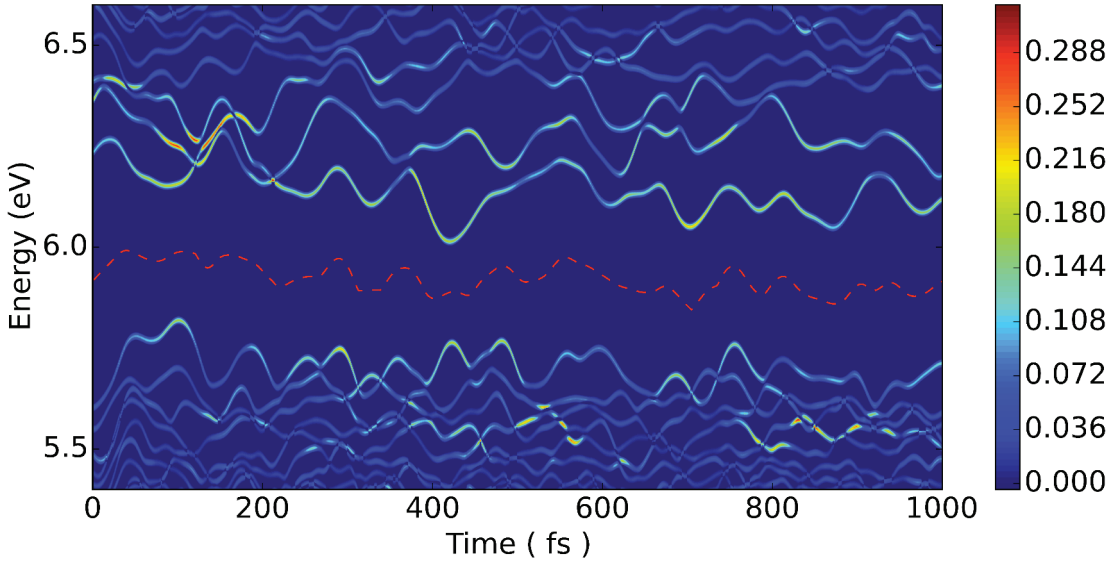

Figure 6.3: Thermal fluctuations of Kohn-Sham eigenvalues near the gap in *a*-Si. The eigenvalues are adiabatically evolving at a constant temperature of 300 K. The colors represent the localization of the states as measured by IPR (Eq. 6.5). The dotted line in red represents the Fermi Energy.

Beside the energy of electronic states, the thermal motion induces fluctuation in localization of these states as well. We note from figure 6.3, that such fluctuation in localization is higher for states with commensurate high fluctuation in energy (i.e. the

band edge states). We find that thermal fluctuation modulates the bond lengths and bond angles, resulting in a reshuffling of the atomic contributions to electronic states. If these states are already localized, such reshuffling can induce dramatic changes to the extent of localization. Inspection of figure 6.3 suggests that at a time near 100 fs, the conduction tail states become momentarily very localized. As an illustrative tale of variation in electronic structure induced by thermal disorder, we find that at this instant, the states are localized around long bonds or around broken bonds. We find that a pair of defects consisting of one dangling bond (a broken bond) and one floating bond (a five-fold bond) that are adjacent to each other are formed around this time. In figure 6.4, we show the charge density of the three lowest conduction tail states for this particular short-lived conformation. We note that these three states are largely localized around the newly formed defect pair, and also around long bonds in the network. Figure 6.4 shows the bonds longer than 2.5 Å and its evident that these conduction tail states have large projections onto these sites. Note that the long bonds in the cell show a spatial correlation among themselves forming a filament like pattern [143, 144]. It is notable that this defect is thermally induced and transient. After 200 fs, we see short-lived surges in the extent of localization of tail states and these surges correspond to various thermally induced defects and bond length fluctuations.

In figure 6.5, we see that there is a linear correlation between the RMS fluctuation of the eigenvalues and the the IPR (localization), confirming equation 6.9. To get a sense for the role of temperature dependence and a broader sense of the spectral dependence (of the general linkage between fluctuation and localization), see figure 6.6. Its is observed that the band tail states fluctuate far more than the deep states and that the spectral fluctuation increase with increase in temperature as is also clear from the discussion.

In *a*-Si:H, there is an extensively studied process of light-induced photo-degradation: the Staebler-Wronski effect, in which light exposure leads to the creation of charge carrier traps, presumably from defects created by the light exposure. This has been atomistically

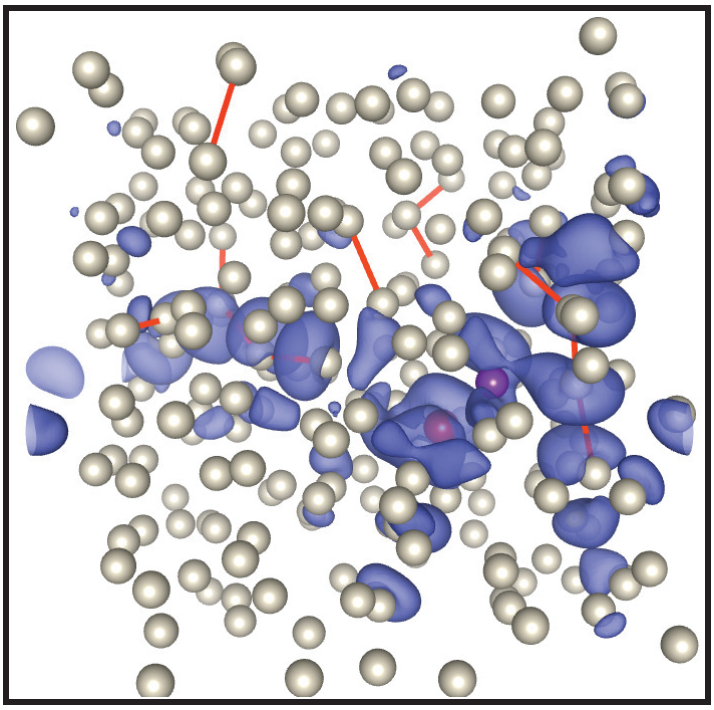

Figure 6.4: The combined charge density of lower three conduction states when these states are most localized. This corresponds to t = 100 fs in 6.3. Figure shows these states are most localized around the defect atoms (represented in color, purple: 5-fold, red: 3-fold) and around long bonds (bonds longer than 2.5 Å are shown as red sticks in the figure).

modeled by Fedders and coworkers [145]. The idea was to mimic photo-excitation by creating an electron-hole pair and tracking the creation and annihilation of structural defects. The scheme can be understood to be a sophisticated local heating approach, with the feature that the intensity of the local heating is critically determined by the electron-phonon coupling and the Hellmann-Feynman forces (equation 6.3) associated with the occupation change. Here, we have have conducted constant temperature MD using VASP [22, 23] and promoted an electron to the bottom of the conduction states. The LUMO drops precipitously into the gap, nearly closing the gap momentarily near t = 600 fs (see figure 6.7). This change is accompanied by creation and annihilation of short-lived geometrical defects in the network. We have empirically observed that there tends to be a

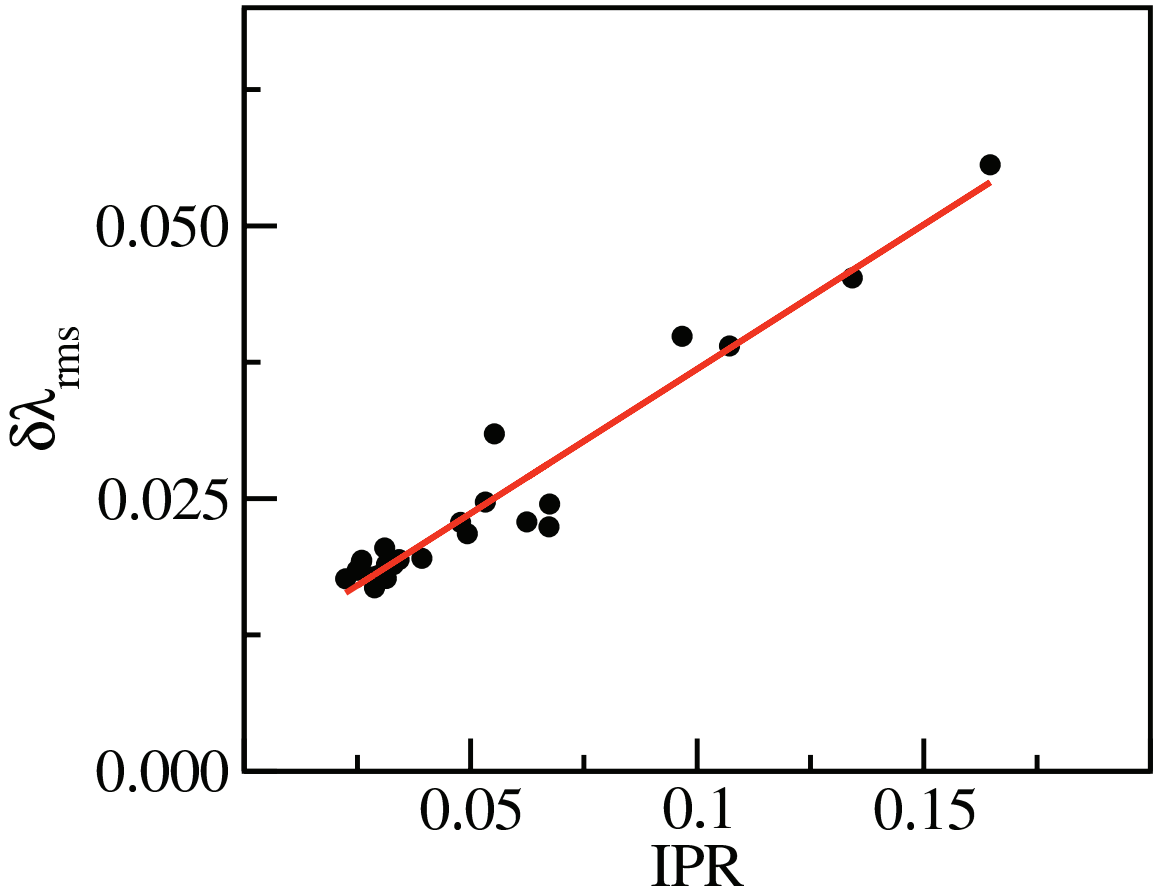

Figure 6.5: The correlation between RMS fluctuation of eigenvalues around the gap and corresponding inverse participation ratio (IPR) at 300 K for the electronic ground state in a-Si (Eq. 6.9). The bold red line is the linear fit of the plotted values. The fitted value of α (Eq. 6.9) for the linear fit is 0.26.

net increase in number of geometrical defects as a result of occupying a conduction state. Figure 6.8 shows the thermal fluctuation of number of defects at 300 K for the time interval that corresponds to the energy fluctuations in figure 6.7. A plausible explanation of this observation is that the lowest conduction state is already localized around coordination defects and long bonds. Occupying that state with an electron causes these atoms to feel the Hellmann-Feynman force coming from the newly occupied state and

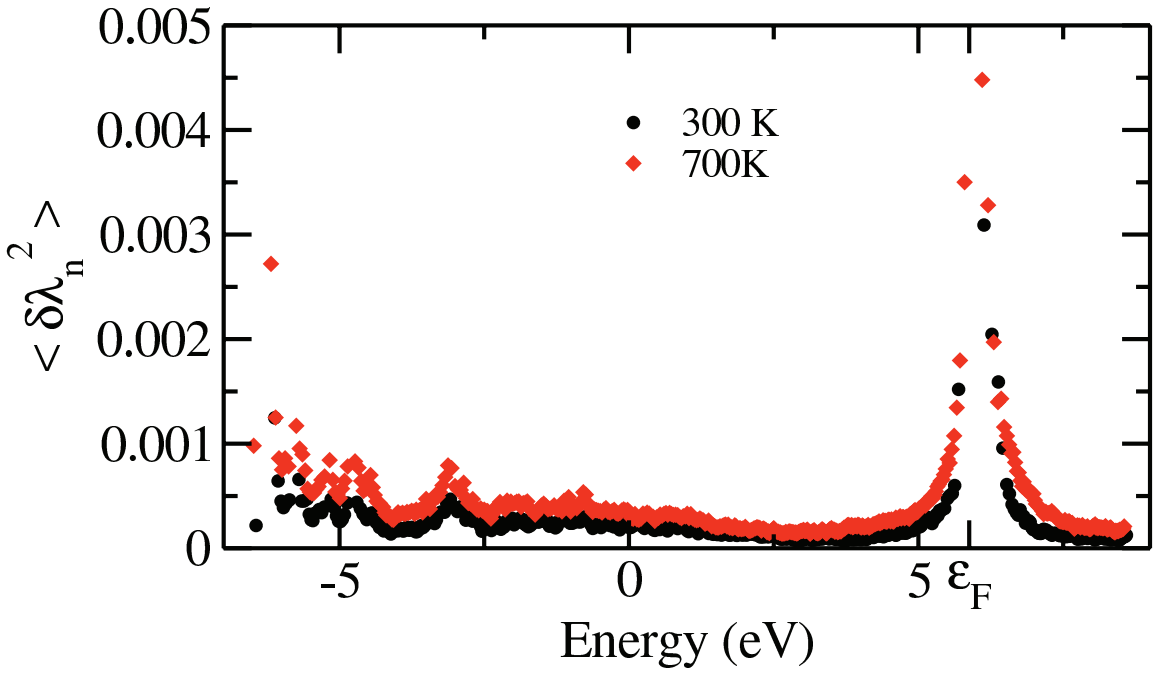

Figure 6.6: Temperature dependence of mean squared fluctuation of eigenvalues. The fluctuation is calculated over constant temperature MD at 300 K and 700 K. Symbol ε_F represents the position of Fermi energy. Note that the band edge states fluctuate more than the deep states. Also, the temperature modulation of the energy is higher for the tail states than for the deeper states.

hence these atoms become much more active. We observe that the states in excited system are much more localized than those in the unexcited system.

6.3.2 Amorphous Selenium

Amorphous selenium is different from *a*-Si in that its network is less constrained, which may be expected to play out in electron-phonon couplings of localized states. We make use of a 216-atom model of Zhang and Drabold [138] and relax it using LDA in plane wave basis. The model represents the material reasonably well as reported in earlier work [138, 140]. It is notable from figure 6.2 that the density of levels is higher near the

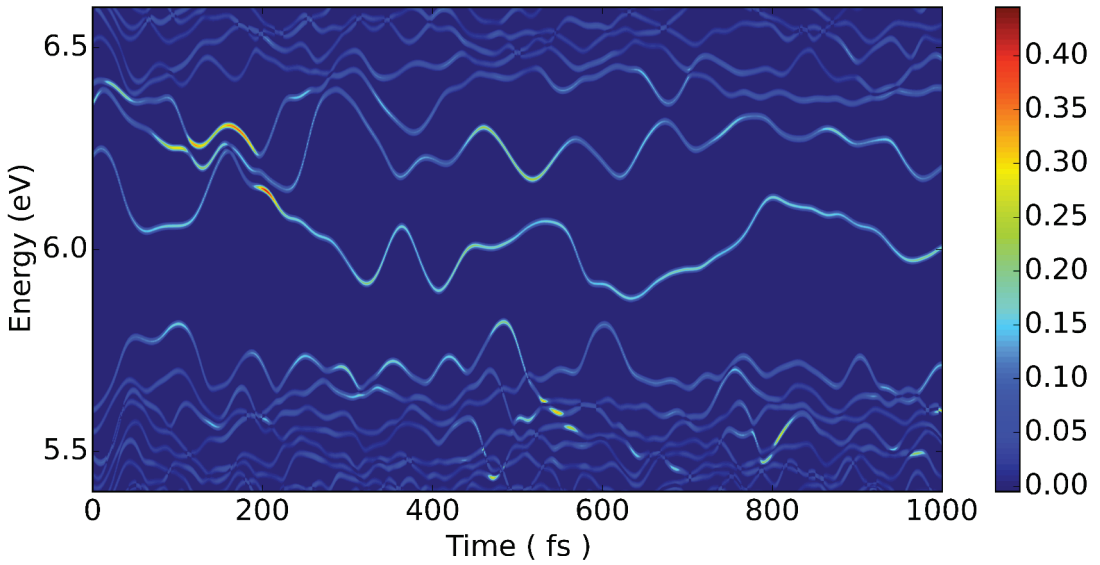

Figure 6.7: Thermal fluctuations of Kohn-Sham eigenvalues near the gap in excited *a*-Si. The eigenvalues are evolving under constant temperature at 300 K when an electron is promoted to conduction band. The color represents the localization of the states as measured by Inverse participation ratio (IPR). Note that this is a *non-equilibrium* simulation as the system responds to the promotion of an electron to the bottom of the conduction states. Fermi level for the unexcited system at t=0 is at 5.88 eV.

Fermi level for a-Se. The localization of the tail states is fairly similar at either band edges of the optical gap.

We perform constant temperature dynamics at 300 K using a Nosé thermostat and monitor the evolution of Kohn-Sham eigen energies. In figure 6.9 we show the thermal fluctuation of energies of states on the band edges. We see that the edge states fluctuate substantially more than the extended states (well into the valence and conduction bands) and they are more localized compared to the deep states. The system has an under coordinated and an over coordinated atoms to begin with. The equilibrium edge states are usually localized largely around these imperfections. The dynamics introduces many short-lived defect states (mostly dangling bonds and a few floating bonds) in the system.

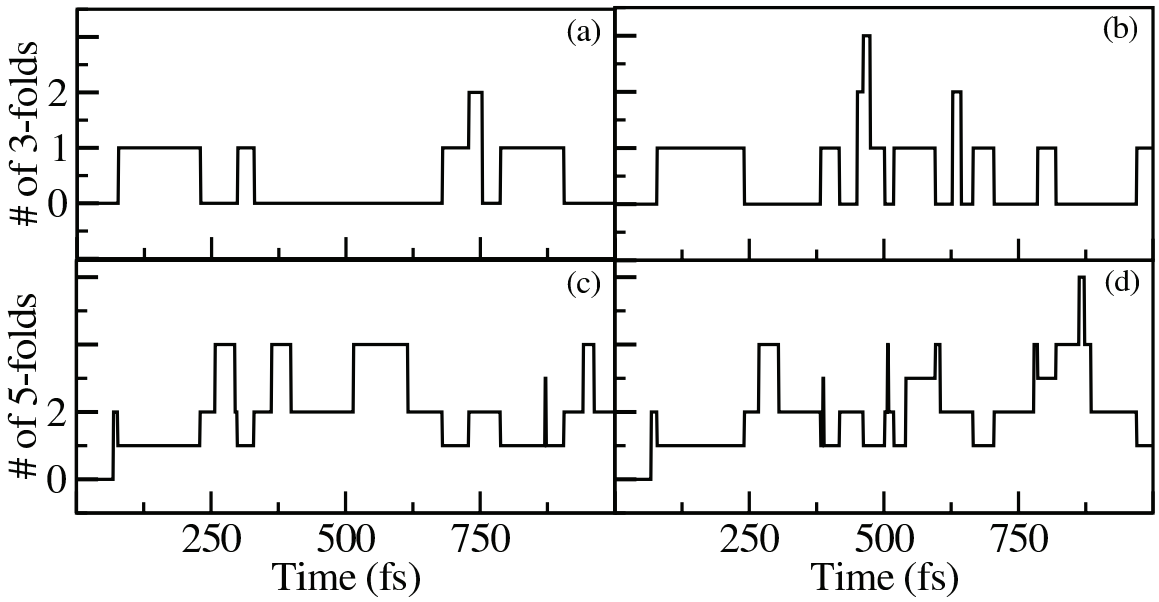

Figure 6.8: Thermally induced geometrical defects in excited and unexcited *a*-Si. (a) and (c) are the evolution of defects under constant temperature MD at 300 K in unexcited 216-atom *a*-Si. (b) and (d) are those for an excited system. Coordination is defined by a radius r_c = 2.7Å

In figure 6.10, we examine the correlation between the RMS variation of the eigenvalues and the thermally averaged IPR as in Eq. 6.9. Here, we see a strong correlation between the fluctuation of energy and the spatial localization of the state. We observe separate correlation for conduction states and the valence states. In relation to Eq. 6.9, we note that the 'amplification' factor α for conduction states is twice as big as for valence states. Figure 6.11 indicates once again that there is an unmistakeable connection between localization and electronic response to phonons. We note, as in figure 6.6, that the fluctuation of localized tail states is significantly higher than that of the extended valence and conduction states.

In figure 6.12, we consider the non-equilibrium (adiabatic) time development of the system – the response to adding a carrier to the LUMO state. We note that the LUMO plunges nearly 1 eV across the gap in a time of about 400 fs (see figure 6.13 to follow the

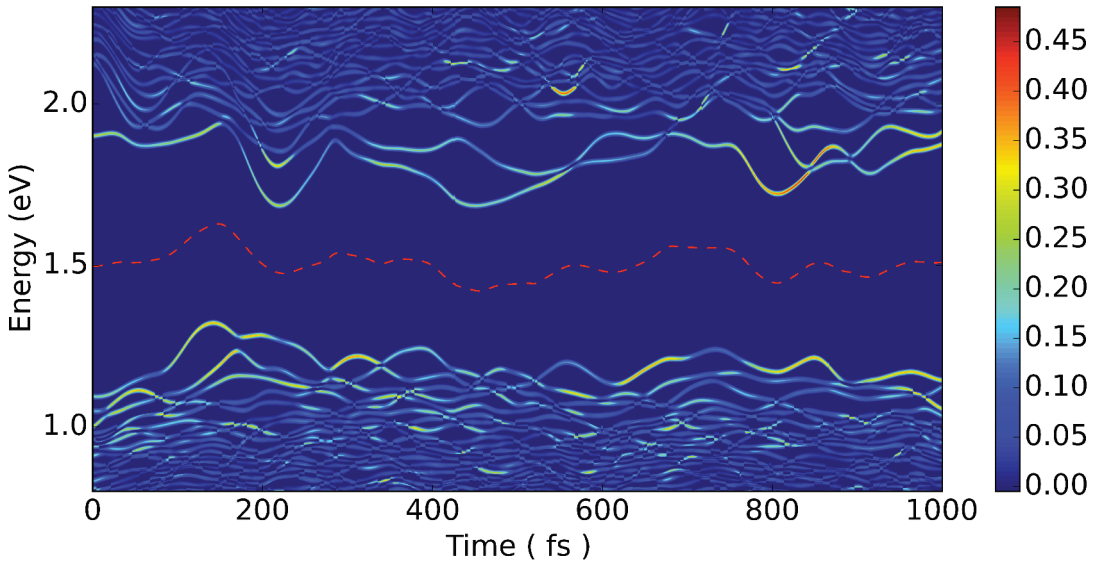

Figure 6.9: Thermal fluctuations of Kohn-Sham eigenvalues near the gap in *a*-Se. The color dimension corresponds to the localization of the states as measured by (IPR). The dotted line in red represents Fermi Energy.

evolution of LUMO on longer timescale). Whenever an electron fills a conduction state, the system tries to lower the total energy of the system, typically by the relevant state dropping into the gap, thereby reducing its (electronic) energy, and there will be geometrical changes associated with this electronic drop – bond breaking and/or formation. Some systems like Si may often be too constrained to allow geometrical rearrangements enabling such an electronic plunge. Amorphous Se, on the other hand, has a highly flexible (essentially polymeric) structure and hence can provide for the lowering of the newly filled conduction state. This suggests an explanation for why the photo-darkening effect in *a*-Se is so pronounced (see figure 6.13).

6.3.3 Amorphous Gallium Nitride

The case of the partly ionic system *a*-GaN makes an interesting counterpoint to the purely covalent materials described in earlier sections. The first peculiarity of this material

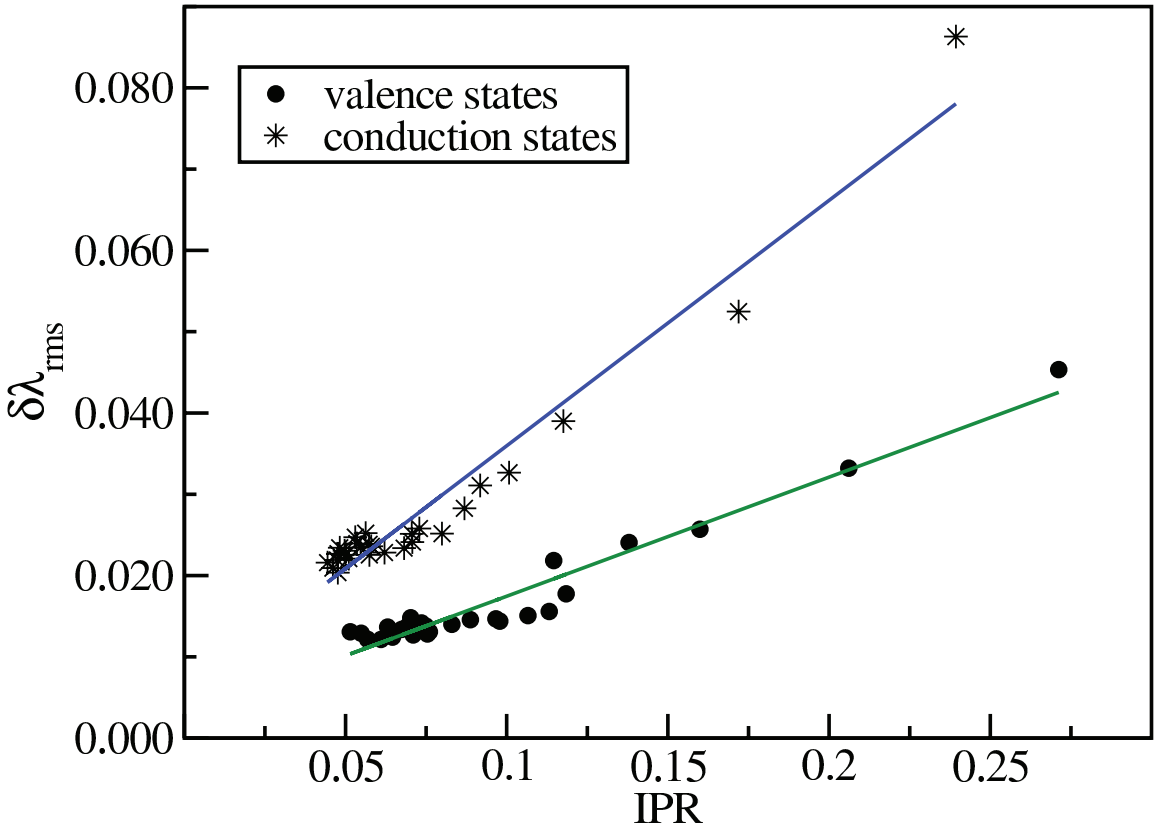

Figure 6.10: The correlation between RMS fluctuation of eigenvalues around the gap and corresponding inverse participation ratio (IPR) in *a*-Se (Eq. 6.9). The fluctuation is calculated over constant temperature MD at 300 K. Note that the fluctuation is higher for conduction states than for valence states. The correlation breaks neatly into two "branches", one for valence and one for conduction tail states. The green and blue lines represent the linear fit of the plotted values. The fitted value of α for the linear fits are 0.15 for valence states and 0.30 for conduction states.

is that the valence tail is more localized than the conduction tail. The reason for this is that the valence tail is susceptible to bond angle disorder whereas the conduction tail is more sensitive to bond length disorder (which is comparatively mild) [146]. In figure 6.14, we note that the valence states are densely packed together with notable fluctuations right at the band edge. Remarkably, a-GaN displays an essentially extended mid-gap state (see figure 6.2). This is of significant interest, since such states are unknown in covalent

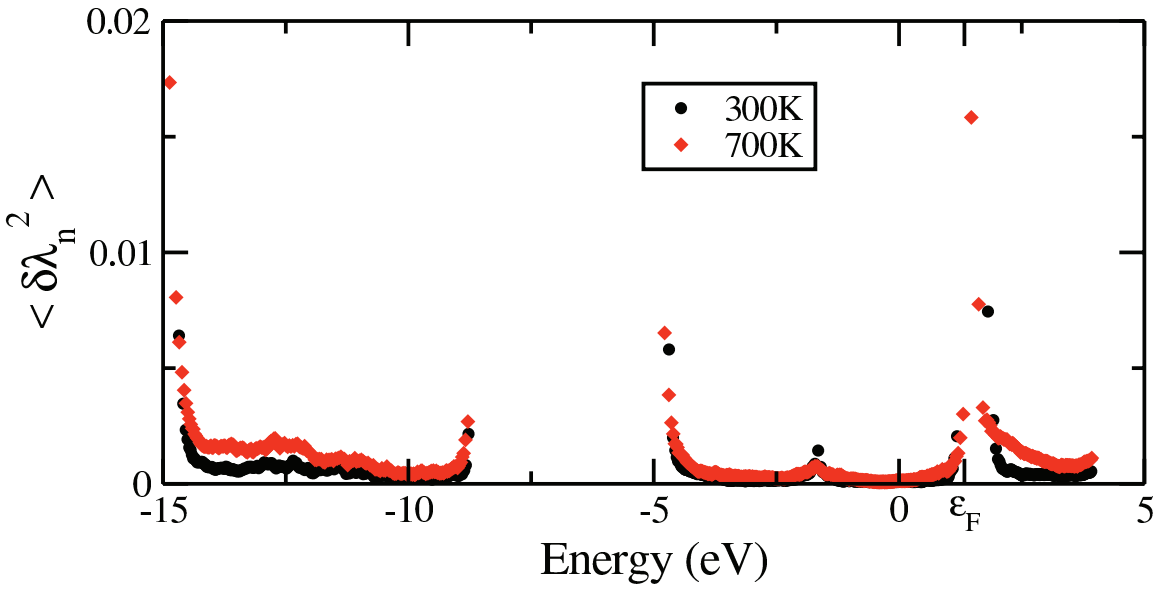

Figure 6.11: Temperature dependence of mean squared fluctuation of eigenvalues in *a*-Se. The fluctuation is calculated over constant temperature MD at 300 K. and 700 K. Symbol ε_F represents the position of Fermi energy. Note, in addition to the observations in Fig. 6.6, that deep states are virtually unaffected by temperature whereas the edge states see strong modulation.

systems like those discussed earlier. As we have suggested elsewhere, these distinctive extended states must yield better electronic conduction than in covalent systems [78, 146].

What is also of interest is the meandering conduction state (starting at near 4.5 eV at t=0), which shows a thermal dispersion of nearly 1 eV, the largest we have noted in any of these systems. In this case, we see a first example contradicting the general rule "more localized implies more fluctuation", clearly seen in figure 6.15. The linear correlation is remarkably well maintained, but again split into different branches for valence and conduction edges. Within a given band – conduction or valence, the rule of linear correlation between IPR and RMS fluctuation is preserved. The partitioning into two branches isn't surprising since hybridization of the eigenstates near the two band edges is quite different for GaN, suggesting that in general the two edges need to be treated

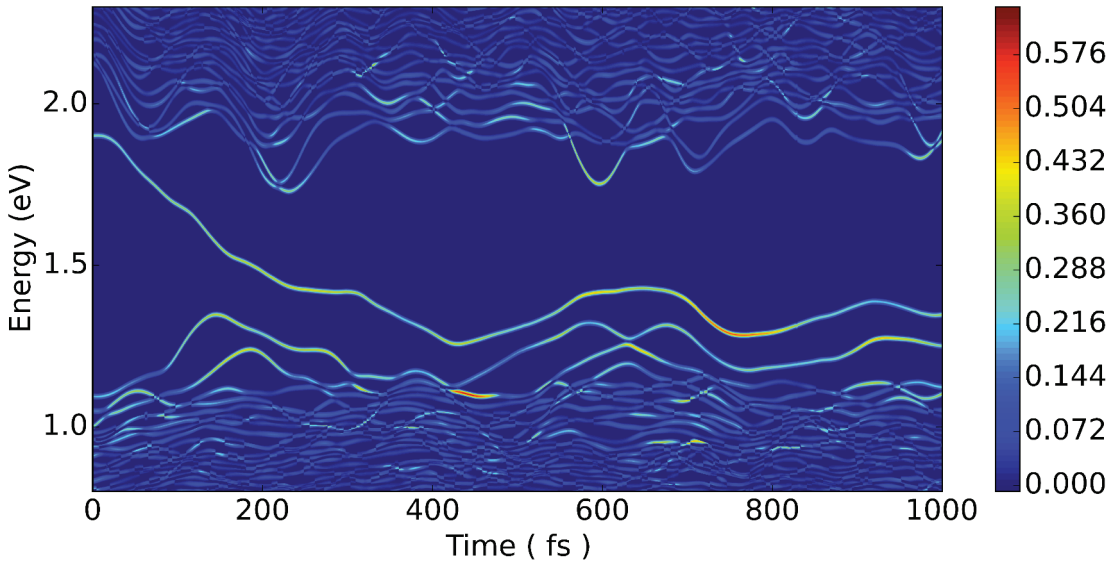

Figure 6.12: Thermal fluctuations of Kohn-Sham eigenvalues near the gap in excited *a*-Se. The system is kept at T=300 K when an electron is promoted to conduction band. The color dimension maps to the localization of the states (IPR). Fermi level for the unexcited system at t=0 is at 1.33 eV.

separately. Unlike previous experience in covalent systems, the state near 3.5 eV at t=0 is extremely extended despite being nearly a "midgap" state. As expected, such a delocalized state has a very weak EPC and barely shows thermal modulation at all.

In figure 6.15, the strong linear correlation between IPR and fluctuation is again observed. *The state near 4.5 eV at t=0 of figure 6.14 shows very high fluctuation compared to the rest of the conduction states and is not included in the plot.* There are two distinctive linear branches, one for the valence states, one for the conduction. As for the case of *a*-Se, We plot the data is plotted with thermally averaged IPR as abscissa and RMS (thermally indiced) variation as ordinate. Again, we plot it in this way because it shows a better correlation than the result implied by Eq. 6.7. This is an empirical, but evidently strong, correlation. Note that for all three cases, the intercept β (from Eq. 6.9) provides an

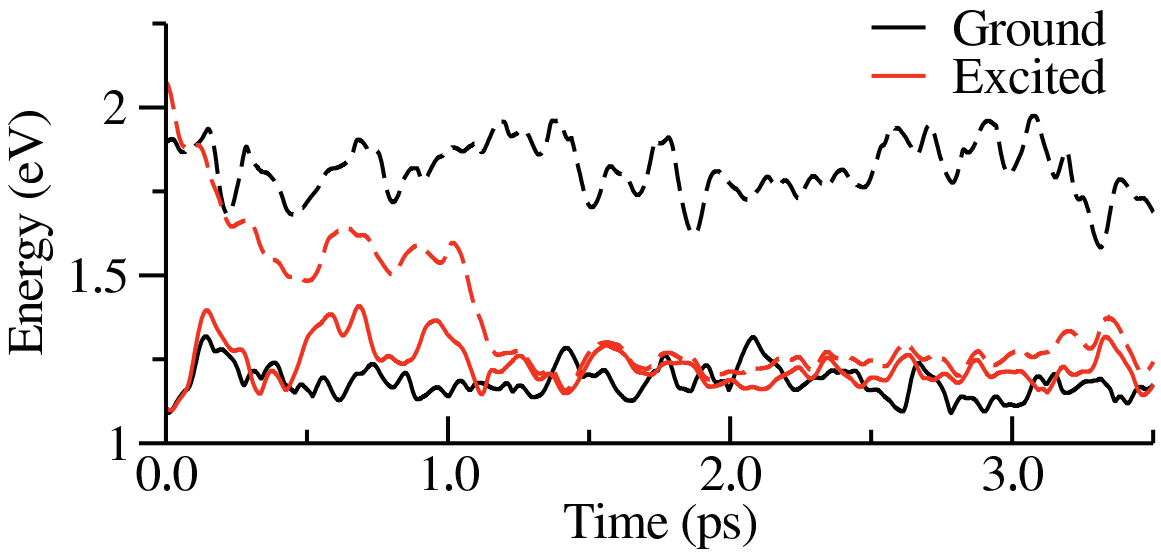

Figure 6.13: The evolution of HOMO and LUMO states of *a*-Se. The ground state represents the constant temperature MD at 300 K whereas the excited state refers to similar MD run when an electron is promoted to conduction band.

estimate for the fluctuation of an ideally extended ($\mathcal{I}$=0) state always of order or a bit smaller than kT.

6.4 Conclusions

We discussed the electronic response to atomic motion (by treating the latter classically) and the structural response of a system to an electronic modification. In a topologically-disordered semiconductor, we find that the EPC is strongly energy-dependent, and significantly larger for localized states than extended states. This energy dependence can lead to useful anomalies in transport (e.g. high Temperature Coefficient of Resistivity (TCR) behavior in doped *a*-Si:H) and at least a partial explanation for the Meyer-Neldel rule or compensation law [147]. It also explains the strong photo-response of amorphous semiconductors and glasses (e.g. photo-induced defect creation in *a*-Si:H or Staebler-Wronski effect [148]).

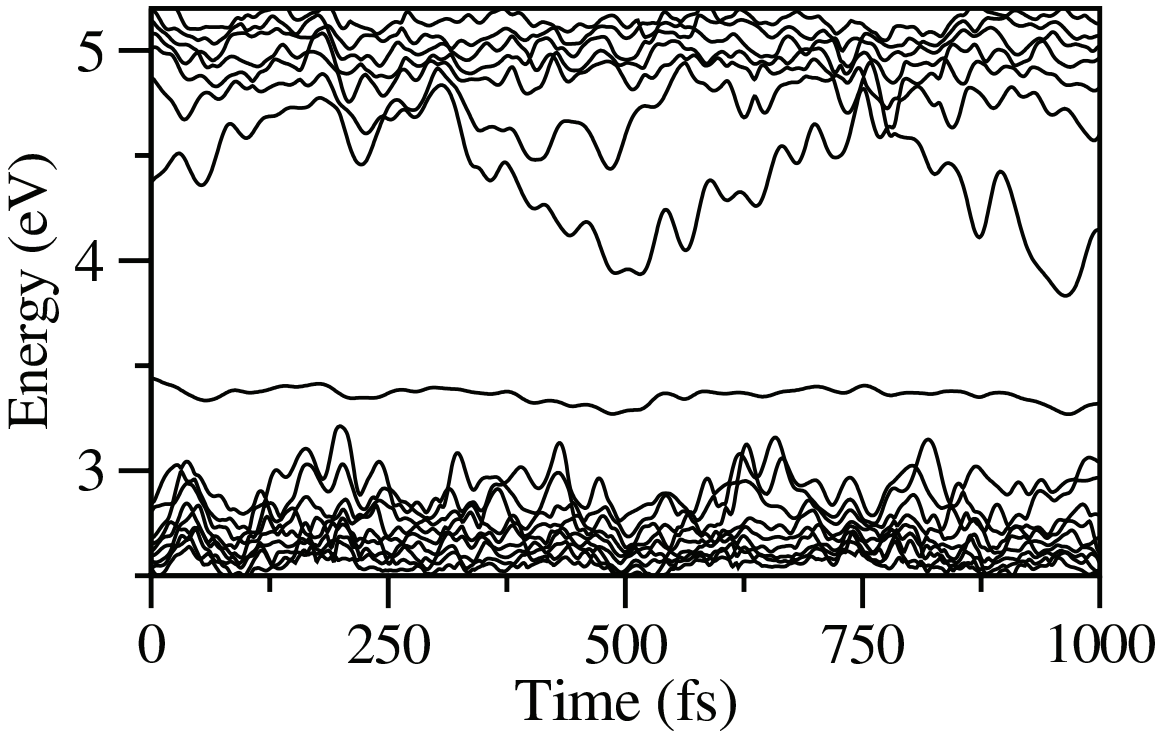

Figure 6.14: Thermal fluctuations of Kohn-Sham eigenvalues near the gap in GaN. The eigenvalues are evolving under constant temperature at 300 K. *Note the energetically itinerant conduction state level near 4.5 eV at t=0 and the extended mid-gap state near 3.5eV at t=0.* The Fermi level at t=0 is at 3.13 eV

In conclusion, we have carried out an array of accurate thermal MD simulations of realistic models of *a*-Si, *a*-Se and *a*-GaN. We have demonstrated a strong correlation between localization and thermally-induced modulation of Kohn-Sham eigenvalues. We report a new correlation (Eq. 6.9) that works for all three highly distinct materials. The value of this observation lies in its generality across systems with dramatically different chemistry and short-range order. We reveal the effects of changes in cell charge states, as a necessary ingredient to model light-induced changes in such materials.

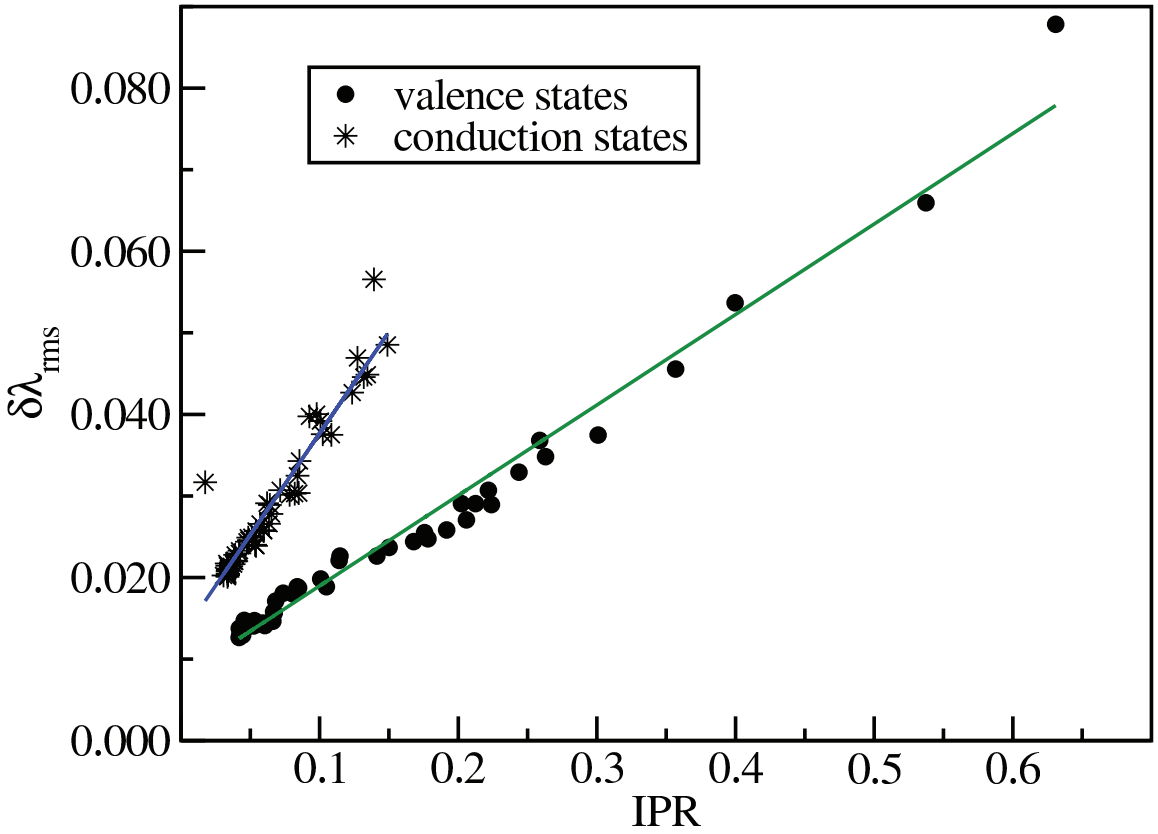

Figure 6.15: The correlation of RMS fluctuation of eigenvalues around the gap and corresponding inverse participation ratio (IPR) in GaN, as described by Eq. 6.9. The fluctuation is calculated over constant temperature MD at 300 K. Note that the fluctuation is higher for conduction states than for valence states. As was the case in Se, the correlation is observed in two separate branches for the conduction and valence edge states. The green and blue lines represent the linear fit of the plotted values. The observed value of α for the linear fits are 0.11 for valence states and 0.25 for conduction states.

7 Conclusions

We developed a novel method of incorporating *a priori* knowledge of electronic band gap into molecular dynamics simulations. The method involves computation of Hellmann Feynman forces associated with the electronic states near to the Fermi energy and since these forces are already computed as parts of the total force, the method doesn't incur significant computational cost. Using tight-binding MD simulation, we showed that models of amorphous silicon (*a*-Si) produced using this method show no mid-gap states that are typical of models with conventional melt quench methods. In addition, we showed that such electronic information purges structural defects (dangling and floating bonds, broad distribution bond lengths and bond angles) in the model *a*-Si. This is the first use of electronic structure constraints in to eliminate structural defects. We also showed, in the tight binding framework, band gap information can be used to tune sp^2/sp^3 ratio in amorphous carbon, allowing us to choose the character of the amorphous network while using the same tight-binding parametrization.

The method is then developed to engineer the band gap using *ab initio* molecular dynamics (AIMD) simulations. Using this method, we successfully modeled insulator-metal transition glass $GeSe_3Ag$. From a modeling point of view, this shows that such method can sample the energy landscape in a way to arrive at structural solutions with metal-like density of states (DOS). From a materials point of view, we show that the electronically conducting phase of *a*-$GeSe_3Ag$ consists of an enhanced Ag-Se phase and a diminished Ge-Se phase. Furthermore, we investigate the electronic transport in $GeSe_3Ag$ using more conventional tools of quantum chemistry and show that the non-bridging and terminating Se atoms play a significant role in DC conductivity. By explicitly modeling Ag-nanowires in a glassy host, we show that Ag-nanowires of at least 2-3 atom thickness do *not* take part in electronic conduction. We used an empirical two-body potential to model $GeSe_3Ag$ glass and the recovery of the system after an impact. We showed, with in

the limit of the accuracy of the potential, that the system recovers its pre-impact structural features in less than a nanosecond time making the material suitable for use as radiation dosimeter.

We investigated the coupling between lattice vibrations and electrons within the framework of state-of-the-art *ab initio* calculations and showed that there exists an strong correlation between localization of electronic states and the thermal modulation of the energies of these states. It is shown that this gives rise to drastically different thermal modulation of electron energies for crystalline and disordered solids and we discussed interesting new correlations between localized band edge states and thermal fluctuation.

7.1 Future Work

Gap sculpting is useful to solve modeling problems where conventional melt-quench MD produces defect states in the band gap. It can be further extended to incorporate hybrid functionals and GW methods where the size of band gap is closer to experimentally measured values. Gap sculpting provides us ways to explore doped structures, mid-gap defects or meta-stable configurations with interesting properties. Wide band-gap semi-conductors like TiO_2 are ideal candidates for this type of pursuit. Band tuning using Hellmann-Feynman forces can be further extended to spin polarized calculations to explore interesting spin arrangements of useful systems, e.g. maximally polarized structures, half metals or spin filtering systems.

The channels of electronic conduction in CBRAM materials should be further explored using more advanced tools. More rigorous formalisms should be developed to project the conductivity in real space and highlight the parts that serve as channels of electron conduction.

References

[1] Boolchand, P. *Insulating and semiconducting glasses*, volume 17. World scientific, (2000).

[2] Schrödinger, E. *What is life?: With mind and matter and autobiographical sketches*. Cambridge University Press, (1992).

[3] Fedders, P. and Drabold, D. *Physical Review B* **53**(7), 3841 (1996).

[4] Atta-Fynn, R., Biswas, P., and Drabold, D. *Physical Review B* **69**(24), 245204 (2004).

[5] Mott, N. F. and Davis, E. A. *Electronic processes in non-crystalline materials*. Oxford University Press, Oxford, (1979).

[6] Pan, Y., Inam, F., Zhang, M., and Drabold, D. *Physical Review Letters* **100**(20), 206403 (2008).

[7] Ziman, J. M. *Models of disorder: the theoretical physics of homogeneously disordered systems*. CUP Archive, (1979).

[8] Weaire, D. and Thorpe, M. *Physical Review B* **4**(8), 2508 (1971).

[9] Zachariasen, W. H. *Journal of the American Chemical Society* **54**(10), 3841–3851 (1932).

[10] Mott, N. *Contemporary Physics* **18**(3), 225–245 (1977).

[11] Wooten, F., Winer, K., and Weaire, D. *Physical Review Letters* **54**(13), 1392 (1985).

[12] Mousseau, N. and Barkema, G. *Journal of Physics: Condensed Matter* **16**(44), S5183 (2004).

[13] Allen, M. P. and Tildesley, D. J. *Computer simulation of liquids*. Oxford university press, (1989).

[14] Iyetomi, H., PriyaVashishta, and Kalia, R. K. *Journal of Non-Crystalline Solids* **262**(1-3), 135–142 (2000).

[15] Plimpton, S. *Journal of Computational Physics* **117**, 1–19 (1995).

[16] Kwon, I., Biswas, R., Wang, C., Ho, K., and Soukoulis, C. *Physical Review B* **49**(11), 7242 (1994).

[17] Xu, C., Wang, C., Chan, C., and Ho, K. *Journal of Physics: Condensed Matter* **4**(28), 6047 (1992).

[18] Goodwin, L., Skinner, A., and Pettifor, D. *Europhysics Letters* **9**(7), 701 (1989).

[19] Martin, R. M. *Electronic structure: basic theory and practical methods*. Cambridge university press, (2004).

[20] Hohenberg, P. and Kohn, W. *Physical Review* **136**(3B), B864 (1964).

[21] Kohn, W. and Sham, L. J. *Physical Review* **140**(4A), A1133 (1965).

[22] Kresse, G. and Furthmüller, J. *Physical Review B* **54**(16), 11169 (1996).

[23] Kresse, G. and Furthmüller, J. *Computational Materials Science* **6**(1), 15–50 (1996).

[24] Blöchl, P. E. *Physical Review B* **50**(24), 17953 (1994).

[25] Kresse, G. and Joubert, D. *Physical Review B* **59**(3), 1758 (1999).

[26] Perdew, J. P. and Zunger, A. *Physical Review B* **23**(10), 5048 (1981).

[27] Perdew, J. P., Burke, K., and Ernzerhof, M. *Physical Review Letters* **77**(18), 3865 (1996).

[28] Popescu, M. *Non-crystalline Chalcogenides* **8** (2000).

[29] Elliott, S. R. *Materials Science and Technology* **9**, 375 (1991).

[30] Mitkova, M., Wang, Y., and Boolchand, P. *Physical Review Letters* **83**(19), 3848 (1999).

[31] Kolobov, A. V., editor. John Wiley & Sons, (2006).

[32] Mitkova, M. In *Insulating and semiconducting glasses,* Boolchand, P., editor, volume 17, 483–514. World Scientific (2000).

[33] Kozicki, M. N. and Mitkova, M. October 21 (2003). US Patent 6,635,914.

[34] Valov, I., Waser, R., Jameson, J. R., and Kozicki, M. N. *Nanotechnology* **22**(25), 254003 (2011).

[35] Hansen, J.-P. and McDonald, I. R. *Theory of simple liquids*. Elsevier, (1990).

[36] Elliott, S. R. *Physics of amorphous materials*. Longman Group, Longman House, Burnt Mill, Harlow, Essex CM 20 2 JE, England, 1983., (1983).

[37] Cusack, N. and Stein, D. L. *Physics Today* **41**, 110 (1988).

[38] Le Roux, S. and Petkov, V. *Journal of Applied Crystallography* **43**(1), 181–185 (2010).

[39] Wegner, F. *Zeitschrift für Physik B Condensed Matter* **36**(3), 209–214 (1980).

[40] Prasai, K., Biswas, P., and Drabold, D. *Scientific Reports* **5**, 15522 (2015).

[41] Prasai, K., Biswas, P., and Drabold, D. A. *physica status solidi (a)* (2016).

[42] Prasai, K. and Drabold, D. A. *Nanoscale Research Letters* **9**(1), 594 (2014).

[43] Prasai, K., Chen, G., and Drabold, D. A. *Physical Review Materials* **1**(1), 015603 (2017).

[44] Prasai, K., Biswas, P., and Drabold, D. *Semiconductor Science and Technology* **31**(7), 73002–73015 (2016).

[45] Stillinger, F. H. *Physical Review E* **59**(1), 48 (1999).

[46] Biswas, P., Atta-Fynn, R., and Drabold, D. *Physical Review B* **69**(19), 195207 (2004).

[47] Biswas, P., Drabold, D., et al. *Physical Review B* **71**(5), 054204 (2005).

[48] Gereben, O. and Pusztai, L. *Physical Review B* **50**(19), 14136 (1994).

[49] Cliffe, M. J., Dove, M. T., Drabold, D., and Goodwin, A. L. *Physical Review Letters* **104**(12), 125501 (2010).

[50] Akola, J., Jones, R., Kohara, S., Kimura, S., Kobayashi, K., Takata, M., Matsunaga, T., Kojima, R., and Yamada, N. *Physical Review B* **80**(2), 020201 (2009).

[51] Los, J. H. and Kühne, T. D. *Physical Review B* **87**(21), 214202 (2013).

[52] Timilsina, R. and Biswas, P. *Journal of Physics: Condensed Matter* **25**(16), 165801 (2013).

[53] Pandey, A., Biswas, P., and Drabold, D. *Physical Review B* **92**(15), 155205 (2015).

[54] Cliffe, M. J. and Goodwin, A. L. *physica status solidi (b)* **250**(5), 949–956 (2013).

[55] Tanaka, K. and Odajima, A. *Solid State Communications* **43**(12), 961–964 (1982).

[56] Sankey, O. F. and Niklewski, D. J. *Physical Review B* **40**(6), 3979 (1989).

[57] Djordjević, B. R., Thorpe, M. F., and Wooten, F. *Physical Review B* **52**(8), 5685 (1995).

[58] Laaziri, K., Kycia, S., Roorda, S., Chicoine, M., Robertson, J., Wang, J., and Moss, S. *Physical Review B* **60**(19), 13520 (1999).

[59] Laaziri, K., Kycia, S., Roorda, S., Chicoine, M., Robertson, J., Wang, J., and Moss, S. *Physical Review Letters* **82**(17), 3460 (1999).

[60] Sjoerd Roorda, L. J. L. *Science* **338**(6114), 1539 December (2012).

[61] Robertson, J. *Advanced Physics* **35**(4), 317–374 (1986).

[62] Robertson, J. *Materials Science and Engineering: R: Reports* **37**(4), 129–281 (2002).

[63] McKenzie, D., Muller, D., and Pailthorpe, B. *Physical Review Letters* **67**(6), 773 (1991).

[64] Pan, H., Pruski, M., Gerstein, B., Li, F., and Lannin, J. S. *Physical Review B* **44**(13), 6741 (1991).

[65] Kelires, P. *Physical Review Letters* **68**(12), 1854 (1992).

[66] Drabold, D., Fedders, P., and Stumm, P. *Physical Review B* **49**(23), 16415 (1994).

[67] Sankey, O. F. and Niklewski, D. J. *Physical Review B* **40**(6), 3979 (1989).

[68] Tersoff, J. *Physical Review Letters* **61**(25), 2879 (1988).

[69] Wang, C. and Ho, K. *Physical Review Letters* **71**(8), 1184 (1993).

[70] Wang, C., Ho, K., and Chan, C. *Physical Review Letters* **70**(5), 611 (1993).

[71] Galli, G., Martin, R. M., Car, R., and Parrinello, M. *Physical Review Letters* **62**(5), 555 (1989).

[72] Wang, C. and Ho, K. *Journal of Physics: Condensed Matter* **6**(17), L239 (1994).

[73] Wang, C., Chan, C., and Ho, K. *Physical Review B* **45**(21), 12227 (1992).

[74] Harada, A., Shimojo, F., and Hoshino, K. *Journal of the Physical Society of Japan* **74**(7), 2017–2024 (2005).

[75] Kim, E. and Lee, Y. H. *Physical Review B* **49**(3), 1743 (1994).

[76] Servalli, G. and Colombo, L. *European Physical Letters* **22**(2), 107 (1993).

[77] Durandurdu, M., Drabold, D., and Mousseau, N. *Physical Review B* **62**(23), 15307 (2000).

[78] Stumm, P. and Drabold, D. *Physical Review Letters* **79**(4), 677 (1997).

[79] Mott, N. F. and Davis, E. A. *Electronic processes in non-crystalline materials*. Oxford University Press, Oxford, (2012).

[80] Prasai, K., Biswas, P., and Drabold, D. *Scientific Reports* **5** (2015).

[81] Piarristeguy, A., Mirandou, M., Fontana, M., and Arcondo, B. *Journal of Non-Crystalline solids* **273**(1), 30–35 (2000).

[82] Arcondo, B., Urena, M., Piarristeguy, A., Pradel, A., and Fontana, M. *Physica B: Condensed Matter* **389**(1), 77–82 (2007).

[83] Van Tuan, D., Kumar, A., Roche, S., Ortmann, F., Thorpe, M., and Ordejon, P. *Physical Review B* **86**(12), 121408 (2012).

[84] Abtew, T., Zhang, M., and Drabold, D. *Physical Review B* **76**(4), 045212 (2007).

[85] Galli, G., Martin, R. M., Car, R., and Parrinello, M. *Physical Review B* **42**(12), 7470 (1990).

[86] Allen, P. B. and Broughton, J. Q. *J. Phys. Chem.;(United States)* **91**(19) (1987).

[87] Glazov, V. M., Chizhevskaya, S. N., and Glagoleva, N. N. *Plenum Press, New York, 1969, 362 P* (1969).

[88] Boolchand, P. and Bresser, W. *Philosophical Magazine B* **80**(10), 1757–1772 (2000).

[89] Mitkova, M., Kozicki, M., Kim, H., and Alford, T. *Journal of Non-Crystalline solids* **352**(9), 1986–1990 (2006).

[90] Prasai, B. and Drabold, D. *Physical Review B* **83**(9), 094202 (2011).

[91] Tafen, D. N., Drabold, D., and Mitkova, M. *Physical Review B* **72**(5), 054206 (2005).

[92] Akola, J., Beuneu, B., Jones, R., Jóvári, P., Kaban, I., Kolář, J., Voleská, I., and Wágner, T. *Journal of Physics: Condensed Matter* **27**(48), 485304 (2015).

[93] Wang, R. Y., Tangirala, R., Raoux, S., Jordan-Sweet, J. L., and Milliron, D. J. *Advanced Materials* **24**(1), 99–103 (2012).

[94] Waser, R., Dittmann, R., Staikov, G., and Szot, K. *Advanced Materials* **21**(25-26), 2632–2663 (2009).

[95] Nagarajan, L., De Souza, R. A., Samuelis, D., Valov, I., Börger, A., Janek, J., Becker, K.-D., Schmidt, P. C., and Martin, M. *Nature materials* **7**(5), 391–398 (2008).

[96] Balakrishnan, M., Kozicki, M. N., Poweleit, C. D., Bhagat, S., Alford, T. L., and Mitkova, M. *Journal of non-crystalline solids* **353**(13), 1454–1459 (2007).

[97] Dong, J. and Drabold, D. *Physical Review Letters* **80**(9), 1928 (1998).

[98] Chen, G. Private Communication.

[99] Kozicki, M. N., Mitkova, M., and Valov, I. In *Resistive Switching: From Fundamentals of Nanoionic Redox Processes to Memristive Device Applications,* Ielmini, D. and Waser, R., editors, 483–514. John Wiley & Sons (2015).

[100] Baranovski, S. *Charge transport in disordered solids with applications in electronics*, volume 17. John Wiley & Sons, (2006).

[101] Overhof, H. and Thomas, P. *Electronic transport in disordered semiconductors*, volume 17, 553–606. World Scientific (2000).

[102] Kozicki, M. N. and Mitkova, M. *Journal of Non-Crystalline solids* **352**(6), 567–577 (2006).

[103] Hirose, Y. and Hirose, H. *Journal of Applied Physics* **47**(6), 2767–2772 (1976).

[104] Westwood, J., Georgopoulos, P., and Whitmore, D. *Journal of Non-Crystalline solids* **107**(1), 88–100 (1988).

[105] Dejus, R. J., Susman, S., Volin, K. J., Montague, D. G., and Price, D. L. *Journal of Non-Crystalline solids* **143**, 162–180 (1992).

[106] Kawaguchi, T., Maruno, S., and Elliott, S. R. *Journal of Applied Physics* **79**(12), 9096–9104 (1996).

[107] Chaudhuri, I., Inam, F., and Drabold, D. *Physical Review B* **79**(10), 100201 (2009).

[108] Pandey, A., Biswas, P., and Drabold, D. A. *Scientific Reports* **6** (2016).

[109] Kozicki, M., Mitkova, M., Zhu, J., and Park, M. *Microelectronic Engineering* **63**(1), 155–159 (2002).

[110] Mirandou, M., Fontana, M., and Arcondo, B. *Journal of Materials Processing Technology* **143**, 420–424 (2003).

[111] Kubo, R. *Journal of the Physical Society of Japan* **12**(6), 570–586 (1957).

[112] Drabold, D. A. and Prasai, K. *Unpublished* .

[113] Ovshinsky, S. R. *Non-Crystalline materials for Optoelectronics*. INOE, Bucharest, (2004).

[114] Wuttig, M. and Yamada, N. *Nature Materials* **6**(824) (2007).

[115] Rowlands, J. and Kasap, S. *Physics Today* **50**(24) (1997).

[116] Mitkova, M. and Kozicki, M. N. *Journal of Non-Crystalline Solids* **299-302**, 1023–1027 (2002).

[117] Krecmer, P., Moulin, A. M., Stephenson, R. J., Rayment, T., Welland, M. E., and Elliott, S. R. *Science* **277**(5333), 1799–1802 (1997).

[118] Poborchii, V. V., Kolobov, A. V., and Tanaka, K. *Applied Physics Letters* **74**(2), 215–217 (1999).

[119] Dandamudi, P., Kozicki, M., Barnaby, H., Gonzalez-Velo, Y., Mitkova, M., Holbert, K., Ailavajhala, M., and Yu, W. *Nuclear Science, IEEE Transactions on* **60**(6), 4257–4264 (2013).

[120] Mitkova, M. and Butt, D. June 18 (2013). US Patent 8,466,425.

[121] Mitkova, M., Chen, P., Ailavajhala, M., Butt, D., Tenne, D., Barnaby, H., and Esqueda, I. *Journal of Non-Crystalline Solids* **377**(0), 195 – 199 (2013).

[122] Laakkonen, J. and Neiminen, R. M. *Physical Review B* **41**, 7 (1990).

[123] Prasai, B. and Drabold, D. A. *Physical Review B* **83**, 094202 (2011).

[124] Tafen, D. N., Drabold, D. A., and Mitkova, M. *Physical Review B* **72**(054206) (2005).

[125] Gibson, J. B., Goland, A. N., Milgram, M., and Vineyard, G. H. *Physical Review* **120**, 4 (1960).

[126] de la Rubia, T. D., Averback, R. S., Benedek, R., and King, W. E. *Physical Review Letters* **59**, 17 (1987).

[127] Trachenko, K., Dove, M. T., Artacho, E., Todorov, I. T., Artacho, E., Todorov, I. T., and Smith, W. *Physical Review B* **73**, 174207 (2006).

[128] Robinson, M. T. and Torrens, I. M. *Physical Review B* **9**(12) (1974).

[129] Biersack, J. P. and Haggmark, L. G. *Nuclear Instruments and mathods* **174**, 257–269 (1980).

[130] Drabold, D. A. *European Physical Journal B* **68**, 1–21 (2009).

[131] Dejus, R., Susman, S., Volin, K., Montague, G., and D.L.Price. *Journal of Non-Crystalline Solids* **143**(162) (1992).

[132] Kozicki, M. N. and Mitkova, M. *Journal of Non-Crystalline Solids* **352**, 567–577 (2006).

[133] Prasai, B., Chen, G., and Drabold, D. A. *Applied Physics Letters* **102**(041907) (2013).

[134] Ardondo, B., Urena, M. A., Piarristeguy, A., Pradel, A., and Fontana, M. *Physica B* **389**, 77–82 (2007).

[135] King, W. E. and Benedek, R. *Journal of Nuclear Materials* **117**(26) (1983).

[136] Nordlund, K. *Computational Material Science* **3**, 448–456 (1995).

[137] Jones, R. O. *Reviews of Modern Physics* **87**(3), 897 (2015).

[138] Zhang, X. and Drabold, D. *Physical Review Letters* **83**(24), 5042 (1999).

[139] Drabold, D., Dow, J., Fedders, P., Carlsson, A., and Sankey, O. F. *Physical Review B* **42**(8), 5345 (1990).

[140] Sharma, R., Prasai, K., Drabold, D., and Adarsh, K. *AIP Advances* **5**(7), 077164 (2015).

[141] Kastner, M., Adler, D., and Fritzsche, H. *Physical Review Letters* **37**(22), 1504 (1976).

[142] Street, R. and Mott, N. *Physical Review Letters* **35**(19), 1293 (1975).

[143] Pan, Y., Inam, F., Zhang, M., and Drabold, D. *Physical Review Letters* **100**(20), 206403 (2008).

[144] Inam, F., Lewis, J. P., and Drabold, D. *physica status solidi (a)* **207**(3), 599–604 (2010).

[145] Fedders, P., Fu, Y., and Drabold, D. *Physical Review Letters* **68**(12), 1888 (1992).

[146] Cai, B. and Drabold, D. *Physical Review B* **84**(7), 075216 (2011).

[147] Meyer, W. and Neldel, H. *Z. tech. Phys* **18**(12), 588–593 (1937).

[148] Staebler, D. and Wronski, C. *Applied Physics Letters* **31**(4), 292–294 (1977).

Thesis and Dissertation Services